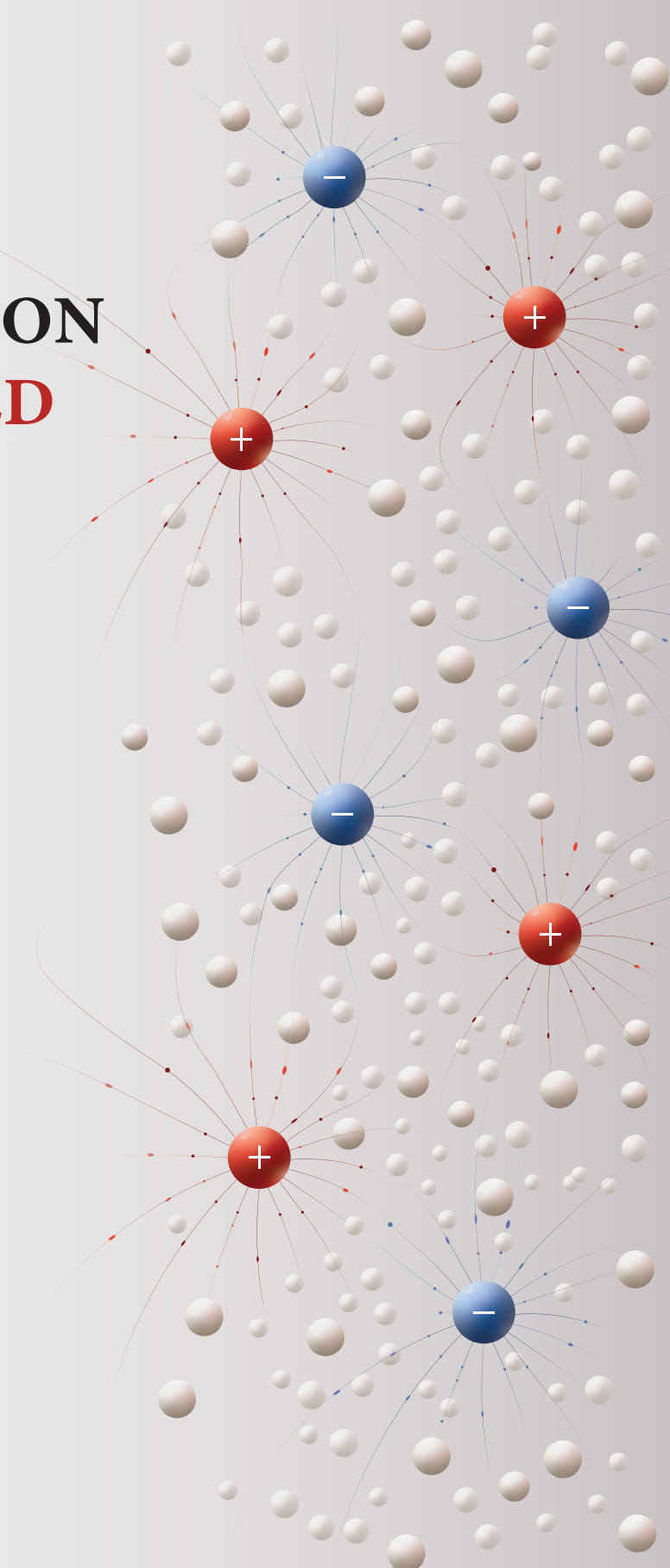
FLUIDIZATION OF CHARGED PARTICLES

Discrete Particle
Simulations and Experiments



Marzieh Kordnejad
Chemical Process Intensification
Eindhoven University of Technology

DOCTORAL THESIS

TU/e EINDHOVEN UNIVERSITY OF TECHNOLOGY

Fluidization of Charged Particles

Discrete Particle Simulations and Experiments

Marzieh Kordnejad

Copyright © 2026 by Marzieh Kordnejad, Eindhoven, The Netherlands.

All rights reserved. No part of the material protected by this copyright notice may be reproduced or utilised in any form or by any means, electronic or mechanical, including photocopying, recording or by any information storage and retrieval system, without the prior permission of the author.

A catalogue record is available from the Eindhoven University of Technology Library
ISBN: 978-90-386-6792-8
Printed by: ProefschriftMaken, Utrecht

Fluidization of Charged Particles

Discrete Particle Simulations and Experiments

PROEFSCHRIFT

ter verkrijging van de graad van doctor aan de Technische Universiteit Eindhoven, op gezag van de rector magnificus prof.dr. S.K. Lenaerts, voor een commissie aangewezen door het College voor Promoties, in het openbaar te verdedigen op donderdag 08 oktober 2026 om 13:30 uur

door

Marzieh Kordnejad

geboren te Eizeh, Iran

Dit proefschrift is goedgekeurd door de promotoren en de samenstelling van de promotiecommissie is als volgt:

voorzitter:	prof.dr. A. Forner Cuenca
1^{e} promotor:	prof.dr.ir. M. van Sint Annaland
copromotor:	dr.ir. I. Roghair
leden:	prof.dr.ir. J.A.M. Kuipers
	prof.dr.ir. J.R. van Ommen (Technische Universiteit Delft)
	prof.dipl.ing.dr. S. Heinrich (Hamburg University of Technology)
	prof.dr. P. Mehrani (University of Ottawa)
	dr.ing. C.M. Venier (National Scientific and Technical Research Council)

Het onderzoek dat in dit proefschrift wordt beschreven is uitgevoerd in overeenstemming met de TU/e Gedragscode Wetenschapsbeoefening.

Summary

Electrostatic charging caused by triboelectrification is an inherent phenomenon in gas–solid fluidized beds containing insulating particles and can significantly influence hydrodynamics, particle motion, fouling, and heat transfer. Although electrostatic effects are frequently observed in industrial fluidized-bed processes such as polymer drying, coating, and granulation, they are often treated as secondary disturbances rather than as governing forces that directly influence reactor performance. This thesis combines numerical modeling and experimental investigations to improve the understanding of electrostatic phenomena in fluidized beds and their implications for industrial applications.

The thesis begins by reviewing the physical mechanisms responsible for triboelectric charging, including conductor–conductor, conductor–insulator, and insulator–insulator contact electrification. The influence of electrostatic interactions on fluidization behavior is discussed together with existing experimental and numerical studies, highlighting the remaining challenges in accurately predicting charged particulate systems.

The first part of the thesis focuses on the numerical modeling of electrostatic interactions in CFD–DEM simulations. Because direct Coulomb-force calculations scale quadratically with the number of particles, they rapidly become computationally prohibitive for industrial-scale simulations. To overcome this limitation, a hierarchical particle-cell method is developed in which short-range electrostatic interactions are evaluated directly using Coulomb's law, while long-range interactions are efficiently approximated using lumped charges within computational cells. Validation against exact Coulomb-force calculations for a three-dimensional fluidized bed containing 70,000 charged particles demonstrates that the proposed method substantially improves the accuracy of electrostatic force predictions while maintaining computational efficiency. Consequently, the method provides an efficient and reliable framework for incorporating long-range electrostatic interactions into large-scale CFD–DEM simulations.

The developed numerical framework is subsequently applied to investigate the influence of electrostatic charging on fluidized-bed hydrodynamics.

The simulations demonstrate that electrostatic interactions increase the minimum fluidization velocity, delay bubble formation, reduce the measured bubble area, modify particle circulation patterns, and increase bed voidage. The contour plots further indicate that charged bubbles become more elongated while their boundaries become increasingly diffuse because of particle penetration. These changes arise because electrostatic forces become comparable to gravitational and drag forces, fundamentally altering the force balance governing particle motion.

Experimental investigations using a pseudo-two-dimensional fluidized bed containing Geldart B glass particles confirm the numerical observations. Charge accumulation measured using a Faraday cup resulted in an approximately 33% increase in the minimum fluidization velocity under dry conditions compared with humidified conditions, where electrostatic charging was largely suppressed. Bubble characteristics were also significantly modified. Bubble-area analysis showed a reduction in the measured bubble area, while contour analysis revealed more elongated bubbles with increasingly diffuse gas–solid interfaces due to particle penetration. Together, the numerical and experimental results demonstrate that electrostatic charging has a pronounced influence on fluidization behavior.

The final part of the thesis investigates the consequences of electrostatic charging for fouling and heat-transfer performance in fluidized beds containing HDPE particles. Measurements of charge density, fouling mass, and heat-transfer coefficient demonstrate a clear relationship between electrostatic charging, particle deposition, and thermal performance. Particle groups exhibiting higher charge accumulation, particularly smaller particles (fines) or with a larger particle size distribution produced greater fouling on the grounded heating element and consequently lower heat-transfer coefficients. The measured heat-transfer coefficient progressively decreased during operation to less than half of the theoretical value predicted by the Molerus correlation for a clean fluidized bed. Comparison of particle groups further demonstrates that increased electrostatic charging promotes fouling formation, thereby increasing the thermal resistance between the heating surface and the fluidized particles and reducing heat-transfer performance.

Overall, this thesis demonstrates that electrostatic interactions cannot be regarded as secondary effects in gas–solid fluidized beds. Electrostatic charging directly influences fluidized-bed hydrodynamics, fouling formation, and heat-transfer performance. By combining an accurate and computationally efficient electrostatic modeling framework with comprehensive experimental validation, this work provides new insight into the mechanisms governing charged particulate systems and establishes a foundation for more predictive CFD–DEM simulations and improved industrial fluidized-bed design and operation.

Contents

Summary i

Contents iii

List of Figures v

List of Tables xi

1 Introduction 1
- 1.1 Motivation . . . 1
- 1.2 Scope of the Thesis . . . 2
- 1.3 Fundamentals of Gas–Solid Fluidized Beds . . . 2
- 1.4 Electrostatics as A Governing Force . . . 4
- 1.5 Tribo-Electrification . . . 5
- 1.6 Influence on Fluidization Processes . . . 11
- 1.7 Previous Work and Knowledge Gaps . . . 13
- 1.8 Thesis Outline . . . 15

2 Long-range Electrostatic Interaction Forces in Discrete Particle Simulations 17
- 2.1 Introduction . . . 18
- 2.2 Discrete Particle Model framework . . . 22
- 2.3 Results and Discussion . . . 29
- 2.4 Conclusion . . . 39

3 Numerical investigation of the hydrodynamics of fluidized bed charged particles 43
- 3.1 Introduction . . . 44
- 3.2 Discrete Particle Model . . . 47
- 3.3 Minimum Fluidization and Bubbling Velocity . . . 49
- 3.4 Bubble Dynamics . . . 55
- 3.5 Particle Dynamics . . . 62
- 3.6 Discussion . . . 67

3.7 Conclusions 69

4 Experimental study of electrostatic charge effect on hydrodynamics of gas-solid fluidized beds 71
4.1 Introduction 72
4.2 Experimental Methods and Materials 74
4.3 Results & Discussion 81
4.4 Conclusions 102

5 Heat transfer coefficient in the presence of fouling 105
5.1 Introduction 106
5.2 Experimental Setup 108
5.3 Results and Discussion 110
5.4 Conclusion 119

Appendix A: Particle Size Distributions 121

6 Discussion and Conclusions 125
6.1 Summary and Comparative Analysis 126
6.2 Industrial Relevance 127
6.3 Evaluation of Modeling Approaches and Methodological Contributions 127
6.4 Outlook 128

Bibliography 131

Acknowledgements 145

Curriculum Vitae 147

List of Figures

1.1 Evolution of gas–solid fluidization regimes with increasing gas velocity, ranging from fixed bed to bubbling, slugging, turbulent, and lean-phase transport (Kunii et al. 1994). 3
1.2 Geldart's classifications (Geldart 1973) 4
1.3 Energy-level representation of contact electrification between two metallic surfaces. Electron transfer occurs upon contact until Fermi level alignment is achieved. Upon separation, charge is retained due to the contact potential difference and finite capacitance (Lowell et al. 1980). 7
1.4 Conceptual illustration of contact electrification between two insulating materials. Charge transfer occurs via electron tunneling between localized surface states at nanoscale asperity contacts, followed by charge trapping upon separation (Matsusaka et al. 2010). 10
1.5 Examples of volcanic lightning observed during explosive eruptions at several volcanoes worldwide, illustrating the occurrence of electrical discharges within volcanic ash plumes (Cimarelli et al. 2022) 11
1.6 Particle deposition on reactor walls in gas–solid fluidized beds. (a) Representative photograph of polymer particle deposition observed in the present laboratory experiments. (b) Schematic illustration of the development of particle deposition due to electrostatic interactions. 12

2.1 Geometrical parameters of two charged particles 25
2.2 Schematic of the Verlet list method 25
2.3 Screened-force method 27
2.4 Hybrid method 27

2.5 Two different modified hybrid computation methods to reduce computational cost. Method 1: Considering the charge cell centers of the target cell location to calculate the distance to the lumped particles. Method 2: Multi-grid sizes for the lumped particles, with coarser grids used for particles farther from the target. 28
2.6 (a) Average and maximum relative errors obtained using the screened-force method for different values of the screening criterion α. (b) Illustration of the screened-force method for $\alpha = 1\%$ and $\alpha = 0.05\%$. A decrease in α increases the cut-off radius and the number of particles included in the electrostatic force calculation. 31
2.7 (a) Average and maximum relative errors obtained using the hierarchical particle-cell method for different numbers of surrounding cell layers. (b) Schematic representation of the hierarchical particle-cell method. Electrostatic interactions within $\Gamma_{f,\text{direct}}$ are evaluated using direct Coulomb calculations, whereas interactions outside this region are approximated using lumped charges in $\Gamma_{f,\text{lumped}}$ and Γ_c. 32
2.8 Snapshots of the three different methods described in this study. In the hybrid method, particles experience stronger electrostatic forces compared to the screened-force method, causing them to spread more throughout the bed. Additionally, particles in the hybrid method, like those in the exact method, are observed to adhere to the walls. This behavior is similar to the results obtained using the exact evaluation method, which provides a more accurate representation of the system's dynamics. 34
2.9 Time-averaged granular temperature. 36
2.10 Axial distribution of time-averaged granular temperature along the axial direction for the screened force, hybrid, and exact interaction methods. The inset shows the cumulative distribution function (CDF) of granular temperature over all available computational cells at the same time instant. The CDF represents the fraction of cells with granular temperature below a given value. 37
2.11 Circulation pattern 38

3.1 Hierarchical particle–cell method representation for electrostatic force calculations. The computational domain is divided into three zones: (1) $\Gamma_{f,\text{direct}}$: Zone for direct particle-particle Coulombic calculations involving the target particle (red particle) and nearby real particles; (2) $\Gamma_{f,\text{lumped}}$: Zone for fine-grid calculations using lumped particle approximations; (3) Γ_c: Coarse-grid zone where long-range interactions are computed using lumped particle methods. 50

3.2 Pressure drop as a function of superficial gas velocity for the uncharged bed. The intersection of the fixed-bed and fluidized-bed regions gives the minimum fluidization velocity. 52
3.3 Pressure drop as a function of superficial gas velocity for uncharged and charged particle beds. 53
3.4 Time-averaged solids holdup at different bed heights for uncharged and charged particle systems. 55
3.5 Contours of solids volume fraction during single-bubble rise: (a) uncharged particles, (b) 0.5% charged particles and (c) 1% charged particles. 57
3.6 Comparison of single-bubble evolution for different particle charge levels in a bed with increased height: (a) uncharged, (b) 0.5%, (c) 1%, and (d) 2% of the maximum particle charge. 59
3.7 Evolution of bubble area during bubble rise for different particle charge levels. 60
3.8 Snapshots of uncharged and charged fluidized beds, coloured according to the magnitude of the electrostatic force acting on each particle, with blue indicating low electrostatic forces and red indicating high electrostatic forces: (a) Uncharged bed, wall section (b) Charged bed wall section (c) Uncharged bed, interior section (d) Charged bed, interior section. 63
3.9 Time-averaged particle circulation patterns for uncharged and charged systems. 64
3.10 Comparison of circulation patterns obtained with and without particle–wall electrostatic interactions. 66
3.11 Time-averaged granular temperature distributions for uncharged and 1,3 pC charged particles in fluidized beds. 67

4.1 Experimental set-up schematics. 75
4.2 Experimental set-up parts overview. 76
4.3 Correlation between the normalized pixel intensity and the 3D solids porosity. 78
4.4 Example of the image conversions in the DIA script. A shows the normalized pixel intensity. B shows the solid porosity. C shows the binary image and D shows the bubble overlay on the original image. 79
4.5 Consecutive measurements of a charged copper object suspended by a non-conductive Nylon thread moving into and out of the Faraday cup five times consecutively 80
4.6 Results of multiple charge density measurements at different operating conditions. 81
4.7 Comparison of minimum fluidization velocity in case of using humidified nitrogen gas (less/no charged particles) and dry nitrogen gas (charged particles). 85

4.8 The difference in solid holdup between a charged and uncharged bed required to explain the difference in pressure drop slope during the fixed-bed state. 86
4.9 Investigation of U_{mb} for an uncharged bed. Bubble formation shown at different superficial velocities, A) shows 1.0 U_{mf} B) shows 1.05 U_{mf} C) shows 1.1 U_{mf} and D) shows 1.2 U_{mf}. . . . 87
4.10 Investigation of U_{mb} for a charged bed. Bubble formation shown at different superficial velocities, A) shows 0.9 U_{mf}, B) shows 1.0 U_{mf}, C) shows 1.1 U_{mf} and D) shows 1.2 U_{mf}. 88
4.11 Sectional pressure drop for uncharged (black) and charged (red) bed. 88
4.12 Average bubble diameter in the uncharged bed (black) and charged bed (red) as function of the height in the bed. 89
4.13 Average bubble area in the uncharged bed (black) and charged bed (red) as function of the bubble height in the bed. 90
4.14 Average bubble aspect-ratio (bubble width over bubble height) for an uncharged bed (black) and charged bed (red). 91
4.15 Paths of bubbles in an uncharged bed with an injection volume of 50.0 mL. 92
4.16 Paths of bubbles in a charged bed with an injection volume of 50.0 mL. 92
4.17 Percentage of bubbles that are split over the vertical position. The percentage is taken from the 30 bubble recordings for each case. 93
4.18 Average bubble rise velocity in an uncharged bed (black) and charged bed (red). 94
4.19 Average bubble area in uncharged bed (black) and charged bed (red) as a function of the height in the bed with a smaller injection volume of 33.3 mL. 95
4.20 Bubbles forming in multiple locations during bubble injection with a 33.3 mL injection volume in a charged bed. 96
4.21 Average bubble area in uncharged bed (black) and charged bed (red) as function of the height in the bed when the same background velocity was used (0.191 $\mathrm{m\,s^{-1}}$) with an injection volume of 66.7 mL. 97
4.22 Equivalent bubble diameter over the height for 1.3, 1.6 and 2.0 times U_{mf} in an uncharged bed compared to the correlation by Shen et al. (2004) 98
4.23 Equivalent bubble diameter over the height for 1.3, 1.6 and 2.0 times U_{mf} in a charged bed compared to the correlation by Shen et al. (2004) 98
4.24 The equivalent bubble diameter in a freely bubbling bed in case of an uncharged bed (black) and charged bed (red) when the gas flow rate is very similar (50.9 and 51.2 l/min respectively). 99
4.25 Average visual bubble flow for an uncharged bed at 1.3 U_{mf} (A), 1.6 U_{mf} (B) and 2.0 U_{mf} (C). 100

4.26 Average visual bubble flow rate for a charged bed at 1.3 U_{mf} (A), 1.6 U_{mf} (B) and 2.0 U_{mf} (C). 100
4.27 Particles attracting each other on the walls at the bed surface. 101
4.28 Formation of a bridge (at top of the bed) during switching from high gas flow to minimum fluidization gas flow. 102
4.29 Collapse of the bridge after gas flow is turned off after 1 second (B). 102

5.1 Schematic of the experimental setup: gas-solid fluidized bed including a central electric heating element. 109
5.2 Photograph of the laboratory-scale fluidized-bed apparatus showing the fluidization column, thermocouple connections, and heating-element power controller 110
5.3 Particle size distribution of sieved particles with 180 to 220 µm 111
5.4 Representative photographs of polymer deposition observed after the fluidization experiments: (a) polymer deposits on the cartridge heating element and (b) polymer deposition on the inner wall of the fluidized-bed reactor. 112
5.5 Charge of bulk and fouling particles fluidized at different temperatures 112
5.6 Average charge density of the investigated particle groups at different superficial gas velocities. 114
5.7 Average fouling mass deposited on the heating element for the investigated particle groups at different superficial gas velocities. 114
5.8 Temperature evolution of the heating element surface and the fluidized bed during the experiment with an 80°C heater setpoint. Nitrogen was supplied at a superficial gas velocity of 2.86 $m\,s^{-1}$ using unsieved HDPE particles. 116
5.9 Comparison between the experimentally measured heat-transfer coefficient and the theoretical value predicted by the Molerus correlation for a clean fluidized bed. 118
5.10 Measured heat-transfer coefficients for the investigated HDPE particle groups at different superficial gas velocities. 118
5.11 The PSD of unsieved particles 121
5.12 The PSD of sieved particles, Below 180µm fraction 122
5.13 The PSD of sieved particles, 180–224 µm fraction 122
5.14 The PSD of sieved particles, 224-300µm fraction 123
5.15 The PSD of sieved particles, upper 300µm fraction 123

List of Tables

1.1 Representative triboelectric series indicating the qualitative tendency of selected materials to acquire positive or negative charge after contact and separation. The ordering is based on empirical observations and serves as a qualitative guideline rather than a universal ranking (Adams 1987). 6

2.1 An overview of computational studies on electrostatic force calculation methods used in an Eulerian-Lagrangian model of gas-solid fluidized bed 20
2.2 Summary of equations in the DPM model for the simulation of gas-solid fluidized beds 23
2.3 Simulation parameters 30
2.4 Percentage error and CPU time for different electrostatic force computation methods for a gas-solid fluidized bed with 70,000 charged particles. 39

3.1 Simulation parameters 52

4.1 Camera and software settings. 78

5.1 HDPE particle size distribution and experimentally measured minimum fluidization velocities of the investigated particle groups. 109

CHAPTER 1

Introduction

1.1 Motivation

Gas–solid fluidized beds are key unit operations in the chemical, petrochemical, energy, food, and pharmaceutical industries, where they are employed in catalytic cracking, combustion, drying, polymerization, coating processes, and many other processes. Their widespread use is rooted in their excellent gas–solid contact, high heat and mass transfer rates, and effective solids mixing, even at industrial scales (Kunii et al. 1994). These characteristics make fluidized beds particularly suitable for highly exothermic reactions and thermally sensitive particulate systems, as emphasized in practical design and operational studies (Cocco et al. 2014).

From a physical standpoint, gas–solid fluidization represents a transition from a static granular packing to a dynamically evolving multiphase system driven by an upward-flowing gas. Classical fluidization theory describes this transition in terms of a balance between gravitational forces, gas–particle drag, and inter-particle collisions (Hoomans et al. 1996; Kunii et al. 1991). Above the onset of fluidization, excess gas forms bubbles that rise through the particulate phase and generate large-scale circulation patterns, which govern mixing, transport, and reactor performance (Mori et al. 1975). Despite the success of this framework, industrial fluidized beds frequently exhibit behaviors that cannot be explained solely by hydrodynamic forces. One of the most persistent and industrially relevant phenomena is the accumulation of electrostatic charge due to triboelectric effects. Bailey (1993) demonstrated early on that powder handling processes are intrinsically prone to charge generation, while Matsusaka et al. (2010) showed that triboelectric charging is unavoidable in gas–solid flows involving insulating materials. In fluidized beds, the resulting electrostatic forces can reach magnitudes comparable to gravitational and drag forces, thereby fundamentally altering the force balance that governs the overall fluidization behavior (Fotovat et al. 2017a). Understanding these electrostatic effects is therefore essential for accurate prediction of fluidization behavior and for mitigating operational problems such as agglomeration, wall fouling, and heat-transfer degradation.

1.2 Scope of the Thesis

This thesis focuses on electrostatic phenomena in gas–solid fluidized beds, with particular emphasis on understanding how triboelectric charging influences particle hydrodynamics, bubble dynamics, wall fouling, and heat transfer. The work combines numerical modeling and experimental investigations to provide a comprehensive understanding of electrostatic interactions across different length scales.

The numerical part addresses the development of physically consistent and computationally efficient models for long-range electrostatic interactions in Discrete Particle Method (DPM) simulations and their application to charged gas–solid fluidized beds. The experimental part focuses on quantifying the influence of electrostatic charging on fluidization behavior and heat transfer performance under controlled operating conditions.

Together, these complementary numerical and experimental investigations provide a unified framework for understanding, modeling, and evaluating the role of electrostatic interactions in gas–solid fluidized beds.

1.3 Fundamentals of Gas–Solid Fluidized Beds

Fluidization occurs when a bed of granular solids is subjected to an upward gas flow exceeding the minimum fluidization velocity, u_{mf}. Below this threshold, the gas percolates through the voids of the packed bed while the solid phase remains mechanically stable. As gas velocity increases, drag forces progressively counterbalance the effective weight of the particles until mechanical equilibrium is reached and fluidization initiates (Ergun 1952; Kunii et al. 1994). As illustrated in Figure 1.1, beyond incipient fluidization, the bed typically enters the bubbling regime, in which gas in excess of that required for particle suspension forms discrete bubbles. These bubbles grow, coalesce, and rise through the emulsion phase, inducing macroscopic circulation that enhances mixing and transport (Kunii et al. 1994).

Particle properties exert a decisive influence on fluidization behavior. A widely used classification of particles was proposed by Geldart (1973), based on particle size and the density difference between the solid and gas phases (See Figure 1.2).

Geldart classified particles into four groups, commonly referred to as Groups A–D, each exhibiting characteristic fluidization behavior. Very fine powders (Group C) are dominated by cohesive inter-particle forces and are difficult to fluidize. Group A particles fluidize smoothly and exhibit controlled bubble growth. Group B particles display vigorous bubbling behavior, while large and dense Group D particles require high gas velocities and often show unstable or spouting behavior. This classification remains a cornerstone for interpreting gas–solid fluidization behavior and is discussed extensively in classical fluidization texts (Geldart 1973; Kunii et al. 1994).

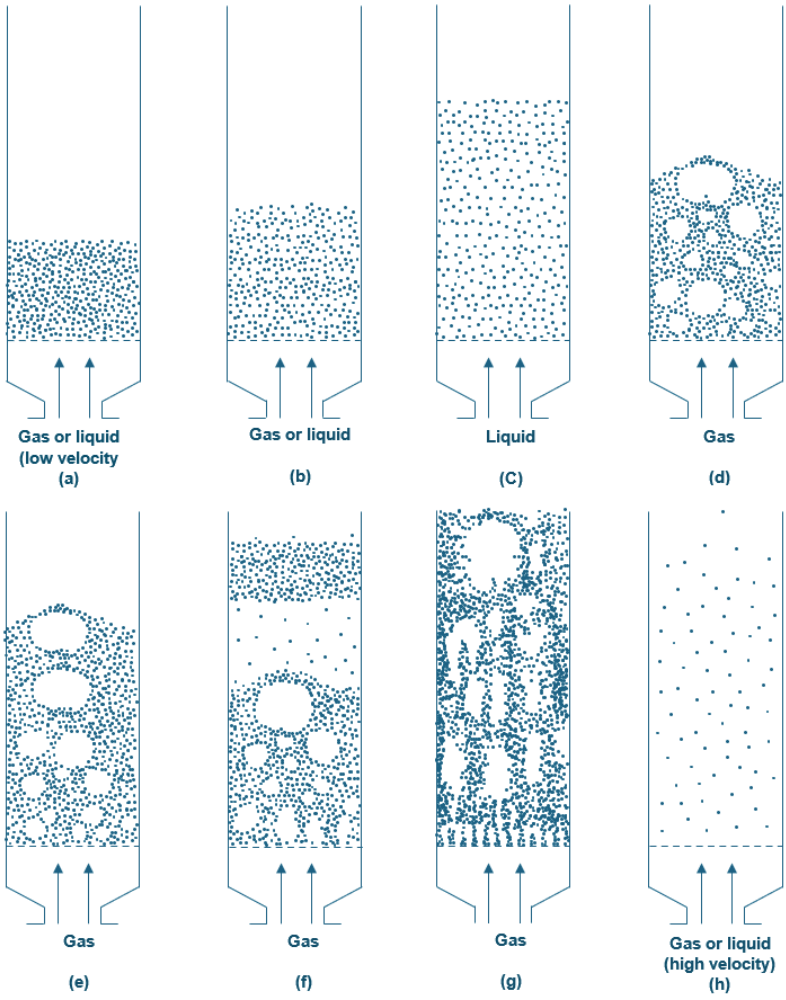


Figure 1.1: Evolution of gas–solid fluidization regimes with increasing gas velocity, ranging from fixed bed to bubbling, slugging, turbulent, and lean-phase transport (Kunii et al. 1994).

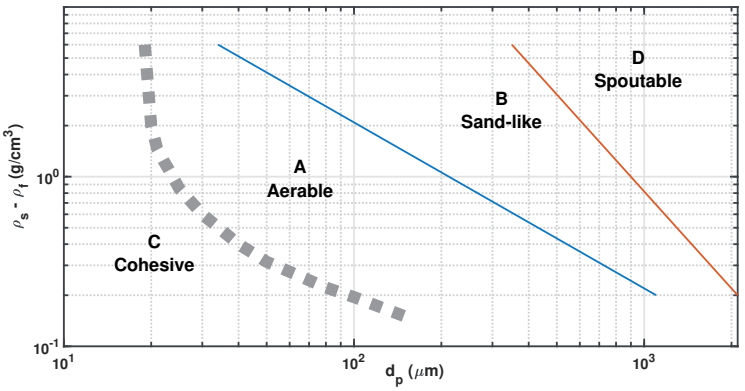


Figure 1.2: Geldart's classifications (Geldart 1973)

Figure 1.2 illustrates the qualitative differences in fluidization behavior associated with each particle group. It is important to note that classical fluidization theory and correlations derived for these groups implicitly assume electrically neutral particles and short-range mechanical interactions. Electrostatic forces, which are neglected in this framework, can therefore fundamentally alter the expected behavior for each Geldart group when insulating or polymeric materials are involved.

1.4 Electrostatics as A Governing Force

Electrostatic forces differ fundamentally from hydrodynamic and gravitational forces in both their origin and scaling behavior. While drag and collision forces depend primarily on gas velocity, particle size, and solids concentration, electrostatic forces are governed by charge magnitude, spatial charge distribution, and the dielectric properties of the surrounding medium (Joseph et al. 1983).

As a consequence, electrostatic interactions exhibit a fundamentally different range and persistence compared to mechanical forces. In particular, electrostatic forces can act over longer distances and remain significant even in regions where hydrodynamic forcing is weak, such as near minimum fluidization conditions or within dense particle assemblies.

Experimental studies have demonstrated that charge accumulation in fluidized beds depends strongly on particle material, surface properties, and operating conditions (Mehrani et al. 2005). In addition, electrostatic interactions have been shown to influence macroscopic bed behavior, including bed expansion, solids circulation patterns, and wall fouling (Fotovat et al. 2017a). In certain cases, the magnitude of electrostatic forces can become comparable to gravitational and drag forces, thereby modifying the effective force balance that governs particle motion.

These observations indicate that electrostatic interactions should not be treated merely as secondary perturbations to hydrodynamics. Instead, they constitute an additional governing force that can fundamentally alter fluidization behavior, particularly in systems involving fine, insulating, or polymeric particles. This shift in perspective is essential for accurately describing and predicting the behavior of industrial fluidized beds where triboelectric charging is unavoidable.

1.5 Tribo-Electrification

Tribo-electrification refers to the generation of electrical charge during contact and subsequent separation between dissimilar materials. In gas–solid systems, this process is continuously driven by repeated particle–particle and particle–wall collisions, where mechanical interactions such as impact, sliding, and deformation lead to charge transfer at the contact interface (Bailey 1993). A qualitative overview of material charging tendencies is commonly provided by a *triboelectric series*, which ranks materials according to their observed tendency to acquire positive or negative charge upon contact and separation. Such series are based on empirical observations and are frequently used as a conceptual tool in the analysis of triboelectric phenomena in particulate systems.

Table 1.1 illustrates that many materials relevant to industrial fluidized beds exhibit distinct qualitative charging tendencies. It is important to emphasize, however, that triboelectric series do not provide quantitative predictions of charge magnitude or distribution. The relative ordering of materials may vary with surface roughness, contamination, humidity, temperature, and contact history. Nevertheless, the triboelectric series remains a useful conceptual framework for interpreting and comparing charging behavior in complex particulate systems.

Physical Origin of Charge Transfer

At the microscopic level, triboelectric charging is governed by differences in electronic energy states between contacting materials. When two materials come into contact, charge redistribution occurs in order to reach electrostatic equilibrium.

For conductive materials, charge transfer is primarily governed by differences in work function. The work function is defined as the minimum energy required to remove an electron from a material surface to vacuum. A closely related concept is the Fermi level, which represents the highest occupied electronic energy level at absolute zero temperature and can be interpreted as the electrochemical potential of the electrons. When two conductors with different work functions are brought into contact, electrons transfer from the material with the higher Fermi level (lower work function) to the material with the lower Fermi level until the Fermi levels become equal.

Table 1.1: Representative triboelectric series indicating the qualitative tendency of selected materials to acquire positive or negative charge after contact and separation. The ordering is based on empirical observations and serves as a qualitative guideline rather than a universal ranking (Adams 1987).

Material	Positive charge
Air	
Human hands	
Asbestos	
Rabbit fur	
Glass	
Mica	
Human hair	
Nylon	
Wool	
Fur	
Lead	
Silk	
Aluminum	
Paper	
Cotton	Zero reference
Steel	
Wood	
Amber	
Sealing wax	
Hard rubber	
Nickel, Copper	
Brass, Silver	
Gold, Platinum	
Sulfur	
Acetate, Rayon	
Polyester	
Polystyrene foam (Styrofoam)	
Orlon	
Saran	
Polyurethane	
Polyethylene	
Polypropylene	
Vinyl (PVC)	
Silicon	
Teflon	Negative charge

Upon separation, a residual charge remains on each surface, the magnitude of which depends on the separation distance and system capacitance (Harper 1951; Lowell et al. 1980).

For insulating materials, the mechanism is more complex because electrons are not freely mobile throughout the bulk material. Instead, charge transfer is generally attributed to localized surface states within the band gap, which arise from defects, impurities, adsorbed molecular species, and structural disorder. Electrons may tunnel between these localized states during contact, leading to charge accumulation after separation (Lacks et al. 2011; Lowell 1979).

Contact Electrification Mechanisms

Conductors Contacts

In metal–metal contacts, electron transfer occurs via tunneling until thermodynamic equilibrium is reached. The resulting charge after separation is related to the contact potential difference:

$$\Delta q = C_0 \frac{(\Phi_2 - \Phi_1)}{e} \tag{1.1}$$

where C_0 is the capacitance at separation distance, and Φ is the work function (Matsusaka et al. 2003). Figure 1.3 illustrates this process in terms of energy level alignment.

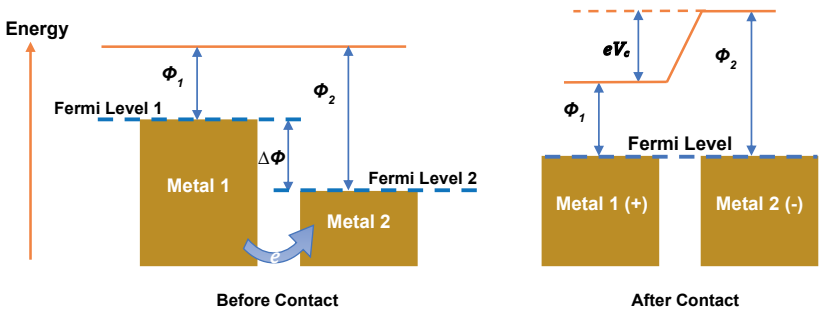


Figure 1.3: Energy-level representation of contact electrification between two metallic surfaces. Electron transfer occurs upon contact until Fermi level alignment is achieved. Upon separation, charge is retained due to the contact potential difference and finite capacitance (Lowell et al. 1980).

Conductor–Insulator Contacts

In conductor–insulator contacts, electron transfer occurs between the delocalized electronic states of the conductor and localized surface states of the insulator. Unlike conductor–conductor contacts, only the electronic states near the contact interface participate in charge transfer because electrons cannot move freely through the insulating material. Consequently, complete Fermi level equilibration does not occur, and the transferred charge remains trapped in localized surface states after separation (Lacks et al. 2011; Lowell et al. 1980).

The driving force for charge transfer is the mismatch in electronic energy levels between the contacting materials. When contact is established, electrons tunnel from energetically favorable occupied states in the conductor to accessible empty surface states in the insulator, thereby reducing the total free energy of the system.

Experimental studies have shown that the net transferred charge in conductor–insulator systems often scales approximately with the difference in effective work function between the contacting materials, suggesting that electron transfer remains the dominant mechanism governing charge exchange (Harper 1951; Matsusaka et al. 2000). However, this relationship is not strictly universal and should be interpreted as a first-order approximation.

Single-particle impact experiments, in which insulating or polymeric particles collide with metallic surfaces, have further demonstrated that both impact velocity and particle deformation significantly influence the magnitude of transferred charge. These effects are typically attributed to variations in real contact area and contact duration, which enhance the probability of electron tunneling between the metal surface and localized insulator states (Matsusaka et al. 2010; Matsusaka et al. 2000).

Under these assumptions, the transferred charge can be expressed in a phenomenological form as:

$$\Delta q \propto \frac{(\Phi_2 - \Phi_1)}{e}, \tag{1.2}$$

where Φ_1 and Φ_2 denote the effective work functions of the conductive and insulating materials, respectively, and e is the elementary charge. This relation captures the primary thermodynamic driving force for electron transfer but does not represent a universal law, as the actual charge magnitude is strongly influenced by surface chemistry, environmental conditions, and repeated contact history (Lacks et al. 2011; Lowell et al. 1980).

Insulator–Insulator Contact Electrification

The charging mechanisms in insulator–insulator contacts remain less well understood compared to conductor-involving systems, primarily due to the absence of free charge carriers and the strong influence of surface states and

environmental conditions. Nevertheless, a growing body of experimental and theoretical work suggests that charge transfer in such systems arises from a combination of electron transfer, ion exchange, and material transfer processes occurring at the microscopic contact interface (Lacks et al. 2011; Lowell et al. 1980).

In insulating materials, the concept of a well-defined Fermi level is not strictly applicable. Instead, charge transfer is governed by localized surface energy states, which may originate from structural defects, trapped charges, adsorbed molecular layers, and chemical heterogeneities. When two insulating surfaces come into contact, electrons can tunnel between these localized states if the separation distance is sufficiently small, typically at nanometer-scale asperity contacts.

In addition to electron transfer, ion transfer mediated by adsorbed water layers has been proposed as an important charging pathway, particularly under humid conditions. Furthermore, mechanical deformation during collision can lead to localized material exchange, which may also contribute to net charge redistribution between surfaces. The relative importance of these mechanisms depends strongly on material pair, surface roughness, contact history, and ambient conditions such as humidity and gas composition.

Experimental studies using repeated particle–particle collisions and controlled impact experiments have demonstrated that charge accumulation in insulating systems is highly stochastic and history-dependent. Unlike conductor-involving contacts, no simple universal scaling law exists that links charge magnitude directly to material properties alone. Instead, charge transfer exhibits strong variability even under nominally identical conditions, reflecting the sensitivity of insulator surfaces to microscopic and environmental fluctuations (Lacks et al. 2011; Matsusaka et al. 2010).

Despite this complexity, electron transfer between localized surface states is generally considered the dominant mechanism in dry conditions, as supported by observations of polarity reversal and systematic charge exchange in controlled experiments.

Figure 1.4 illustrates the conceptual mechanism of charge transfer between insulating materials, highlighting the role of localized surface states and nanoscale contact points in facilitating electron tunneling.

From the perspective of gas–solid fluidized beds, insulator–insulator charging is particularly important, as many industrially relevant particles (e.g. polymers, ceramics, and glass) behave as electrical insulators. In such systems, continuous and repeated collisions lead to cumulative charge build-up, which can significantly modify inter-particle forces, promote agglomeration, and alter macroscopic flow structures.

Relevance to gas–solid fluidized beds

In gas–solid fluidized beds, triboelectric charging is a continuous stochastic process driven by repeated particle–particle and particle–wall collisions.

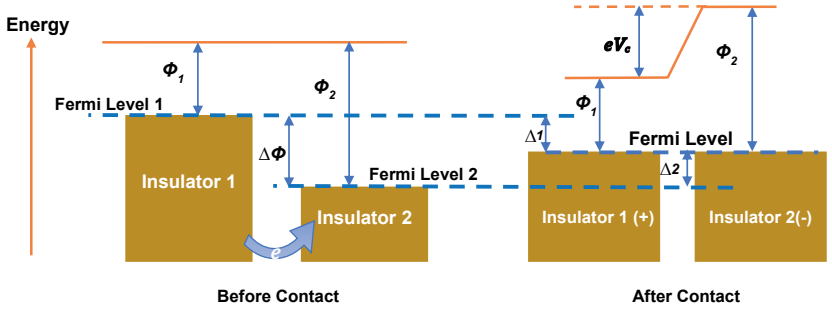


Figure 1.4: Conceptual illustration of contact electrification between two insulating materials. Charge transfer occurs via electron tunneling between localized surface states at nanoscale asperity contacts, followed by charge trapping upon separation (Matsusaka et al. 2010).

Unlike controlled laboratory experiments, these interactions involve a broad distribution of impact velocities, contact geometries, and material pairings.

As a result, charge accumulation in fluidized beds is spatially and temporally heterogeneous. Local electric fields can develop within the bed, introducing additional inter-particle forces that may be attractive or repulsive depending on charge polarity.

These effects can significantly influence particle clustering, collision dynamics, and macroscopic flow structures, thereby coupling particle-scale electrostatic phenomena to bulk hydrodynamic behavior.

Natural example: volcanic ash charging

Explosive volcanic eruptions provide one of the most striking natural manifestations of particle electrification in dense gas–solid flows. Volcanic ash consists primarily of fragmented silicate minerals and glassy particles that behave as electrical insulators. During an eruption, magma fragmentation generates vast quantities of ash, while the rapid expansion of the eruption column produces intense particle–particle collisions and turbulent mixing. These processes promote efficient charge generation through a combination of triboelectrification and fracto-electrification, resulting in significant charge accumulation within the volcanic plume.

As charge separation develops, strong electric fields are established inside the ash cloud. When the local electric field exceeds the dielectric breakdown strength of air, electrical discharges occur in the form of volcanic lightning. Figure 1.5 presents representative examples of volcanic lightning observed during explosive eruptions at several volcanoes worldwide.

Field observations from eruptions such as Eyjafjallajökull (2010) and



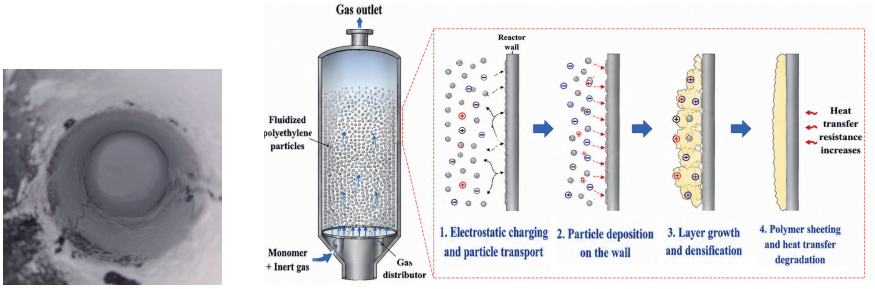
Figure 1.5: Examples of volcanic lightning observed during explosive eruptions at several volcanoes worldwide, illustrating the occurrence of electrical discharges within volcanic ash plumes (Cimarelli et al. 2022)

Redoubt (2009), obtained using ground-based lightning detection networks together with satellite observations, have documented hundreds to thousands of lightning discharges during individual eruptive events (Cimarelli et al. 2022). These observations demonstrate that particle electrification is an intrinsic feature of highly energetic granular flows and provide compelling evidence that electrostatic charge generation can occur over length scales ranging from laboratory and industrial particulate systems to large geophysical phenomena.

1.6 Influence on Fluidization Processes

Triboelectric charging has been widely reported to influence the hydrodynamic behavior of gas–solid fluidized beds by introducing electrostatic forces that act in addition to gravitational, drag, and collisional forces. Electrostatic charges generated by frequent particle–particle and particle–wall collisions give rise to attractive or repulsive interactions, depending on charge magnitude and polarity, thereby modifying local force balances and particle motion (Bailey 1993; Hendrickson 2006; Matsusaka et al. 2010). At the macroscopic scale, such interactions have been associated with particle agglomeration, channeling, particle deposition on walls, and electrostatic discharges, which may pose operational and safety challenges in industrial systems. Particle deposition on reactor walls is one of the most important industrial consequences of electrostatic charging in gas–solid fluidized beds. As illustrated in Figure 1.6, electrostatic particle deposition on reactor walls can progressively develop into continuous polymer layers, reducing heat transfer, disturbing bed hydrodynamics, and potentially leading to operational problems.

One of the most direct manifestations of electrostatic effects on fluidization behavior is their influence on the minimum fluidization velocity,



(a) (b)

Figure 1.6: Particle deposition on reactor walls in gas–solid fluidized beds. (a) Representative photograph of polymer particle deposition observed in the present laboratory experiments. (b) Schematic illustration of the development of particle deposition due to electrostatic interactions.

u_{mf}. Multiple experimental studies have reported an increase in u_{mf} in the presence of charged particles, which has been commonly attributed to electrostatic repulsion between similarly charged particles. These repulsive forces increase the effective bed void fraction and hinder the development of uniform fluidization (Alsmari et al. 2015; Dong et al. 2015; Mehrani et al. 2005). In contrast, the influence of electrostatics on the minimum bubbling velocity, u_{mb}, is less systematic and appears to depend on a combination of particle size, material properties, charge distribution, and bed configuration.

Experimental studies have reported conflicting observations regarding the influence of electrostatic charging on bubble dynamics. Jalalinejad et al. (2016) observed a reduction in bubble size together with an increase in bubble aspect ratio as the particle charge density increased, suggesting that electrostatic interactions suppress bubble growth. Conversely, Tan et al. (2018) reported enhanced bubble growth under different particle properties and operating conditions. These contrasting observations indicate that the influence of electrostatic forces on bubble dynamics is highly sensitive to particle properties, charge distribution, and operating conditions, and that no universal trend has yet been established.

Targeted experimental approaches have provided further insight into these effects. Single-bubble injection experiments combined with high-speed imaging and digital image analysis have enabled the isolation of electrostatic influences on local bed structure. Such studies have revealed that electrostatic forces can modify void fraction distributions and interstitial gas pathways within the emulsion phase, with direct implications for solids circulation, mixing, and mass transfer (Fotovat et al. 2017a; Hogue et al. 2008). These findings suggest that electrostatics affects fluidization not only through global parameters such as u_{mf}, but also through localized alterations of bed morphology and gas–solid interaction pathways.

To capture these complex interactions, numerical models have increasingly incorporated electrostatic forces into fluidized-bed simulations. In Eulerian–Eulerian frameworks, electrostatics is commonly represented through continuum charge-density formulations coupled with Poisson's equation for the electric field, whereas Eulerian–Lagrangian (CFD–DEM) approaches explicitly compute inter-particle electrostatic forces using Coulomb's law. These models enable the prediction of charge distributions, bubble dynamics, and bed expansion under a range of operating conditions (Hassani et al. 2013; Pei et al. 2013; Rokkam et al. 2010). However, the computational expense associated with electrostatic interactions often necessitates simplifying assumptions, which can limit quantitative predictive accuracy and motivate the development of more efficient modeling strategies.

1.7 Previous Work and Knowledge Gaps

Significant research effort has been devoted over the past decades to investigating electrostatic phenomena in gas–solid fluidized beds, and a broad range of experimental and numerical studies have demonstrated that electrostatic charging can strongly influence bed behavior. Nevertheless, despite this body of work, a number of fundamental and practical knowledge gaps remain that limit predictive understanding and industrial applicability.

A substantial portion of the experimental literature has focused on the mechanisms and conditions of charge generation, including the influence of gas velocity, humidity, particle material, and additives on net particle charge (Alsmari et al. 2015; Cheng et al. 2012; Mehrani et al. 2005). While these studies have provided valuable insight into charging trends, they often do not directly link charge accumulation to changes in hydrodynamic behavior or bed stability. As a result, electrostatics is frequently treated as a secondary effect rather than as a force that fundamentally alters the fluidization force balance.

Studies that explicitly investigate the hydrodynamic consequences of electrostatic charging frequently report conflicting results. In particular, contradictory trends have been observed with respect to bubble size, bubble rise velocity, and particle segregation patterns. Some investigations report suppression of bubble growth in charged beds, whereas others observe enhanced coalescence or larger bubbles under different particle or operating conditions (Jalalinejad et al. 2016; Tan et al. 2018). These discrepancies highlight the strong dependence of electrostatic effects on particle properties, charge distribution, and experimental configuration, and indicate that no universal hydrodynamic response to electrostatic charging has yet been established.

A further limitation lies in the experimental characterization of electrostatic charge. Most available measurement techniques, such as Faraday cups and collision probes, provide spatially averaged charge-to-mass ratios (Dong et al. 2015; Mehrani et al. 2005). While such measurements are useful for

quantifying global charge levels, they do not resolve local charge heterogeneities or electric field gradients within the bed. This lack of spatially and temporally resolved charge information hampers the ability to establish clear cause–effect relationships between local electrostatic forces and observed hydrodynamic phenomena such as clustering, bubble deformation, or wall fouling.

On the numerical side, electrostatic effects have been incorporated into fluidized-bed simulations using both Eulerian–Eulerian and Eulerian–Lagrangian (CFD–DEM) approaches. However, many CFD–DEM studies approximate electrostatic interactions using short-range force cut-offs or screened Coulomb potentials in order to maintain computational feasibility (Hassani et al. 2013; Kolehmainen et al. 2016). Such approximations neglect long-range electrostatic interactions and have been shown to introduce significant errors in predicted force magnitudes and particle trajectories, particularly in dense particle systems. Although hybrid modeling strategies that combine direct short-range interactions with field-based representations of long-range electrostatics have been proposed (Grosshans et al. 2017), their application to realistic gas–solid fluidized-bed configurations remains limited.

Finally, despite the clear industrial relevance of electrostatic effects, relatively little work has been devoted to quantitatively linking electrostatic phenomena to practical performance indicators such as fouling, heat transfer degradation, and scale-up behavior. While charge-induced agglomeration and particle deposition are widely recognized as precursors to fouling in polymerization and fine-powder systems (Hendrickson 2006), systematic studies that connect electrostatic properties to thermal performance and long-term operational stability are still scarce.

Taken together, these gaps underscore the need for integrated experimental and numerical approaches that explicitly treat electrostatics as a governing force in gas–solid fluidized beds. Addressing these challenges is essential for improving predictive capability, resolving conflicting observations in the literature, and developing reliable mitigation strategies for industrial fluidized-bed systems involving electrically charged particles.

The numerical investigations in this thesis focus on the influence of electrostatic charge on fluidized-bed behaviour rather than on the mechanisms of charge generation. To systematically isolate and quantify these effects, a controlled numerical configuration is adopted in which particles are assigned a prescribed, uniform charge. This approach enables the influence of electrostatic interactions on fluidization behaviour to be investigated independently of the additional complexities associated with charge generation, transfer, dissipation, and bipolar charge distributions.

1.8 Thesis Outline

The remainder of this thesis systematically addresses the knowledge gaps identified in the preceding sections through a combination of physically consistent numerical modeling and targeted experimental investigations. The chapters are organized to progress from fundamental modeling aspects, through detailed hydrodynamic analysis, to experimentally validated insights and industrially relevant implications.

Chapter 2 presents the development of a CFD-DEM incorporating electrostatic forces suitable for dense gas–solid fluidized beds consisting of electrically insulating particles. The limitations associated with neglecting long-range electrostatic interactions for computational efficiency are critically examined. A hybrid modeling framework that combines short-range particle–particle interactions with long-range field-based electrostatic forces is introduced. The accuracy and computational efficiency of the proposed approach are assessed through systematic numerical simulations.

Chapter 3 utilizes the developed CFD-DEM for charged particles to study the hydrodynamic behavior of charged particle systems, with particular emphasis on particle motion, bed structure, and bubble formation. This chapter elucidates the mechanisms by which electrostatic forces modify classical fluidization behavior.

Chapter 4 presents an experimental investigation of electrostatic effects in gas–solid fluidized beds using glass particles. Single-bubble injection experiments, combined with high-speed imaging and digital image analysis (DIA), are employed to quantify the influence of electrostatics on bubble size, bubble shape, and local bed dynamics. The experimental results provide direct validation of the numerical findings and offer insight into electrostatic effects under controlled conditions.

Chapter 5 investigates the role of electrostatic charging in fouling and heat transfer degradation in fluidized beds containing polyethylene particles. The effects of operating parameters such as temperature, gas velocity, and particle size on the heat transfer coefficient are systematically analyzed. This chapter establishes quantitative links between electrostatic agglomeration, wall fouling, and thermal performance degradation, with direct relevance for industrial reactor design and operation.

Collectively, this thesis advances the fundamental understanding of electrostatic phenomena in gas–solid fluidized beds by explicitly treating electrostatics as a governing force alongside hydrodynamic interactions. By combining mechanistic modeling with experimentally validated observations,

the work provides both predictive tools and practical insights for improving the design, operation, and reliability of industrial fluidized-bed systems involving electrically charged particles.

CHAPTER 2

Long-range Electrostatic Interaction Forces in Discrete Particle Simulations

Abstract

Electrostatic charging is a common phenomenon in gas–solid fluidized beds and can strongly influence hydrodynamics, particle deposition, heat-transfer performance, and operational safety. Accurate prediction of electrostatic interactions remains computationally challenging because direct evaluation of Coulomb forces requires pairwise calculations between all charged particles, making large-scale CFD–DEM simulations prohibitively expensive. Furthermore, the commonly adopted screened-force method neglects long-range electrostatic interactions, potentially compromising the reliable prediction of particle behavior.

This thesis presents a comprehensive numerical and experimental investigation of electrostatic phenomena in gas–solid fluidized beds. A hierarchical particle-cell method is developed to efficiently account for both short-range and long-range electrostatic interactions. The proposed method combines direct Coulomb calculations for nearby particles with a hierarchical cell-based representation of distant particle charges, substantially reducing computational cost while maintaining high predictive fidelity. Compared with the screened-force approach, the proposed method provides markedly improved agreement with reference electrostatic force calculations, offering a significantly more reliable representation of particle interactions while retaining computational efficiency.

The numerical model is subsequently applied to investigate the influence of electrostatic charging on fluidized-bed hydrodynamics and is validated using laboratory-scale experiments.

Both numerical and experimental results demonstrate that electrostatic charging increases the minimum fluidization velocity, increases bed expansion, and suppresses bubble growth due to enhanced electrostatic repulsion between particles. Experimental investigations further demonstrate that electrostatic charging promotes fouling on grounded heating surfaces, resulting in a significant reduction of the heat-transfer coefficient to less than half of the theoretical value predicted for a clean fluidized bed. The combined numerical and experimental findings establish a direct relationship between electrostatic charging, fouling formation, and heat-transfer deterioration.

Overall, this work provides an accurate and computationally efficient framework for modelling electrostatic interactions in fluidized beds while improving the understanding of their influence on hydrodynamics, fouling, and heat transfer. The developed methodology provides a foundation for more predictive CFD–DEM simulations and supports the design and optimization of industrial fluidized-bed processes.

2.1 Introduction

Processes involving the handling of films and powders often experience electrostatic charge build-up due to contact and triboelectric charging (Bailey 1993; Li et al. 2001; Matsusaka 2011; Matsusaka et al. 2003). In gas-solid fluidization processes, in particular, electrostatic charge generation is a common and generally unavoidable phenomenon resulting from frequent particle-wall and particle-particle interactions (Cheng et al. 2012; Chowdhury et al. 2021). This charge accumulation induces attractive or repulsive forces between the particles, significantly influencing the hydrodynamics and motion of the emulsion phase, i.e., the dense particle phase with interstitial gas flow. These electrostatic effects can present several challenges, such as equipment fouling, where charged particles adhere to reactor walls or heating elements, leading to blockages and reduced operational efficiency (Lu et al. 2020; Zhang et al. 2021). Additionally, charge build-up can create safety hazards in industrial applications, as electrostatic discharges may ignite combustible powders, increasing the risk of fires or explosions (Bailey 1993; Fotovat et al. 2018; Hou et al. 2025; Tardos et al. 1983).

Due to these challenges, investigating the effects of electrostatic forces on fluidized bed behavior has become increasingly important. Over the past decade, numerous studies have focused on modeling gas-solid fluidized beds while accounting for electrostatic charging (Chowdhury et al. 2021; Fotovat et al. 2017a). In these models, electrostatics can enter the momentum balance in different ways depending on the level at which the phases are represented. In particle-resolved approaches (e.g., Euler-Lagrange/CFD-DEM), which employ a continuous gas phase and discrete particles (Wang

et al. 2023), electrostatic charge is tracked at the particle level, requiring the electrostatic force on each particle to be evaluated from pairwise charge interactions with other charged particles. In continuum approaches (e.g., Euler-Euler/two-fluid models), which treat both the gas and emulsion phase as interpenetrating continua (Ray et al. 2019), electrostatics is typically introduced through a charge density and an electric field that act on a phase-averaged momentum equation.

Accordingly, in CFD-DEM the electrostatic contribution is commonly evaluated either (i) *explicitly* via direct pairwise Coulomb interactions between particles or (ii) *implicitly* by first computing the electric field from Gauss's law (typically through a Poisson equation) using particle charges mapped to a mesh, and then obtaining the force on each particle from that field (Fotovat et al. 2017a). The explicit method resolves particle-particle interactions directly from charge and separation distance, whereas the implicit method provides a mesh-based (and therefore spatially filtered) representation of long-range interactions.

For Euler-Euler type models (Rokkam et al. 2010), only the implicit method is typically applied. Recent simulation studies indicate that Euler-Euler methods, when combined with Poisson's equation, are most suitable for simulating fluidized beds in larger system sizes. In contrast, Euler-Lagrange type simulations that use Coulomb's law to account for electrostatic particle interactions provide more detailed insights but come with a higher computational cost (Fotovat et al. 2017a).

Table 2.1 presents a summary of recent Euler-Lagrange studies that estimate electrostatic forces in gas-solid fluidized beds. Although the explicit Coulomb summation for all the particles accurately captures electrostatic forces affecting particle motion, it requires computing interactions for each particle pair, leading to a computational complexity of $\mathcal{O}(N^2)$ (despite being highly parallelizable). As a result, fully resolved Coulomb summation is generally limited to small beds or two-dimensional (2-D) domains due to computational limitations (Pei et al. 2016; Pei et al. 2013).

To reduce the computational cost associated with explicit pairwise Coulomb summation, many studies have adopted the screened-force methods (SFM), also referred to as truncated-pairwise approaches, in which only short-range electrostatic interactions are retained while contributions from more distant particles are neglected (Cheng et al. 2012; Hadisarabi et al. 2019; Hassani et al. 2013; Hogue et al. 2008; Kazemi et al. 2021; Korevaar et al. 2014; Norouzi et al. 2016; Tan et al. 2019; Wang et al. 2023; Yang et al. 2017). In these methods, electrostatic forces are computed only for particle pairs separated by less than a prescribed cut-off radius r_c. An early demonstration of this approach considered a two-dimensional system of 500 spherical particles (diameter 2 mm) flowing down an inclined chute, where interactions beyond five particle radii were ignored (Hogue et al. 2008).

The underlying assumption of the screened-force method is that long-range electrostatic interactions decay sufficiently rapidly due to dissipative mechanisms such as gas drag, charge leakage, or environmental conductivity

(Aghel et al. 2022). While this assumption may be reasonable in conductive or humid environments, it becomes questionable in dry, insulating systems, such as polymer powders and other high-resistivity materials, where charge dissipation is negligible and long-range Coulombic forces can remain significant (Hendrickson 2006). As demonstrated in several studies (Giordano et al. 2025; Kolehmainen et al. 2016), truncating electrostatic interactions in such conditions can lead to substantial errors in predicting particle clustering, electrostatic effects on hydrodynamics, and wall fouling.

Table 2.1: An overview of computational studies on electrostatic force calculation methods used in an Eulerian-Lagrangian model of gas-solid fluidized bed

Reference	Investigation	Bed size	Electrostatic force computational method
(Cheng et al. 2012)	Experiments and numerical simulations were used to study the electrostatic performance in the downer reactor of a triple-bed combination circulating fluidized bed	$D \times H = 0.04 \times 2.0$ m^3	Coulomb's law, screened force
(Hassani et al. 2013)	The effect of electrostatic forces between particles on fluidization hydrodynamics was studied	$W \times H \times D = 0.15 \times 1.0 \times 0.01$m^3	Coulomb's law, screened force
(Pei et al. 2016; Pei et al. 2013)	Contact electrification and electrostatic interactions between charged particles with different gas velocities in a 2-D fluidized bed were investigated during fluidization	$W \times H = 0.01 \times 0.02$ m^2	Coulomb's law
		$W \times H = 0.005 \times 0.035$ m^2	
(Norouzi et al. 2016)	Governing equations of inter-particle forces such as van der Waals, liquid bridge, and electrostatic forces, are discussed in the CFD-DEM modeling of the fluidized bed in the 8th chapter of this book		Coulomb's law, screened force
(Kolehmainen et al. 2016)	Development of a hybrid method for electrostatic force computation to consider long-range force using Gauss's law	$W \times H = 0.003 \times 0.096$ m^2	Coulomb's law for nearby particles and Gauss's law for long-range forces
(Hadisarabi et al. 2019)	Development of a computational model for charge build up in fluidized bed	$W \times H \times D = 0.15 \times 0.80 \times 0.01$ m^3	Coulomb's law, screened force
(Tan et al. 2019)	Analyses on the influence effect of electrostatics on single bubble rising in a 2D gas-solid fluidized bed	$W \times H = 0.024 \times 0.06$ m^2	Coulomb's law, screened force
(Li et al. 2022)	Hydrodynamics of a hybrid pulsed fluidized bed	$W \times H \times D = 0.04 \times 0.32 \times 0.004$ m^3	Coulomb's law, screened force

Because neither full Coulomb summation (accurate but expensive) nor screened-force truncation (efficient but potentially inaccurate when long-range effects matter) is fully satisfactory for large, industrially relevant domains, several *hybrid* approaches have been proposed to balance accuracy and computational cost. These methods share a common principle: treat the near field with particle-particle resolution, while approximating the far field with a coarser representation.

For instance, Kolehmainen et al. (2016) computed short-range interactions via a truncated Coulomb summation and accounted for long-range contributions by solving the Poisson equation on an Eulerian mesh to obtain an electric field acting on particles. A correction term was introduced to avoid counting the interactions represented in both parts twice. The strength of such Poisson-based methods is that they naturally represent long-range interactions; however, their cost and accuracy depend strongly on mesh resolution and on how charges are mapped from particles to the mesh, and sufficiently fine grids near strongly charged regions can become computationally demanding.

Alternatively, Grosshans et al. (2017) proposed a hybrid formulation in which neighbor interactions are evaluated with Coulomb's law, while far-field effects are approximated using Gauss' law, building on Aboud et al. (2004). Their results highlighted a practical limitation of standard Eulerian field solvers in large-scale particle simulations: maintaining accuracy may require fine grids around charged particles, which increases memory use and runtime.

A different class of hybrid methods avoids solving a global field equation by using particle-cell decompositions. Pei et al. (2015) introduced a hybrid particle-cell method that partitions the electrostatic domain around each particle into a strong-interaction (SI) region and a weak-interaction (WI) region. Forces from particles in the SI region are computed directly by Coulomb's law, while forces from the WI region are approximated from the net charge in each cell and the distance between the particle and the cell center. Such approaches can be computationally efficient, but their accuracy depends on how the chosen cut-off distance and cell size resolve local heterogeneity in the charge distribution.

Although these hybrid schemes can reduce the computational complexity to $\mathcal{O}(N \log N)$, they often remain sensitive to spatial discretization errors and to local charge gradients, particularly in strongly inhomogeneous systems where charge clustering is pronounced. Notably, more advanced mesh-free hierarchical solvers, such as the Barnes-Hut (BH) tree algorithm (Barnes et al. 1986b) and the Fast Multipole Method (FMM) (Dehnen 2014), have, to date, not been adopted in electrostatic CFD-DEM simulations of fluidized beds. This absence contrasts sharply with their widespread and mature use in other particle-based fields, including astrophysics, colloidal science, and molecular dynamics, where BH and FMM are standard tools for efficiently resolving long-range interactions (Gan et al. 2014; Hoffmann 2006; Kohnke et al. 2020; Ruan et al. 2022).

Several factors have contributed to the limited adoption of hierarchical methods in electrostatic fluidization modeling. First, electrostatic forces in fluidized beds have long been assumed to be effectively short-ranged under typical operating conditions, motivating the use of screened-force approximations. Second, the need to dynamically construct and update hierarchical data structures at each DEM time step has been viewed as prohibitively complex. Finally, until recently, the computational resources

available to DEM practitioners constrained the practical implementation of such algorithms. However, as demonstrated in this work, neglecting long-range electrostatic interactions can lead to physically inconsistent predictions, even at moderate charge levels representative of polymer-drying and other industrial fluidization processes.

Motivated by these limitations, the objective of this work is to propose and characterize a hybrid force calculation method, namely hierarchical particle-cell method, that efficiently captures both short-range and long-range electrostatic interactions while remaining practical for large fluidized-bed simulations. Inspired by the Barnes-Hut algorithm (Barnes et al. 1986b) used in astrophysical N-body simulations, the proposed method employs a hierarchical cell structure: short-range forces are computed directly within a smaller *minor cell* surrounding each particle, while long-range forces are approximated through an averaged representation over a larger *major cell*. Compared with screened-force truncation, the method retains a controlled approximation of far-field contributions; compared with purely mesh-based Poisson solvers, it reduces reliance on globally fine grid resolution around particles; and compared with single-level particle-cell aggregation (Pei et al. 2015), the hierarchy improves the representation of non-uniform charge distributions at increasing length scales. From an algorithmic perspective, the hierarchical particle-cell method represents a first step toward a full Barnes-Hut implementation, with the key distinction that Barnes-Hut employs adaptive hierarchical refinement, enabling superior performance for strongly inhomogeneous charge distributions.

The following sections provide a detailed explanation of the DEM modeling technique including the proposed hybrid method for electrostatic force calculations. Subsequently, we compare its performance with the screened-force technique and the exact evaluation method (all pairwise interactions), discuss grid-size optimization to balance accuracy and computational cost, and present two further modifications aimed at improving computational efficiency.

2.2 Discrete Particle Model framework

In this study, a gas-solid fluidized bed is modeled using an Euler–Lagrange approach implemented through the Discrete Particle Model (DPM). Newton's equations of motion are solved for each individual particle, while the gas phase is treated as a continuum and described on an Eulerian mesh. Additionally, other properties, such as particle charge, are tracked separately and considered constant and mono-polar in this study. Inter-phase momentum coupling is handled through a mapping term in the momentum balance, which corresponds to the drag force term in the particle equations of motion. As for this work, the focus lies on the methods for electrostatic force calculations, the generic modeling equations for fluid flow and particle motion are summarized

in Table 2.2. Further details on DPM can be found in the literature, e.g., (Deen et al. 2007; Hoomans et al. 1996; Mihajlovic et al. 2020; Mihajlović et al. 2025; Tan et al. 2014; Tan et al. 2017; Zhao et al. 2024). The remainder of this section considers the incorporation of the electrostatic forces.

Table 2.2: Summary of equations in the DPM model for the simulation of gas-solid fluidized beds

Eulerian Equations	
Continuity equation	$\frac{\partial(\varepsilon_g \rho_g)}{\partial t} + \nabla.(\varepsilon_g \rho_g \vec{u}_g) = 0$
Navier-Stokes equation	$\frac{\partial(\varepsilon_g \rho_g \vec{u}_g)}{\partial t} + \nabla.(\varepsilon_g \rho_g \vec{u}_g \vec{u}_g) = -\varepsilon_g \nabla p_g - \nabla.(\varepsilon_g \vec{\tau}_g) - S_p + \varepsilon_g \rho_g \vec{g}$
Lagrangian Equations	
Newton's Law of motion	$m_p \frac{d\vec{v}_p}{dt} = \sum \vec{F} = \vec{F}_{\text{external}} + \vec{F}_{\text{contact}}$
External force exerted on particles	$\vec{F}_{\text{external}} = m_p \vec{g} - V_p \nabla p_s + \frac{V_p \beta}{1-\epsilon_g}(u_g - v_p) + \vec{F}_{\text{electrostatic}}$
Contact forces, Soft sphere model	$\vec{F}_{\text{contact,i}} = \sum \vec{F}_{ij,n} + \vec{F}_{ij,t}$
	$\vec{F}_{ij,n} = -k_n \sigma_n \vec{n}_{ij} - \eta_n \vec{v}_{ij,n}$
	$\vec{F}_{ij,t} = \begin{cases} -k_t \eta_t & \text{if} \quad e_n \neq 0 \\ -\mu_f & \text{if} \quad e_n = 0 \end{cases}$
	$\eta_n = \begin{cases} \frac{-2 \ln e_n \sqrt{m_{ij} k_n}}{\sqrt{\pi^2 + \ln {e_n}^2}} & \text{if} \quad e_n \neq 0 \\ 2\sqrt{m_{ij} k_n} & \text{if} \quad e_n = 0 \end{cases}$
	$\eta_t = \begin{cases} \frac{-2 \ln e_t \sqrt{\frac{2}{7} m_{ij} k_t}}{\sqrt{\pi^2 + \ln {e_n}^2}} & \text{if} \quad e_t \neq 0 \\ 2\sqrt{\frac{2}{7} m_{ij} k_t} & \text{if} \quad e_t = 0 \end{cases}$
Coupling Equations	
Inter-phase momentum exchange	$S_p = \frac{1}{V_{cell}} \int \sum_{k=0}^{N_p} \frac{V_{p,k} \beta}{1-\varepsilon_g} (\vec{u} - \vec{u}_{p,k}) \delta(\vec{u} - \vec{u}_{p,k})$

Force Calculation

Besides gravity and drag, the primary force of interest in this study is the electrostatic force, which governs the attraction or repulsion between charged particles. To simplify its calculation, the following assumptions were made:

1. Each charged particle is represented as a point charge located at its center of mass.
2. Particle charge is prescribed and kept constant during each simulation to isolate the influence of electrostatic interactions.
3. The electrostatic force is computed using Coulomb's law (Equation 2.1).
4. Image-charge forces are neglected in the main simulations unless otherwise stated. Their influence is examined separately in Section 3.5.

In our initial approach, Coulomb's law (Equation 2.1) is used to calculate the electrostatic force between particles. Since this force acts between pairs

of charges, it affects both particles equally in magnitude but in opposite directions.

$$\vec{F}_{\text{electrostatic}} = \frac{q_i q_j}{4\pi\varepsilon_0} \frac{\vec{r_i} - \vec{r_j}}{|\vec{r_i} - \vec{r_j}|^3} \tag{2.1}$$

Here, $\vec{r_i}$ represents the position of particle i, and $\vec{r_i} - \vec{r_j}$ is the displacement vector between charges, with $|\vec{r_i} - \vec{r_j}|$ representing its magnitude. The vacuum permittivity, ε_0, is equal to $8.854 \times 10^{-12}\,\mathrm{C^2\,kg^{-1}\,m^{-3}\,s^2}$. The charges of the particles are indicated by q_i and q_j. The polarity and relative positions of these charges determine the force direction: opposite charges attract, causing the force to be directed toward each other, while like charges repel, resulting in a force directed away from one another (Figure 2.1).

Screened-Force Method

While Coulomb's law governs electrostatic interactions between all particles, computing every pairwise interaction becomes computationally prohibitive for large systems. A common strategy to mitigate this challenge is to consider only the most significant interactions, typically those between nearby particles. This approach has been widely adopted in previous studies (Cheng et al. 2012; Hogue et al. 2008; Salama et al. 2013). The screened-force technique, in particular, reduces computational complexity by neglecting interactions beyond a predefined cut-off distance, assuming their net contribution is negligible.

To efficiently identify particle pairs for electrostatic interaction calculations, two distinct radii are used: the electrostatic cut-off radius, r_c, and the Verlet-list search radius, r_s. The cut-off radius r_c defines the maximum separation at which the electrostatic interaction between a particle pair is explicitly evaluated. In contrast, r_s is a computational parameter used to construct the neighbor list and is chosen larger than r_c, such that particles that may enter the interaction range before the next neighbor-list update are already included as potential neighbors. Thus, r_s determines which particles are stored in the neighbor list, whereas r_c determines which particle pairs actually contribute to the electrostatic force calculation, as illustrated in Figure 2.2.

A neighbor list is typically implemented using a Verlet list (Verlet 1967), which stores, for each particle, a list of its potential neighbors. The Verlet neighbor list goes beyond a simple distance check by incorporating information from previous time steps, allowing for more efficient computational updates and reducing the frequency of neighbor-list recalculations. As illustrated in Figure 2.2 (described in 2-D for convenience), particles within the search radius r_s are retained as potential neighbors and verified during the update step, reducing redundant neighbor searches.

Since particles move during the simulation, the Verlet list is updated dynamically. Particles that exit the search radius r_s are removed, while newly approaching particles are added. For the electrostatic force calculation,

only particle pairs with a separation smaller than the cut-off radius r_c are considered. This adaptive mechanism ensures that relevant interacting pairs are captured while significantly reducing the computational cost compared with a static neighbor list.

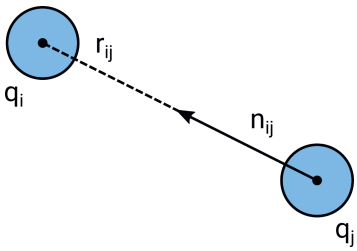


Figure 2.1: Geometrical parameters of two charged particles

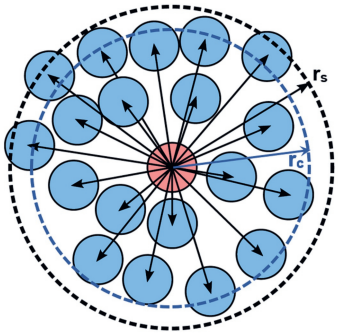


Figure 2.2: Schematic of the Verlet list method

For simulations utilizing the screened-force technique in this study, a cut-off radius was selected to ensure that any electrostatic force exceeding 5% of a particle's gravitational force is accounted for (Hassani et al. 2013). To determine the effective separation distance for a given particle, the cut-off radius r_c was defined as the distance at which a similar particle, having the same size and charge, exerts an electrostatic force equal to 5% of its gravitational force. Given Coulomb's law and the gravitational force acting on each particle, r_c can be calculated using the following formula:

$$r_c = K_c \; q \; r_p^{-3/2} \quad , \quad K_c = \frac{1}{\sqrt{\left(\frac{16}{3}\right) \pi^2 \rho_p g \alpha \varepsilon_0}} \tag{2.2}$$

In this equation, ρ_p represents the particle density, r_p is the particle radius, and q is equal to the particle charge. The parameter α is the ratio of the electrostatic force to the particle's weight, below which the electrostatic force is considered negligible. In this study, α is set to 0.05.

Hybrid Method

In this section, we propose a hybrid approach that incorporates both long-range and short-range electrostatic forces to achieve a more accurate calculation of electrostatic forces in fluidized beds while maintaining the computational efficiency. The core idea of the hybrid method is to approximate long-range electrostatic forces by averaging interactions over spatially grouped particles rather than computing them individually,

inspired by the approach of (Barnes et al. 1986a). This method balances computational efficiency with accuracy. The domain is subdivided using a regular Cartesian mesh Γ, where each volumetric cell $d\Gamma$ contains a group of particles. It is important to note that the grid $d\Gamma$ used for electrostatic force aggregation is independent of the Eulerian mesh employed for solving the fluid flow equations in the CFD part of the CFD-DEM framework. The electrostatic grid is introduced only for grouping particle charges and may therefore be chosen with different resolution or alignment than the fluid grid. In practice, both grids could be set identical for convenience, but this is not required by the method. Each particle is assigned to the cell in which it resides. This is an $\mathcal{O}(n)$ operation that can be efficiently integrated with the neighbor list search algorithm when the cell sizes are appropriately chosen, further enhancing computational performance.

Similar to the screened-force method, we establish a distance threshold for each particle pair to determine whether an explicit Coulomb-type interaction is computed or if the long-range electrostatic force calculation is applied instead. The long-range force is computed as a weighted average of the charges within a given cell $d\Gamma$, effectively representing all charges in that cell as a single equivalent charge. This significantly reduces the number of computations by lumping multiple particle interactions into a single calculation.

Figure 2.4 provides a schematic representation of this approach. Unlike the screened-force method, which employs a spherical cut-off radius (illustrated in 2-D in Figure 2.3), the hybrid method uses a cubic region to simplify computation. As shown in Figure 2.4, explicit pairwise Coulomb interactions are computed for all particles (blue) within the red square. Beyond this region, instead of considering every individual particle, a weighted average position of aggregated particles (green) in each cell is used.

For each cell $d\Gamma_k$, the total charge Q_k is given by:

$$Q_k = \sum_{j \in d\Gamma_k} q_j, \tag{2.3}$$

where $d\Gamma_k$ represents the k-th cell containing the aggregated charge Q_k, which is located at the cell's weighted centroid R_k. The weighted centroid R_k is determined by:

$$\mathbf{R}_k = \frac{\sum_{j \in d\Gamma_k} q_j r_j}{\sum_{j \in d\Gamma_k} q_j}. \tag{2.4}$$

The lumped charge Q_k located at $\mathbf{R}_k$ is then treated as an equivalent point charge when evaluating the long-range electrostatic force on a target particle i. The contribution of cell k to the electrostatic force on particle i is calculated as

$$\mathbf{F}^e_{i,k} = \frac{1}{4\pi\varepsilon_0} \frac{q_i Q_k}{|\mathbf{R}_k - \mathbf{r}_i|^3} (\mathbf{R}_k - \mathbf{r}_i), \tag{2.5}$$

where q_i and $\mathbf{r}_i$ are the charge and position of the target particle, respectively. The total electrostatic force on particle i is obtained by combining the directly evaluated particle–particle interactions in the region surrounding the target particle with the contributions from the lumped charges outside this region. This total electrostatic force enters the particle equation of motion as $\mathbf{F}_{\text{electrostatic}}$.

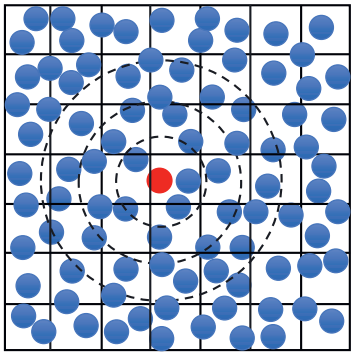


Figure 2.3: Screened-force method

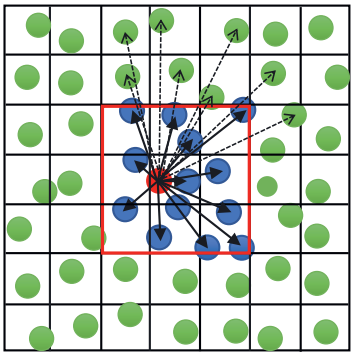


Figure 2.4: Hybrid method

Hybrid Method Improvements

As discussed in previous sections, accurately computing electrostatic forces in gas-solid fluidized beds requires capturing both short- and long-range interactions while ensuring computational efficiency. In Section 2.3, we will demonstrate that the hybrid method significantly reduces computational costs. However, it remains computationally demanding for large-scale systems. To address this, we propose two modified hybrid methods designed to further enhance computational efficiency, as schematically illustrated in Figure 2.5.

The first method, the single-grid hybrid approach, uses a uniform grid size $d\Gamma$ to generalize the calculation of long-range electrostatic forces. In this approach, long-range interaction forces are computed based on the charge center of the grid cell containing the target particle. A fixed location for the charge center, where the target particle is located, is considered during distance calculations (even for short-range forces before switching to lumped particles). This approach reduces computational time but may potentially lower accuracy. The transition from direct force calculations to lumped approximations occurs at the boundary of $d\Gamma$ (as shown in Figure 2.5), where particles beyond this boundary treated as lumped entities.

The second method, the multi-grid hybrid approach (or the hierarchical particle-cell method), employs a hierarchical grid structure, where fine grids

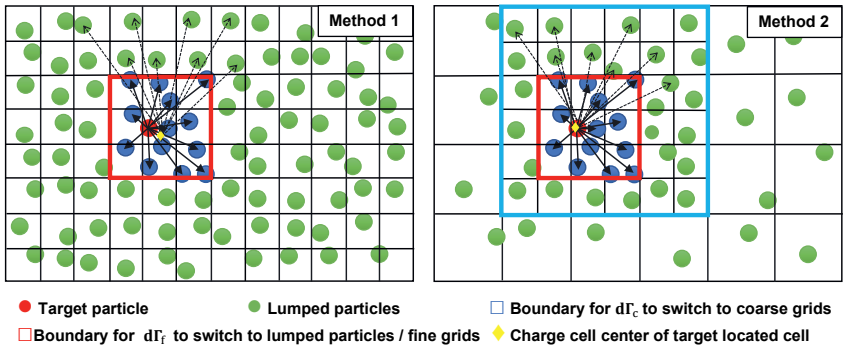


Figure 2.5: Two different modified hybrid computation methods to reduce computational cost. Method 1: Considering the charge cell centers of the target cell location to calculate the distance to the lumped particles. Method 2: Multi-grid sizes for the lumped particles, with coarser grids used for particles farther from the target.

Γ_f are used for detailed force computations near the target particle, and coarser grids Γ_c are applied for particles located at greater distances. The transition from fine to coarse grids is defined by a distance threshold. A schematic representation of this method is shown in Figure 2.5.

In this method, the computational algorithm begins by applying coarse-grid force approximations for particles located in the outer regions of the domain. As the algorithm progresses toward the target particle, finer grids Γ_f are employed, ensuring that interactions within the critical vicinity of the target particle are calculated with higher precision. Unlike the single-grid hybrid approach, this method uses the charge center of the target particle for electrostatic calculations. This multi-resolution framework effectively strikes a balance between accuracy in short-range force calculations and efficiency in handling long-range interactions.

Simulation Setup

In this study, 70,000 particles are considered for the 3-D simulation of a fluidized bed within a computational domain measuring $3.5 \times 3.5 \times 20$ cm^3. This domain size allows for a comprehensive representation of particle interactions within the fluidized bed environment. The particles are initially fluidized by a gas flow through the bottom boundary for 3 s in order to generate a representative particle distribution. Subsequently, the gas flow is switched off and the particles are allowed to collapse under gravity.

The electrostatic force calculation methods are benchmarked during this collapse stage, which represents a demanding test case for electrostatic

force evaluation due to the increased particle concentration and the large number of particle–particle interactions. Since exact electrostatic force evaluation scales with $O(N^2)$, performing such calculations throughout a complete fluidization simulation would be computationally prohibitive. Benchmarking the approximation methods against the exact solution during the collapse stage therefore provides a practical means of assessing their accuracy. Demonstrating good agreement with the exact solution under these conditions provides confidence in the applicability of the approximation methods to fluidized-bed simulations. The simulation details are provided in Table 2.3.

For the hybrid method, two different grid sizes are defined: small grids, equivalent to 5 times the particle radius, and large grids, equivalent to 20 times the particle radius. This approach enables the simulations to balance computational efficiency with the accuracy required to model both short-range and long-range electrostatic forces within the fluidized bed. Both the screened-force and hybrid simulations are compared with the *Exact Electrostatic Force Evaluation* method. The exact evaluation approach explicitly computes the Coulomb forces for all possible charge pairs in the system, following a brute-force methodology. While it provides high accuracy, this approach is computationally prohibitive and impractical for large-scale simulations due to its $O(N^2)$ scaling with respect to the number of charges, N. It was implemented here solely for benchmarking and validation purposes.

To address the computational challenges and facilitate these simulations, parallelization techniques were employed. Each particle's force calculation was made independent of the others, allowing for concurrent computations across multiple processing units. This parallel structure significantly improved efficiency by leveraging modern computational resources, making brute-force methods feasible for small-scale or specialized applications. However, the scalability limitations of this approach reaffirm its impracticality for routine use in large systems, highlighting the necessity of approximate methods like the screened-force and hybrid methods for practical simulations.

2.3 Results and Discussion

In this section, we first present the results of the screened-force method and compare them with the exact evaluation method. Next, we discuss the performance of the hybrid method relative to the exact evaluation. A detailed comparison of particle dynamics follows, focusing on the electrostatic force distribution and granular temperature predicted by each method. Finally, we explore the results of the two modified hybrid approaches aimed at further improving the computational efficiency.

Table 2.3: Simulation parameters

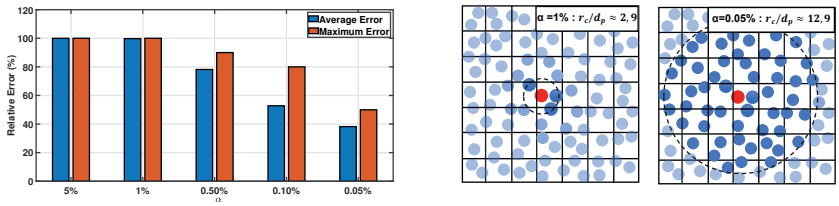
Parameters	Value
Number of particles [-]	70,000
Particle diameter [m]	1.0×10^{-3}
Particle density [$\mathrm{kg\,m^{-3}}$]	890
Particle restitution coefficient	0.9
Particle charge [pC]	6.5
Charge-to-mass ratio [$\mathrm{nC\,g^{-1}}$]	13.9
Simulation [-]	3D
Simulation Boundaries [-]	Bottom and all sides
Bed height [m]	0.20
Bed Width [m]	3.50×10^{-2}
Bed depth [m]	3.50×10^{-2}
Time step size [s]	1.0×10^{-6}
Grid size [m]	2.50×10^{-3}
Number of Eulerian cells [-]	15,680
Superficial gas velocity [-]	$U/U_{mf} = 2.0$

Screened-Force Method Simulation Results

This section compares the results of two simulation methods, the screened-force method and the exact electrostatic force evaluation. Simulations were performed on a fluidized bed of charged particles under the conditions outlined in Table 2.3. After three seconds of fluidization, electrostatic forces were calculated using both methods. To quantitatively evaluate the computational error of the screened-force method, the electrostatic force acting on each particle was computed and compared against the exact electrostatic force evaluation. The resulting difference defines the error. The average relative error across all particles, as well as the maximum relative error, was then determined and is presented in Figure 2.6a. For the screened-force method, different values of the screening criterion α were investigated. The corresponding errors are shown in Figure 2.6a, while Figure 2.6b illustrates the influence of α on the cut-off radius and the number of particles included in the electrostatic force calculation. The results highlight significant discrepancies, with the screened-force method exhibiting notably high average computational errors.

The analysis reveals that even when using screened forces with various cut-off distances, corresponding to electrostatic-to-gravitational force ratios ranging from 5% to as low as 0.05%, the computational errors remain significant. These results indicate that long-range electrostatic forces are significantly influencing the system and adjusting the hydrodynamics. This confirms that applying a cut-off distance for force computation fails to yield accurate results, even when the cut-off parameter α is set as low as 0.05%. For this case, the maximum error in the system exceeds 50%, while the average electrostatic force computational error across the entire bed remains above 38%. As illustrated in Figure 2.6b, reducing α increases the cut-off radius r_c and consequently increases the number of particles included in

the electrostatic force calculation. Although the errors decrease as larger portions of the bed are considered, substantial discrepancies remain even for the smallest value of α investigated.



(a) Relative error.

(b) Influence of the screening criterion.

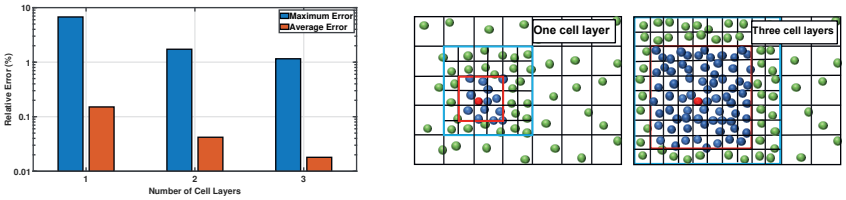
Figure 2.6: (a) Average and maximum relative errors obtained using the screened-force method for different values of the screening criterion α. (b) Illustration of the screened-force method for $\alpha = 1\%$ and $\alpha = 0.05\%$. A decrease in α increases the cut-off radius and the number of particles included in the electrostatic force calculation.

Extending the cut-off distance to encompass an even larger range, or the entire bed, would lead to an unreasonably high computational cost, making it impractical for large-scale simulations. However, to achieve accurate results, both short-range and long-range electrostatic forces must be considered.

Hybrid Method Simulation Results

In this section, we discuss the results of the proposed hybrid method, which aims to minimize electrostatic force computational errors while maintaining the computational efficiency of the screened-force approach. This method considers the long-range electrostatic forces as well by averaging interactions over spatially grouped particles. To balance computational cost and accuracy, the transition threshold to long-range calculations was evaluated by varying the number of cell layers around each particle, from one to three layers. The average and maximum relative errors in electrostatic force calculations were assessed for these configurations. Figure 2.7a presents the error as a function of the number of surrounding cell layers used for direct Coulomb calculations. Figure 2.7b schematically illustrates the directly resolved region $\Gamma_{f,\text{direct}}$ for one and three surrounding cell layers.

The results demonstrate that increasing the number of surrounding cell layers included in $\Gamma_{f,\text{direct}}$ improves the accuracy of the electrostatic force calculation. As shown in Figure 2.7b, enlarging the directly resolved region increases the number of particle-particle Coulomb interactions that are evaluated explicitly while reducing the portion of the domain represented by lumped charges.



(a) Relative error. (b) Interaction regions.

Figure 2.7: (a) Average and maximum relative errors obtained using the hierarchical particle-cell method for different numbers of surrounding cell layers. (b) Schematic representation of the hierarchical particle-cell method. Electrostatic interactions within $\Gamma_{f,\text{direct}}$ are evaluated using direct Coulomb calculations, whereas interactions outside this region are approximated using lumped charges in $\Gamma_{f,\text{lumped}}$ and Γ_c.

For two and three surrounding cell layers, the average relative error remains below 0.1%, while the maximum error is reduced to below 2%. Even for a single surrounding cell layer, the average error remains small, although the maximum error increases to approximately 7%. This demonstrates that accurate electrostatic force prediction can be obtained using only a limited directly resolved region around each particle.

Despite these limitations, the hybrid method significantly reduces computational costs by approximately a factor of 8. For instance, simulating a particle bed with 70,000 particles for 1 ms using the exact evaluation method, which accounts for all pairwise interactions, requires approximately 1891 min of CPU time. In contrast, the same simulation using the hybrid method takes only 239 min. While the hybrid method offers a promising balance between accuracy and efficiency, it remains computationally demanding for large-scale systems, indicating room for further optimization. The following section will explore the results of the two alternative approaches designed to enhance the computational efficiency of the hybrid method while maintaining acceptable error thresholds.

Electrostatic Force Distribution Comparison

To further evaluate the accuracy of the screened-force and hybrid methods in simulating particle dynamics, their predictions of electrostatic force and particle position distribution are compared to the exact evaluation method predictions. This exact evaluation serves as a benchmark for measuring the relative performance of the other methods. For computational feasibility, a smaller bed of 10,000 particles was employed, given the high computational cost of the exact evaluation method. Figure 2.8 presents snapshots of the particle bed after three seconds of simulation, just before the collapse

phase. The figure illustrates particle positions along with a color gradient representing the magnitudes of the electrostatic forces.

Observations from the figure are as follows:

- Screened-Force Method:
  - The total electrostatic force magnitudes calculated using the screened-force method deviate significantly from the exact evaluation.
  - The force underestimation results in particles failing to fully spread throughout the bed, leading to a compact and confined structure.
  - This lack of fidelity highlights the limitations of the screened-force approach in accurately capturing long-range electrostatic interactions, leading to deviations in particle distribution and overall fluidization behavior.
- Hybrid Method:
  - The hybrid method closely aligns with the exact evaluation in both particle positions and force magnitudes.
  - Particles are well-distributed across the domain, with a clear tendency to be drawn toward the walls.
  - This behavior suggests that wall-adjacent particles experience electrostatic forces directing them toward the boundaries, even though image charge effects are not considered in the simulation.
- Exact Evaluation Method:
  - This method provides the ground-truth representation of the system's dynamics.
  - It considers all pairwise interactions without approximations, serving as a benchmark for evaluating other methods.
  - Particles near the walls migrate toward them, confirming the directional nature of electrostatic forces and their influence on wall-adjacent particles.

The observed tendency of particles to adhere to the walls in both the hybrid and exact methods may be attributed to the relatively small size of the particle bed in the simulations. In smaller systems, a larger proportion of particles experience wall-adjacent forces, potentially amplifying the wall effect. However, this phenomenon has not been fully verified, and further investigation is required to determine whether the effect diminishes in larger systems, where wall influences might be distributed over a greater volume. A more rigorous analysis, including simulations of larger domains and experimental validation, is necessary to confirm this hypothesis.

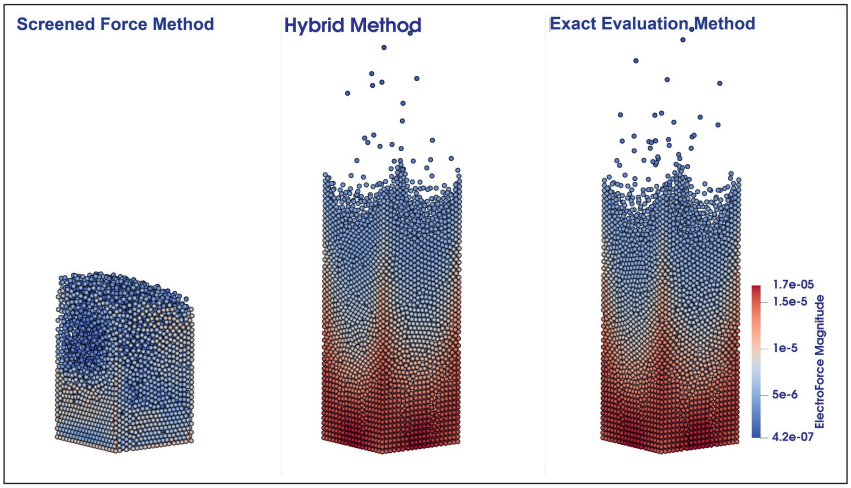


Figure 2.8: Snapshots of the three different methods described in this study. In the hybrid method, particles experience stronger electrostatic forces compared to the screened-force method, causing them to spread more throughout the bed. Additionally, particles in the hybrid method, like those in the exact method, are observed to adhere to the walls. This behavior is similar to the results obtained using the exact evaluation method, which provides a more accurate representation of the system's dynamics.

Granular Temperature Distribution Comparison

To enable a more detailed comparison of particle dynamics across the three methods, a granular temperature analysis is conducted. Granular temperature serves as a key parameter in characterizing the kinetic behavior of particulate systems, quantifying the intensity of particle velocity fluctuations. According to the Kinetic Theory of Granular Flow (KTGF), granular temperature represents the random velocity deviations of particles over small spatial regions and short time intervals. It is mathematically expressed as (Wang et al. 2010):

$$\Theta = \frac{1}{3}(\Theta_x + \Theta_y + \Theta_z) \tag{2.6}$$

where, x, y, and z represent the spatial direction. The granular temperature in the k-th direction (Θ_k) is defined as follows:

$$\Theta_k = \frac{\sum_{i=1}^{N_{part}} (v_{k,i} - v_k)^2}{N_{part}} \tag{2.7}$$

and v_k is the average velocity, which can be determined using the following expression:

$$v_k = \frac{\sum_{i=1}^{N_{part}} v_{k,i}}{N_{part}} \tag{2.8}$$

Figures 2.9 and 2.10 illustrate the granular temperature distribution for the three computational approaches: the screened-force method, the hybrid method, and the exact evaluation method. As shown in Figure 2.9, the granular temperature distribution obtained using the hybrid method closely matches that of the exact evaluation method. In contrast, the screened-force approach significantly overestimates the granular temperature, particularly in the lower and central regions of the bed. This discrepancy indicates that the screened-force method overestimates particle velocity fluctuations, leading to inaccurate predictions of particle interactions and bed stability.

Both Figures 2.9 and 2.10 reveal a consistent trend: particle movement is most restricted in the middle of the bed, while the upper region exhibits greater particle mobility. However, the screened-force method fails to accurately capture this behavior, as it unrealistically predicts elevated granular temperatures even in regions where particle motion should be minimal. This overestimation further underscores the screened-force method's limitations in resolving the intricate dynamics of electrostatic interactions within the particle bed.

Figure 2.10 offers a more detailed quantitative comparison of granular temperature variations along the bed's axial direction. The exact and hybrid methods yield similar profiles, indicating that significant particle motion occurs primarily in the upper regions of the bed. This behavior arises due to reduced confinement in these areas, allowing particles to move more freely under the influence of electrostatic and fluid forces. In contrast, the screened-force method overestimates granular temperature by predicting substantial particle motion throughout the bed, failing to capture the expected reduction in velocity fluctuations in confined regions. Notably, particle motion in the hybrid and exact methods is reduced by approximately 60% compared to the screened-force approach. This significant reduction highlights the hybrid method's enhanced accuracy in capturing the underlying physical interactions, ensuring a more realistic representation of particle dynamics within the bed.

To gain deeper insight into particle dynamics, the average particle velocities were analyzed over time, and the resulting circulation patterns are illustrated in Figure 2.11. The visualization is performed on a central longitudinal slice of the bed to reduce direct front–back wall effects. Nevertheless, owing to the relatively small bed dimensions considered in this study, even the central region remains within the electrostatic influence range of the container boundaries. As a result, wall effects are not fully eliminated and continue to influence particle motion throughout the bed. In the hybrid method, particles exhibit reduced mobility in the bulk and a tendency to accumulate near the walls. This behavior arises from the retention of long-range electrostatic interactions, which induce net forces directing particles toward the boundaries. In contrast, the screened-force approach predicts a more erratic and spatially uniform velocity field, indicating weaker electrostatic confinement. While such motion may appear qualitatively more similar to experimental observations without particle charges, earlier force

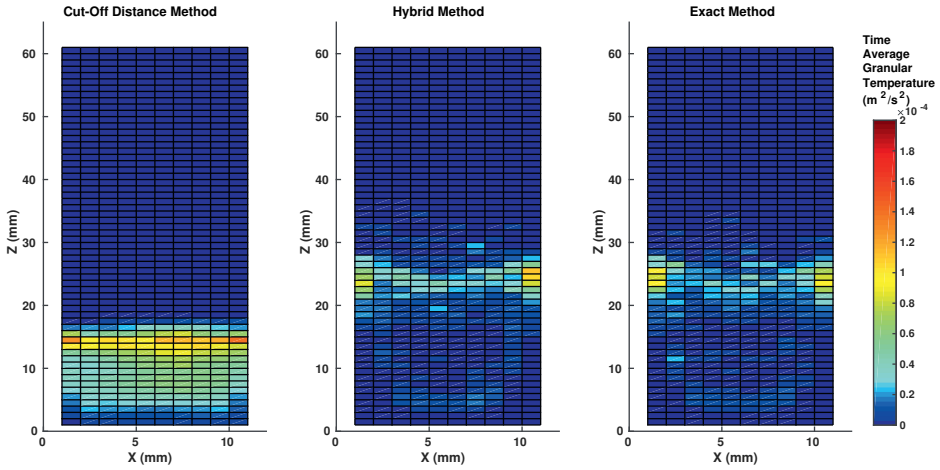


Figure 2.9: Time-averaged granular temperature.

and granular temperature analyses demonstrate that this behavior originates from an underestimation of long-range electrostatic interactions rather than improved physical accuracy.

The granular temperature distribution and circulation patterns indicate that the hybrid method provides a more accurate representation of the coupling between electrostatic forces and particle dynamics than the screened-force method. In addition to the axial profiles, the variability of the granular temperature field is examined using the cumulative distribution function (CDF), which quantifies the fraction of computational cells with granular temperature below a given value. This distributional analysis reveals that the hybrid approach closely reproduces the cumulative distribution obtained with the exact method, whereas the screened-force approach yields a larger fraction of elevated granular temperature values. This demonstrates that the improved agreement of the hybrid method is not limited to averaged quantities but also extends to the variability of the granular temperature field.

It should be noted that these observations may be influenced by the specific simulation conditions considered in this study. In particular, the relatively small bed size may enhance wall effects, as particles located near boundaries experience stronger electrostatic interactions. In larger systems, such effects are expected to be less pronounced due to the increased separation between the bulk particle population and the walls.

Overall, the results confirm the hybrid approach as a promising compromise between accuracy and computational efficiency. The method achieves close agreement with the exact evaluation while significantly reducing computational cost. Future work should focus on assessing the influence of bed size and wall effects more systematically, as well as exploring

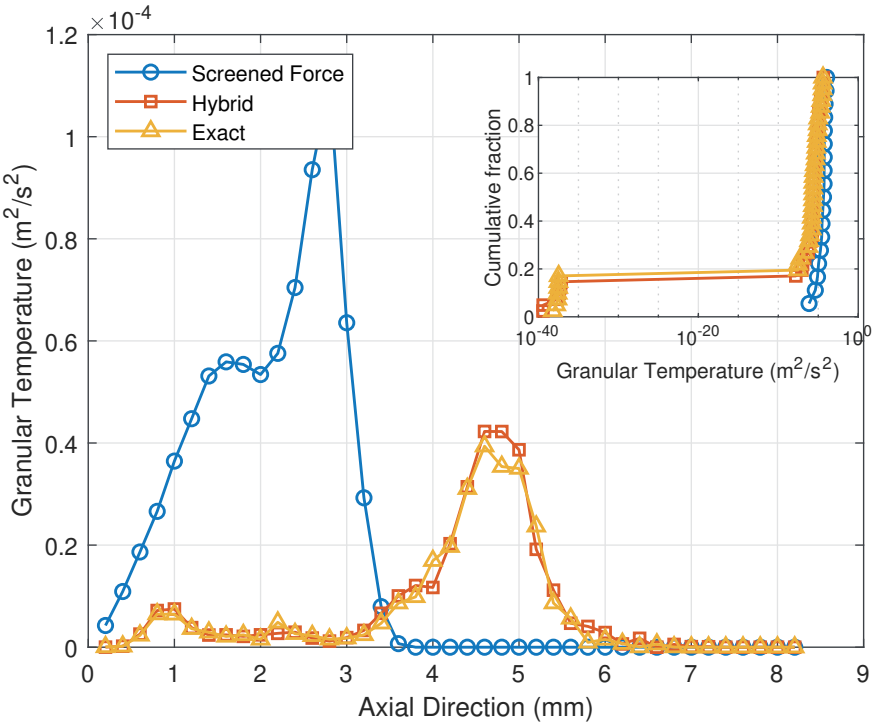


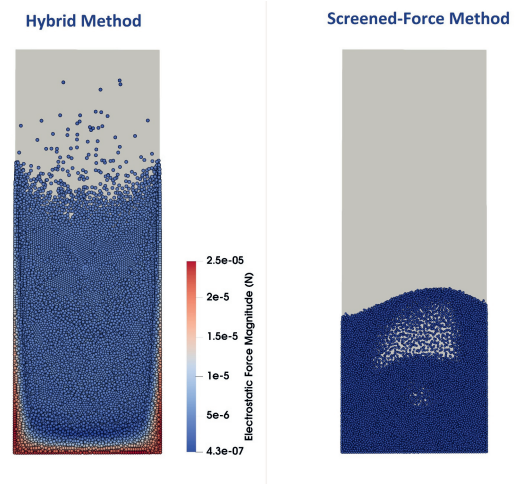
Figure 2.10: Axial distribution of time-averaged granular temperature along the axial direction for the screened force, hybrid, and exact interaction methods. The inset shows the cumulative distribution function (CDF) of granular temperature over all available computational cells at the same time instant. The CDF represents the fraction of cells with granular temperature below a given value.

the incorporation of image charge effects to further improve accuracy in the vicinity of boundaries.

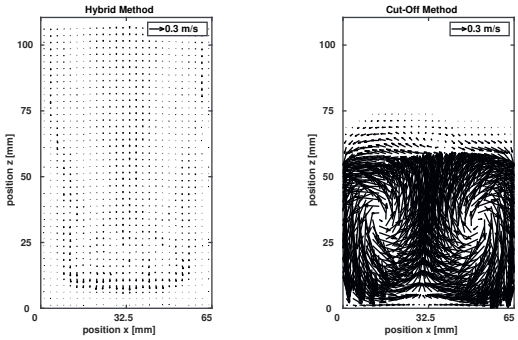
Hybrid Method Improvements Results

In this section, we will discuss the results of the two proposed modified hybrid methods designed to further enhance computational efficiency. The electrostatic force calculations associated with the two proposed modified hybrid methods are quantitatively analyzed, with the results summarized in Table 2.4. Key observations include:

- Single-Grid Hybrid Method (Method 1): This approach introduces significant computational errors due to the approximation of the target



(a) Electrostatic force magnitude



(b) Velocity vectors

Figure 2.11: Circulation pattern

particle's position by the charge center of the grid cell. The substitution error becomes more pronounced as the grid size increases.

- Multi-Grid Hybrid Method (Method 2): By employing fine grids Γ_f for precise force computation near the target particle and coarser grids Γ_c for distant particles, this method significantly reduces both average and maximum errors. The hierarchical grid structure introduces a substantial reduction in computational cost compared to the hybrid method while delivering similar accuracy.

The single-grid hybrid method introduces significant substitution errors due to the inherent inaccuracy of representing the target particle's position with the grid cell's charge center. As a result, the method has limitations in precision, particularly in systems where accurate force localization is crucial.

The multi-grid hybrid methodology provides a robust framework for electrostatic force computation, effectively balancing computational cost and precision. By leveraging a hierarchical grid structure, it achieves high accuracy in critical regions while efficiently approximating interactions from distant particles. Future work will focus on optimizing the grid transition threshold and assessing the method's scalability for larger and more complex systems.

Table 2.4: Percentage error and CPU time for different electrostatic force computation methods for a gas-solid fluidized bed with 70,000 charged particles.

	Average Percentage Error	Maximum Percentage Error	CPU time
Exact Solution	-	-	1891m 0.029s
Hybrid Method without modification	0.151	6.75	239m 1.335s
Single-Grid Hybrid Method	3.11	48.54	57m 11.721s
Multi-Grid Hybrid Method	0.17	6.76	43m 34.443s

2.4 Conclusion

This study highlights the critical role of accurately accounting for electrostatic interactions in predicting particle dynamics within fluidized beds containing charged particles. The findings demonstrate that relying solely on short-range electrostatic force calculations, as in the screened-force method, is insufficient for capturing the complex behavior of charged particles. While the exact evaluation of all pairwise interactions ensures the highest accuracy, its substantial computational cost makes it impractical for large-scale simulations.

To address these challenges, a hybrid approach, namely the hierarchical particle-cell method, was developed that combines the efficiency of the screened-force method with the precision of long-range electrostatic force calculations. By employing lumped particles at the charge center of computational cells and implementing a dual-grid system for long-range force computations, the hybrid method achieves a balance between computational efficiency and accuracy. This innovative methodology allows for more realistic modeling of charged particle behavior while significantly reducing the computational burden, making it more feasible for large-scale simulations.

The comparative analysis of particle movement, granular temperature distribution, and axial profiles revealed that the hybrid method closely aligns with the results of the exact method, outperforming the screened-force approach. The hybrid method reduced errors in electrostatic force calculations from 100% in the screened force method to under 7%, demonstrating its improved reliability. Furthermore, it accurately captured

critical particle behaviors, such as dispersion and wall interactions, which were either exaggerated or misrepresented by the screened-force method.

It is important to note that the limitations observed in this study, particularly regarding the influence of wall effects, stem from the use of a smaller bed size, which facilitated direct comparisons with the exact method. These limitations are not inherent to the hybrid method itself but rather reflect the constraints of using a smaller system for validation. In larger systems, the wall effects observed here may be less pronounced.

While this study provides valuable insights into the use of the hybrid method for fluidized bed simulations, several areas warrant further investigation to enhance both the understanding and application of this method:

- **Scaling Up to Larger Systems:** Future studies should assess the computational scalability of the hybrid method in progressively larger systems. Although the present method substantially reduces the computational cost relative to direct pairwise Coulomb evaluation, further improvements in computational efficiency could enable the application of discrete particle simulations to larger laboratory-scale systems. For industrial-scale systems, where discrete particle modeling remains impractical, more coarse-grained approaches such as two-fluid models (TFM) or phenomenological models incorporating electrostatic effects would be more appropriate. Studies at larger laboratory scales could also help determine whether wall effects diminish with increasing system size and assess the scalability of the proposed method.

- **Optimization of Grid Structures:** Future work could focus on further optimizing the dual-grid structure, including implementing adaptive grid refinement based on particle density or force magnitude. This would improve the efficiency and accuracy of the hybrid method, especially in systems with non-uniform particle distributions.

- **Implementation of fully adaptive hierarchical solvers:** A natural next step is the implementation of a fully adaptive Barnes-Hut algorithm, which would eliminate errors associated with fixed grid sizes by dynamically refining the spatial hierarchy based on particle distribution. Such an approach would further improve the accuracy of long-range electrostatic force calculations, particularly in strongly inhomogeneous systems, while maintaining favorable computational scaling.

- **Experimental Validation:** Although this study focused on computational comparisons, future research should prioritize experimental validation of the hybrid method. This would help confirm its reliability and accuracy in replicating real-world conditions and further improve its applicability to practical systems.

- **Investigation of Different Charge Distributions:** This study assumed uniform particle charge distributions. Future research should explore non-uniform charge distributions or dynamic charge evolution during particle interactions, which could offer deeper insights into the complexities of electrostatic effects in more realistic scenarios.

In conclusion, the hybrid method offers a robust and efficient framework for simulating the hydrodynamics of fluidized beds under the influence of electrostatic forces. By addressing its current limitations and exploring the suggested areas for future research, this methodology can be further refined and expanded for wider applications in both industrial and academic settings.

CHAPTER 3

Numerical investigation of the hydrodynamics of fluidized bed charged particles

Abstract

Hydrodynamic characteristics such as minimum fluidization velocity, bed expansion, bubble dynamics, solids circulation, and granular temperature determine the overall performance of gas–solid fluidized beds. In systems containing electrically insulating particles, these characteristics can be strongly affected by electrostatic charge accumulation generated through repeated particle–particle and particle–wall contacts. This chapter numerically investigates the influence of electrostatic interactions on the hydrodynamics of a gas–solid fluidized bed containing Geldart B particles using the Discrete Particle Model (DPM) framework developed in Chapter 2.

The simulations show that electrostatic charging modifies the onset of fluidization and increases bed heterogeneity. Charged beds exhibit larger local porosity variations and a more diffuse transition from the fixed-bed to the fluidized state, making the determination of a unique minimum fluidization velocity less straightforward than in uncharged systems. The increased emulsion-phase porosity allows a larger fraction of the gas to percolate through the particulate phase, reducing the amount of excess gas available for bubble growth.

Single-bubble injection simulations demonstrate that electrostatic interactions modify bubble evolution. Increasing particle charge promotes particle penetration into the bubble interior, producing a more diffuse gas-solid interface. Consequently, the measured bubble area (defined using a solids-holdup threshold) decreases and, at sufficiently high charge levels, the bubble may collapse before reaching the bed surface. These observations provide a mechanistic explanation for the experimentally reported reduction in bubble size in charged fluidized beds.

Electrostatic charging also alters particle dynamics by reducing particle mobility, weakening large-scale circulation patterns, and decreasing granular temperature. Overall, the results demonstrate that electrostatic interactions modify fluidized-bed hydrodynamics through coupled effects on local bed structure, gas distribution, bubble stability, and particle motion. This chapter therefore provides a mechanistic link between particle-scale electrostatic forces and macroscopic changes in bubbling fluidization behaviour.

3.1 Introduction

Gas–solid fluidized beds are widely employed in industrial processes such as fluid catalytic cracking, polymerization, combustion, drying, and coating due to their excellent gas–solid contact, efficient mixing, and high rates of heat and mass transfer (Cocco et al. 2014; Jakobsen 2014). The hydrodynamic behaviour of fluidized beds is commonly characterized by parameters such as the minimum fluidization velocity (U_{mf}), minimum bubbling velocity, bed expansion, bubble size, bubble rise velocity, and solids circulation patterns. These hydrodynamic characteristics strongly influence reactor performance, particle mixing, heat transfer, and product quality (Kunii et al. 1994; Yates et al. 2016).

Fluidization occurs when the drag force exerted by the gas balances the effective weight of the particles, causing the packed bed to transition into a fluidized state (Delebarre 2004; Ergun 1952). For Geldart B particles, bubbling generally commences shortly after minimum fluidization is reached (Geldart 1973; Shaul et al. 2014). The subsequent hydrodynamics are largely governed by bubble formation, bubble growth, bubble coalescence, and bubble-induced solids circulation (Kunii et al. 1991; Kunii et al. 1994).

Bubble size and bubble rise velocity are among the most important quantities governing hydrodynamics in bubbling fluidized beds because they directly influence gas–solid contact, solids circulation, and mass-transfer rates. Classical fluidization theories and correlations, such as those proposed by Mori and Wen (Mori et al. 1975) and summarized by Kunii and Levenspiel (Kunii et al. 1991; Kunii et al. 1994), provide a useful framework for describing

bubble growth, gas distribution, and bubble evolution in conventional fluidized beds.

In industrial fluidized beds containing insulating materials, however, particle charging is unavoidable due to repeated particle–particle and particle–wall collisions. The resulting triboelectric charge accumulation generates attractive and repulsive electrostatic forces that can become comparable to the hydrodynamic and gravitational forces acting on the particles (Fotovat et al. 2017a; Lacks et al. 2011; Matsusaka et al. 2010). Electrostatic phenomena have long been recognized as a major operational challenge in fluidized-bed reactors due to their association with wall sheeting, particle agglomeration, fouling, entrainment, and process instability (Hendrickson 2006; Salama et al. 2013; Zhang et al. 2021).

Beyond these operational issues, electrostatic forces can directly affect fluidized-bed hydrodynamics. Fluidization promotes particle motion and collisions, which generate electrostatic charge, while the resulting electrostatic forces modify particle trajectories, collision frequencies, local bed structure, and gas–solid interactions. Consequently, electrostatics and hydrodynamics are strongly coupled, and changes in one can significantly affect the other (Fotovat et al. 2017a; Sowinski et al. 2010). Electrostatic interactions may therefore influence key fluidization characteristics such as the minimum fluidization velocity, bubble dynamics, solids circulation, particle mixing, and entrainment behaviour (Alsmari et al. 2015; Fotovat et al. 2017b).

Several experimental and numerical studies have demonstrated that electrostatic charging can substantially alter bubbling behaviour. Dong et al. (2015) reported a reduction in bubble size and significant changes in fluidization behaviour with increasing particle charge. Numerical simulations by Jalalinejad et al. (2012) predicted that electrostatic charges can elongate bubbles and increase their rise velocity due to modifications of the force balance around the bubble interface. Subsequent experiments by Jalalinejad et al. (2016) confirmed that bubbles in highly charged beds are generally smaller and more elongated than in less-charged systems, while also exhibiting enhanced particle raining from the bubble roof. Tan et al. (2019) and Tan et al. (2018) further demonstrated that electrostatic forces modify gas leakage, particle penetration, and gas–solid exchange processes around the bubble, thereby affecting both bubble development and overall bed hydrodynamics. Collectively, these studies indicate that electrostatic interactions have a significant influence on bubble evolution; however, the mechanisms governing these changes remain insufficiently understood.

Numerical investigations have provided further insight into the mechanisms underlying these observations. Hassani et al. (2013) demonstrated that electrostatic repulsion between similarly charged particles may increase the porosity of the emulsion phase, reduce bubble size, suppress solids circulation, and decrease particle diffusivity. Similarly, Rokkam et al. (2010) reported that electrostatic effects can alter particle segregation and modify overall bed hydrodynamics. These studies suggest that electrostatic interactions influence not only particle motion but also the local porosity, gas

distribution, bubble stability, and overall hydrodynamics of the bed.

Despite the growing body of experimental and numerical evidence, the mechanisms through which electrostatic forces modify fluidized-bed hydrodynamics remain incompletely understood (Fotovat et al. 2018; Fotovat et al. 2017a). Although previous studies have demonstrated that particle charging affects bubble characteristics, bed expansion, solids circulation, and fluidization behaviour, the relationships between particle charging, local bed structure, and macroscopic hydrodynamics have not yet been fully established (Fotovat et al. 2017a; Manafi et al. 2019). In particular, it remains unclear how electrostatic interactions alter minimum fluidization behaviour, local porosity distributions, and the evolution of bubbles within the bed. Consequently, many observations reported in the literature remain largely qualitative and are difficult to interpret within the framework of classical fluidization theory. A quantitative assessment of how electrostatic interactions modify local porosity, bubble evolution, and fluidization characteristics is therefore required.

One particularly important unresolved issue is the influence of electrostatic forces on bubble growth and bubble stability. Experimental studies have consistently reported changes in bubble size, shape, and behaviour in charged fluidized beds (Dong et al. 2015; Jalalinejad et al. 2012; Jalalinejad et al. 2016; Tan et al. 2018). Numerical investigations have further suggested that electrostatic interactions increase the porosity of the emulsion phase and modify the gas distribution within the bed (Hassani et al. 2013; Rokkam et al. 2010). An increase in emulsion-phase porosity may allow a larger fraction of the gas flow to permeate through the particulate phase rather than contributing to bubble growth. Consequently, less excess gas may be available for bubble formation, potentially resulting in smaller bubbles, enhanced gas leakage from bubbles into the surrounding emulsion phase, and ultimately particle penetration into the bubble, producing a more diffuse gas–solid interface and reducing the measured bubble area. Such a mechanism could provide a physical explanation for the reduced bubble sizes reported in previous experimental studies (Dong et al. 2015; Jalalinejad et al. 2012; Tan et al. 2018). However, direct numerical evidence linking electrostatic forces, local porosity variations, and bubble evolution remains limited.

Experimental investigation of these phenomena remains challenging because local charge distributions and particle-scale electrostatic interactions are difficult to measure directly within fluidized beds (Chen et al. 2003; Chen et al. 2006; Fotovat et al. 2017a; Sowinski et al. 2010). Most experimental techniques provide bed-averaged electrostatic measurements, making it difficult to establish direct relationships between electrostatic forces and local hydrodynamic behaviour. Numerical simulations therefore offer a powerful alternative for investigating the underlying mechanisms. In particular, DPM simulations enable simultaneous resolution of particle motion, gas flow, and inter-particle electrostatic forces, providing insight into local phenomena that are generally inaccessible through experiments alone (Deen et al. 2007; Hassani et al. 2013; Hoef et al. 2008). Such simulations are therefore well

suited for examining how electrostatic interactions influence fluidization behaviour across multiple length scales.

In Chapter 2, a hierarchical particle-cell method was developed to efficiently account for long-range electrostatic interactions in DPM simulations. The method significantly reduced the computational cost associated with electrostatic force calculations while maintaining good agreement with exact Coulomb-force evaluations. The availability of this computational framework enables detailed investigation of electrostatic effects on fluidized-bed hydrodynamics over a broad range of operating conditions.

The objective of this chapter is therefore to investigate how electrostatic forces influence the hydrodynamics of gas–solid fluidized beds. First, the effects of particle charging on minimum fluidization and bubbling behaviour are analysed using pressure-drop calculations, bed expansion, electrostatic effects on bubble formation, bubble growth, bubble morphology, and bubble collapse are investigated through controlled single-bubble injection simulations. The observed bubble behaviour is interpreted within the framework of classical fluidization theory to gain insight into the mechanisms responsible for bubble shrinkage and particle penetration into bubbles. Finally, the influence of electrostatics on solids circulation patterns and granular temperature is quantified to provide a broader understanding of how particle charging modifies fluidization behaviour.

Through these investigations, this chapter aims to bridge classical fluidization theory and particle-scale electrostatic interactions, thereby providing a mechanistic understanding of how electrostatic forces modify bubbling fluidization and identifying the key hydrodynamic consequences of particle charging.

3.2 Discrete Particle Model

The simulations presented in this chapter are performed using a Discrete Particle Model (DPM), an Euler–Lagrange approach that combines Computational Fluid Dynamics (CFD) and the Discrete Element Method (DEM) to study the hydrodynamics of fluidized beds containing charged particles. The DPM enables a detailed particle-scale investigation by tracking the motion of individual particles, although the associated computational cost restricts simulations to relatively small system sizes (Deen et al. 2007; Hoef et al. 2008; Hoomans et al. 1996). In this approach, each particle possesses its own physical properties, including position, velocity, mass, and electrostatic charge, and is tracked individually using Newton's laws of motion. Meanwhile, the gas phase is treated as a continuum and solved on an Eulerian background mesh. The momentum exchange between the gas and particle phases is represented through inter-phase coupling terms, such that the drag force acting on the particles appears as an equal and opposite momentum source term in the gas-phase equations. Since the numerical methodology

has already been described in detail previously, only the governing equations relevant to the present hydrodynamic simulations are briefly summarized here.

In the DPM framework, conservation equations are solved for the gas phase, while the translational motion of individual particles is obtained from Newton's second law. The gas and particle phases are coupled through inter-phase momentum exchange terms that account for the drag force acting between both phases. The governing equations employed in the present work are summarized below.

The gas phase is governed by the continuity and momentum equations,

$$\frac{\partial(\varepsilon_g \rho_g)}{\partial t} + \nabla \cdot (\varepsilon_g \rho_g \vec{u}_g) = 0 \tag{3.1}$$

$$\frac{\partial(\varepsilon_g \rho_g \vec{u}_g)}{\partial t} + \nabla \cdot (\varepsilon_g \rho_g \vec{u}_g \vec{u}_g) = -\varepsilon_g \nabla p_g - \nabla \cdot (\varepsilon_g \vec{\tau}_g) - S_p + \varepsilon_g \rho_g \vec{g}. \tag{3.2}$$

Here, ε_g, ρ_g, p_g, and $\vec{\tau}_g$ denote the gas voidage, density, pressure, and viscous stress tensor, respectively, while $\vec{u}_g$ represents the local gas velocity. The superficial gas velocity and minimum fluidization velocity are denoted by U and U_{mf}, respectively. The source term S_p accounts for the momentum exchange between the gas and particle phases.

$$S_p = \frac{1}{V_{\text{cell}}} \int \sum_{k=1}^{N_p} \frac{V_{p,k}\beta}{1-\varepsilon_g} (\vec{u}_g - \vec{u}_{p,k}) \delta(\vec{u}_g - \vec{u}_{p,k}) \tag{3.3}$$

where V_{cell} is the computational cell volume, N_p is the number of particles contained within the cell, and β is the inter-phase momentum-exchange coefficient. The coefficient β is evaluated using the combined Ergun and Wen–Yu drag correlations, in which the Ergun correlation is applied in dense regions and the Wen–Yu correlation is applied in dilute regions (Delebarre 2004; Ergun 1952):

$$\frac{\beta d_p^2}{\mu} = \begin{cases} 150\dfrac{1-\varepsilon_g}{\varepsilon_g} + 1.75\,\varepsilon_s Re, & \varepsilon_g < 0.8, \\ \dfrac{3}{4} C_D Re (1-\varepsilon_g) \varepsilon_g^{-2.65}, & \varepsilon_g \geq 0.8. \end{cases} \tag{3.4}$$

The translational and rotational motion of each particle is governed by Newton's second law,

$$m_p \frac{d\vec{u}_p}{dt} = \vec{F}_{\text{contact}} + \vec{F}_{\text{external}}, \tag{3.5}$$

where $\vec{F}_{\text{contact}}$ represents the forces arising from particle–particle and particle–wall collisions. The external forces considered in the simulations are

$$\vec{F}_{\text{external}} = m_p \vec{g} - V_p \nabla p_g + \frac{V_p \beta}{1-\varepsilon_g} (\vec{u}_g - \vec{u}_p) + \vec{F}_{\text{electrostatic}}, \tag{3.6}$$

which correspond to the gravitational, pressure-gradient, drag, and electrostatic forces, respectively. Particle trajectories are integrated using the Beeman integration scheme (Beeman 1976), whereas the inelastic particle contacts are resolved using the linear spring–dashpot contact model proposed by Cundall et al. (1979).

Electrostatic interactions are represented through particle–particle and particle–wall forces. The total electrostatic force acting on a particle is given by

$$\vec{F}_{\text{electrostatic}} = \vec{F}^{e}_{p-p} + \vec{F}^{e}_{p-w}, \tag{3.7}$$

where $\vec{F}^{e}_{p-p}$ and $\vec{F}^{e}_{p-w}$ denote the particle–particle and particle–wall electrostatic forces, respectively. Detailed formulations of these forces and their numerical implementation are provided in Chapter 2.

Accurate evaluation of electrostatic interactions requires accounting for long-range Coulomb forces between all charged particles. Consequently, direct calculation of all pairwise interactions becomes computationally prohibitive for large systems. Therefore, the hierarchical particle–cell method developed and validated in Chapter 2 is employed throughout this work.

The hierarchical particle–cell method combines direct Coulomb-force calculations for nearby particles with lumped-charge approximations for distant particles. Short-range interactions are evaluated explicitly within a fine-grid region surrounding the target particle, whereas interactions with more distant particles are represented using lumped charges defined on fine and coarse computational grids. This approach substantially reduces the computational cost while maintaining high accuracy in the electrostatic force calculations.

A schematic overview of the hierarchical particle–cell method employed throughout this chapter is presented in Figure 3.1.

3.3 Minimum Fluidization and Bubbling Velocity

The minimum fluidization velocity (U_{mf}) is one of the most important parameters used to characterize the hydrodynamic behaviour of gas–solid fluidized beds. It represents the transition from a fixed bed to a fluidized state, occurring when the drag force exerted by the gas balances the effective weight of the particles (Ergun 1952; Kunii et al. 1994). For Geldart B particles, bubbling typically begins shortly after minimum fluidization is reached, such that the minimum bubbling velocity (U_{mb}) is often close to U_{mf} (Geldart 1973; Kunii et al. 1994). Consequently, both quantities play an important role in determining solids mixing, gas–solid contact, bubble formation, and overall reactor performance.

In conventionally fluidized beds, the onset of fluidization is governed primarily by the balance between gravitational and hydrodynamic drag

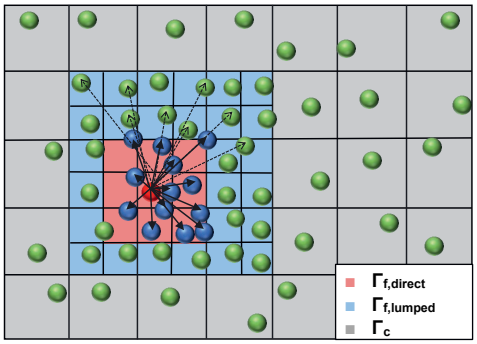


Figure 3.1: Hierarchical particle–cell method representation for electrostatic force calculations. The computational domain is divided into three zones: (1) $\Gamma_{f,\text{direct}}$: Zone for direct particle-particle Coulombic calculations involving the target particle (red particle) and nearby real particles; (2) $\Gamma_{f,\text{lumped}}$: Zone for fine-grid calculations using lumped particle approximations; (3) Γ_c: Coarse-grid zone where long-range interactions are computed using lumped particle methods.

forces. In beds containing charged particles, however, electrostatic forces introduce an additional contribution to the particle force balance. Repulsive electrostatic interactions can modify the local bed structure, alter the voidage distribution, and influence gas flow through the bed. As a result, the classical interpretation of minimum fluidization and bubbling behaviour may no longer be directly applicable.

Previous experimental studies have reported that particle charging can significantly affect fluidization behaviour. Dong et al. (2015) reported a reduction in bubble size and changes in fluidization behaviour with increasing particle charge. Numerical studies have also suggested that electrostatic interactions can increase emulsion-phase porosity and modify gas distribution within fluidized beds (Hassani et al. 2013; Rokkam et al. 2010). These observations indicate that electrostatic forces can substantially influence the hydrodynamics of fluidized beds, although the underlying mechanisms remain incompletely understood.

The objective of this section is therefore to investigate how electrostatic interactions affect minimum fluidization and bubbling behaviour. First, the simulation methodology used to determine U_{mf} and U_{mb} is described. Subsequently, pressure-drop numerical measurements and local bed structure are analysed to assess how particle charging influences fluidization behaviour and contributes to the development of bed heterogeneity.

Simulation set-up

To investigate the influence of electrostatic forces on minimum fluidization and bubbling behaviour, simulations were performed in a pseudo-two-dimensional fluidized bed containing 54,000 mono-sized polyethylene particles. Nitrogen was used as the fluidizing gas. In addition to an uncharged reference case, mono-charged systems with different charge levels were simulated by assigning an identical charge to all particles. The applied charge levels are expressed as percentages of the maximum particle charge. Based on the particle size and dielectric properties of polyethylene, the maximum particle charge was estimated to be approximately 130 pC per particle using the correlation proposed by Jiang et al. (Jiang et al. 1994).

The particles were initially generated in a randomly packed configuration and allowed to settle under gravity until a stable packed bed was obtained. Subsequently, gas flow was introduced through the distributor at the bottom of the bed. To determine the minimum fluidization velocity, the superficial gas velocity was increased gradually from zero to a value exceeding the onset of bubbling. After reaching the maximum velocity, the gas flow rate was reduced again to examine possible hysteresis effects and to facilitate identification of the transition between the fixed and fluidized states.

During the simulations, the pressure drop across the bed was monitored continuously as a function of superficial gas velocity. Simultaneously, the bed structure and local porosity distributions were recorded to support the interpretation of the pressure-drop measurements. Since electrostatic interactions may alter the local voidage distribution and gas permeability of the bed, pressure-drop measurements alone may not be sufficient to identify fluidization behaviour in highly charged systems. Therefore, local bed structure is examined in addition to the conventional pressure-drop analysis.

The computational domain and operating conditions are summarized in Table 3.1. Unless stated otherwise, all particle properties, gas properties, contact-model parameters, and numerical settings are identical to those validated in Chapter 2. The selected time-step size and grid resolution were previously shown to provide grid-independent hydrodynamic predictions while maintaining reasonable computational cost.

Minimum Fluidization Velocity

The minimum fluidization velocity was determined using the conventional pressure-drop method employed in fluidization experiments (Ergun 1952; Kunii et al. 1994). As the superficial gas velocity increases, the pressure drop across a packed bed rises until the drag force exerted by the gas balances the effective weight of the particles. Beyond this point, the bed enters the fluidized state and the pressure drop remains approximately constant. The

Table 3.1: Simulation parameters

Parameters	Value
Number of particles [-]	54000
Particle diameter [m]	1.0×10^{-3}
Particle density [kg m^{-3}]	890
Bed height [m]	0.360
Bed width [m]	6.50×10^{-2}
Bed depth [m]	1.50×10^{-2}
Time step size [s]	1.0×10^{-6}
Grid size [m]	2.50×10^{-3}
Particle restitution coefficient [-]	0.9
Normal spring stiffness [N/m]	7000
Tangential spring stiffness [N/m]	2000
Friction Coefficient [-]	0.3

minimum fluidization velocity is therefore identified from the intersection of the fixed-bed and fluidized-bed regions of the pressure-drop curve.

The procedure was first applied to the uncharged system. The superficial gas velocity was decreased gradually while monitoring the pressure drop across the bed. Figure 3.2 shows the resulting pressure-drop curve. As expected for Geldart B particles, a clear transition from the fixed-bed regime to the fluidized regime is observed. Based on the intersection of the two regions, the minimum fluidization velocity of the uncharged system was determined to be approximately $U_{mf} = 0.265$ m s^{-1}.

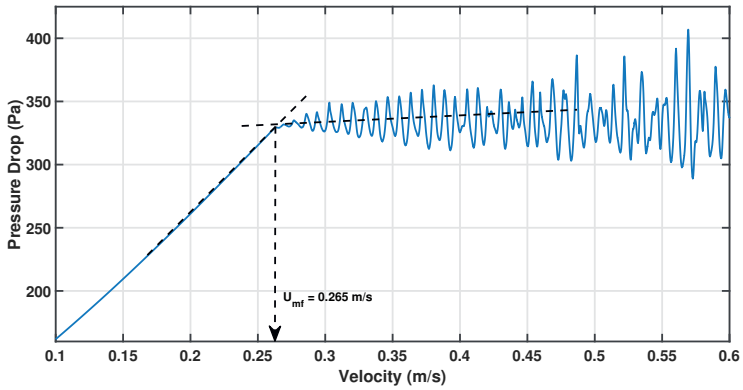


Figure 3.2: Pressure drop as a function of superficial gas velocity for the uncharged bed. The intersection of the fixed-bed and fluidized-bed regions gives the minimum fluidization velocity.

Figure 3.3 compares the pressure-drop behaviour of the uncharged bed with beds containing charged particles. For the lower charge level (0.1% of the maximum particle charge, corresponding to 0.13 pC per particle), the overall pressure-drop behaviour remains similar to that of the uncharged bed. The pressure-drop curve closely follows that of the uncharged bed, and the transition between the packed and fluidized states can still be identified relatively clearly, indicating that electrostatic interactions at this charge level have only a limited influence on the global fluidization behaviour.

For the higher charge level (1% of the maximum particle charge, corresponding to 1.30 pC per particle), the pressure-drop curve begins to deviate from the fixed-bed behaviour at gas velocities well below the minimum fluidization velocity of the uncharged bed. This gradual deviation indicates that local regions within the bed begin to expand before the onset of global fluidization. Consequently, the transition from the packed bed to the fully fluidized state becomes more diffuse, reflecting the development of bed heterogeneity. In contrast to the uncharged case, where a relatively sharp transition is observed, the charged bed exhibits a broader transition region, making the determination of a unique minimum fluidization velocity based solely on the global pressure drop increasingly ambiguous. Although the apparent minimum fluidization velocity increases with particle charge, the reduction in pressure-drop fluctuations suggests that the bed no longer fluidizes uniformly, but instead consists of regions experiencing different local hydrodynamic conditions.

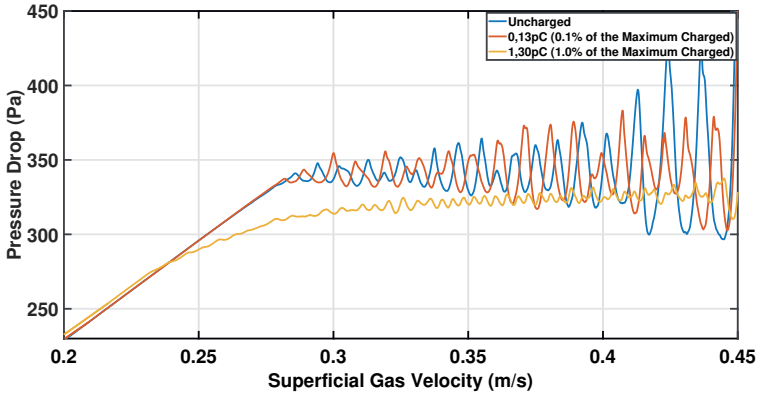


Figure 3.3: Pressure drop as a function of superficial gas velocity for uncharged and charged particle beds.

For Geldart B particles, bubbling commences shortly after minimum fluidization is reached. The onset of visible pressure-drop fluctuations in Figure 3.3 therefore provides an approximate indication of the minimum bubbling velocity (U_{mb}). As the particle charge increases, the amplitude of the pressure-drop fluctuations decreases markedly, indicating reduced bubble

activity. This behaviour suggests that electrostatic interactions promote gas percolation through the increasingly porous emulsion phase.

The pressure-drop results suggest that electrostatic interactions influence not only the onset of fluidization but also the spatial uniformity of fluidization throughout the bed. However, pressure-drop measurements alone do not provide sufficient information to identify the origin of the observed oscillations. To investigate this behaviour further, the local bed structure is analysed in the next subsection through time-averaged porosity and solids-holdup distributions.

Local Bed Structure and Porosity

The pressure-drop analysis indicates that increasing particle charge introduces significant fluctuations in the transition region between the fixed-bed and fluidized-bed states. However, pressure-drop measurements provide only global information and do not reveal how fluidization varies locally throughout the bed. To investigate the origin of these fluctuations, the time-averaged solids holdup was evaluated at different bed heights.

Figure 3.4 shows the vertical distribution of the time-averaged solids holdup for uncharged and charged beds. The uncharged bed exhibits a relatively uniform profile, indicating that fluidization occurs rather homogeneously throughout the bed. In contrast, significant deviations are observed when electrostatic forces are present.

For the charged systems, the solids holdup near the bottom of the bed is higher than in the upper regions, indicating that particles accumulate towards the lower part of the bed. At the same time, the upper regions exhibit a lower solids holdup and therefore a higher local porosity. This non-uniform distribution suggests that electrostatic interactions promote the development of bed heterogeneity. Instead of fluidizing uniformly, different sections of the bed experience different local conditions.

The increase in local porosity is particularly important because it can significantly alter the gas distribution within the bed. In classical fluidization theory, excess gas above minimum fluidization contributes to bubble formation and growth. However, when electrostatic repulsion increases the porosity of the emulsion phase, a larger fraction of the gas may pass directly through the particulate phase rather than being incorporated into bubbles. Consequently, less excess gas is available for bubble growth.

This observation provides a possible explanation for the oscillatory pressure-drop behaviour observed in Figure 3.3. The gas flow no longer interacts with a bed of approximately uniform structure, but instead encounters regions of different local porosity and permeability. As a result, the bed exhibits heterogeneous fluidization behaviour, making the determination of a unique minimum fluidization velocity increasingly difficult from pressure-drop measurements alone.

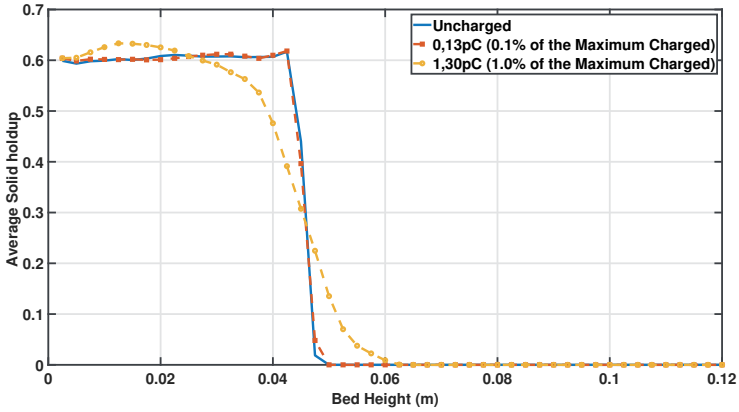


Figure 3.4: Time-averaged solids holdup at different bed heights for uncharged and charged particle systems.

Furthermore, the porosity results suggest a possible mechanism for the reduction in bubble size reported experimentally by Dong et al. (2015) and observed in charged systems discussed later in this chapter. If a larger fraction of the gas permeates through the emulsion phase, the gas available for bubble growth decreases, leading to smaller bubbles and potentially enhanced bubble shrinkage or collapse during their rise through the bed.

3.4 Bubble Dynamics

Bubble behaviour plays a central role in determining the hydrodynamics of bubbling fluidized beds because it directly influences gas–solid contact, solids circulation, mixing, and mass transfer (Kunii et al. 1991; Kunii et al. 1994). The previous section showed that electrostatic interactions modify the local bed structure and increase bed heterogeneity. However, pressure-drop measurements alone do not provide sufficient information to explain how electrostatic forces alter bubble formation and development. To investigate these mechanisms in greater detail, controlled single-bubble injection simulations were performed.

Single-bubble simulations provide a convenient method for isolating the interaction between a bubble and the surrounding particle phase, eliminating complications associated with bubble coalescence and splitting in freely bubbling beds. Similar approaches have previously been employed to investigate bubble behaviour in both uncharged and charged fluidized systems (Jalalinejad et al. 2012; Jalalinejad et al. 2016; Tan et al. 2019; Tan et al. 2018). By studying the evolution of an individual bubble, direct insight can be obtained into the influence of electrostatic forces on bubble shape, bubble

growth, particle penetration, and bubble stability.

Bubble Injection Methodology

The single-bubble simulations were performed using the same bed configuration and particle properties described in the previous section. The bed was first fluidized under background conditions for 1 s and subsequently allowed to stabilize for an additional 0.5 s. A single bubble was then injected through a central inlet located at the bottom of the bed.

Bubble injection was achieved through a central injection port with an area of 7.5×10^{-5} m^2. A gas jet with a velocity of 6 m s^{-1} was imposed for a duration of 0.1 s, resulting in the formation of a single isolated bubble. During the injection period, the remainder of the distributor continued to operate at approximately the minimum fluidization velocity, thereby maintaining the surrounding bed in a fluidized state while minimizing the formation of additional bubbles. This procedure enabled the evolution of a single bubble to be tracked and compared under different charging conditions. Bubble boundaries were identified using a solids-holdup threshold of $\varepsilon_s = 0.15$ ($\varepsilon_g = 0.85$), consistent with the criterion adopted throughout this work. To investigate the effect of electrostatic interactions, simulations were performed for uncharged particles and for particles carrying different fractions of the maximum particle charge. The resulting bubble behaviour was compared in terms of bubble morphology, particle penetration, bubble stability, and bubble size evolution during the ascent through the bed.

Bubble Morphology and Stability

The evolution of a single bubble in beds containing particles with different charge levels is shown in Figure 3.5. Significant differences are observed between the uncharged and charged systems.

In the contour plots, dark purple corresponds to a low solids volume fraction (gas-rich regions), whereas yellow indicates a high solids volume fraction representative of the dense emulsion phase. Figure 3.5(a) shows a large, well-defined bubble with a nearly particle-free core that exhibits the characteristic shape expected for bubbles rising in Geldart B particles. In Figure 3.5(b), the bubble remains recognizable, but becomes more elongated. At the same time, particles increasingly penetrate into the bubble interior, resulting in a more diffuse gas–solid interface. Consequently, the region with very low solids concentration becomes smaller and the boundary between the bubble and the surrounding emulsion becomes less distinct.

In Figure 3.5(c), this behaviour becomes even more pronounced. Although an elongated gas region is still present, particles occupy a substantial portion of the bubble interior, increasing the local solids holdup

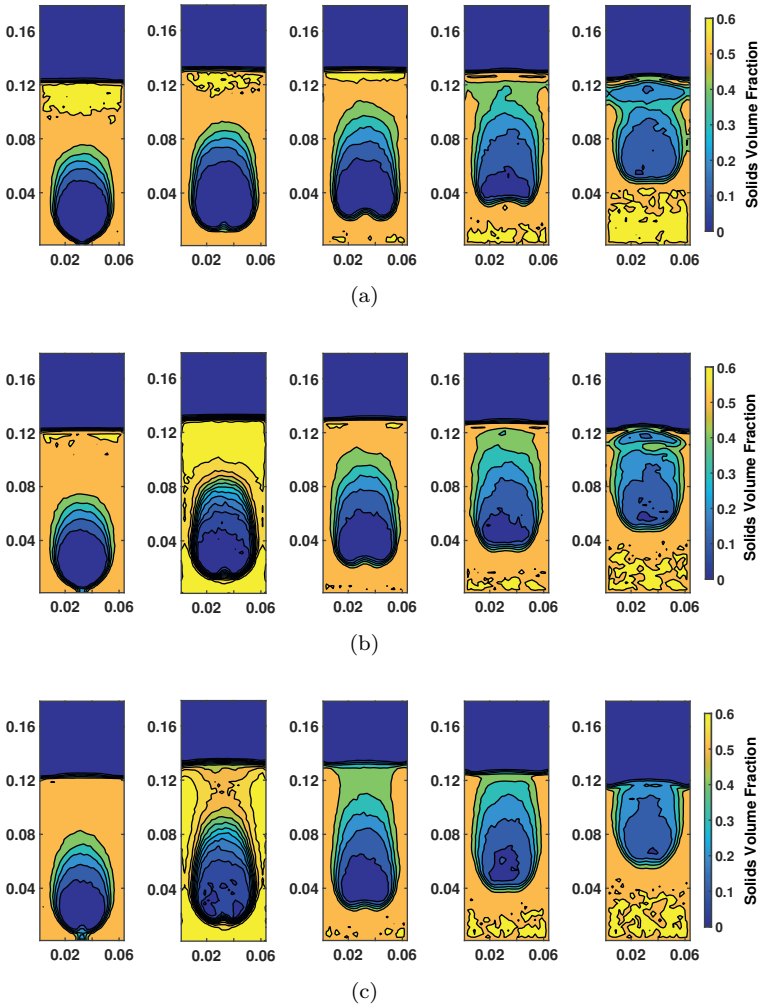


Figure 3.5: Contours of solids volume fraction during single-bubble rise: (a) uncharged particles, (b) 0.5% charged particles and (c) 1% charged particles.

and producing a diffuse interface. As a result, the particle-free core is considerably reduced.

These observations suggest that electrostatic forces significantly influence bubble stability. Rather than promoting bubble growth, electrostatic interactions facilitate particle intrusion into the bubble and suppress the development of a clearly defined gas void.

To investigate the bubble evolution over a longer travel distance, additional simulations were performed using a bed with approximately twice the original height. The results are presented in Figure 3.6.

The extended simulations confirm that increasing particle charge suppresses bubble development. While only minor differences are observed between the uncharged and weakly charged systems, substantial changes occur at higher charge levels. The bubble becomes progressively more elongated while its boundary becomes increasingly diffuse because of particle penetration into the gas region. Consequently, the particle-free core decreases and, for the highest charge levels, the bubble eventually loses its integrity before reaching the bed surface.

The observed behaviour is consistent with the porosity analysis presented in the previous section. As electrostatic repulsion increases the local porosity of the emulsion phase, a larger fraction of the gas flow can pass through the particulate phase rather than contributing to bubble growth. Consequently, the amount of excess gas available to maintain the bubble decreases, causing particle penetration and eventually bubble shrinkage or collapse.

Bubble Shrinkage and Area Evolution

The contour plots presented in the previous subsection indicate that electrostatic interactions significantly influence the evolution of bubbles as they rise through the bed. To quantify these observations, the bubble area was evaluated at the center section of the bed and compared for different charge levels.

Figure 3.7 shows the bubble area as a function of bubble position for the uncharged bed and for particles carrying 0.5% and 1% of the maximum particle charge. For all cases, the bubble area decreases gradually as the bubble rises. However, the rate of shrinkage increases substantially with increasing charge level.

Bubble identification was performed using a solids-holdup threshold of $\varepsilon_s = 0.15$. Consequently, the reported bubble area represents only the region satisfying this criterion rather than the entire visible gas region. As electrostatic interactions promote particle penetration into the bubble, portions of the diffuse gas–solid interface exceed the adopted threshold and are therefore classified as part of the emulsion phase. The measured bubble area should therefore be interpreted as the particle-poor core of the bubble rather than the entire visible gas-rich region.

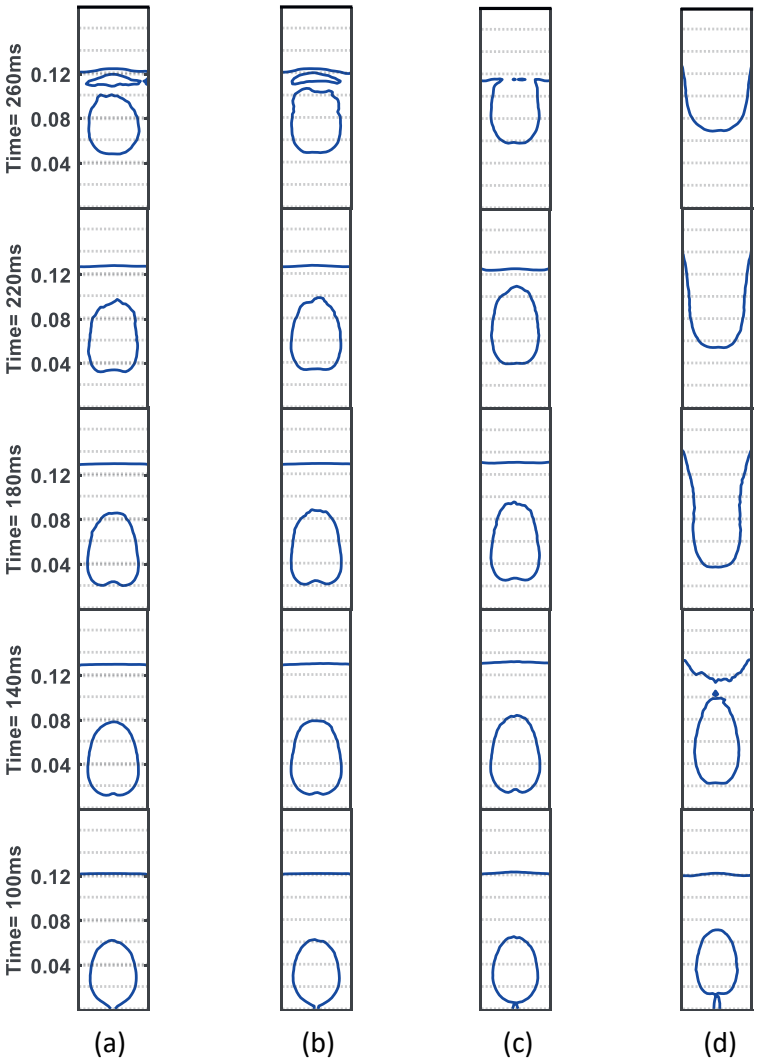


Figure 3.6: Comparison of single-bubble evolution for different particle charge levels in a bed with increased height: (a) uncharged, (b) 0.5%, (c) 1%, and (d) 2% of the maximum particle charge.

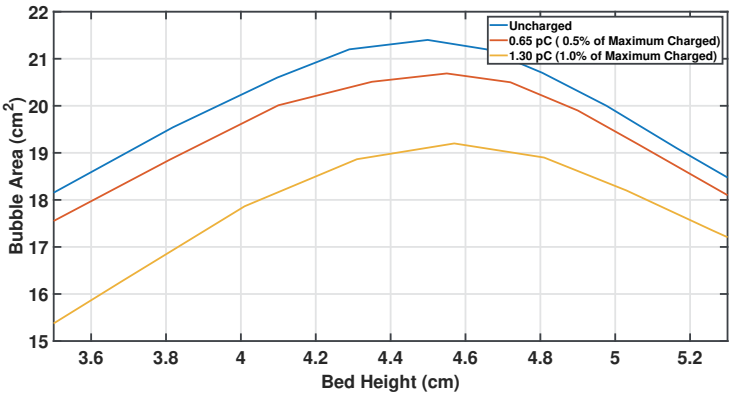


Figure 3.7: Evolution of bubble area during bubble rise for different particle charge levels.

As electrostatic interactions promote particle penetration into the bubble, the gas–solid interface becomes increasingly diffuse and the solids holdup near the bubble boundary increases. Consequently, portions of the elongated gas region no longer satisfy the adopted threshold and are classified as part of the emulsion phase. Therefore, the measured bubble area decreases even though the contour plots indicate that the overall gas region remains elongated.

The reduction in the measured bubble area is consistent with the experimental observations of Dong et al. (2015), who reported a decrease in bubble diameter with increasing particle charging. Similar behaviour was observed by Jalalinejad et al. (2016), who found that bubbles in highly charged beds were generally smaller and less stable than those in weakly charged systems. The present simulations therefore provide further evidence that electrostatic forces can substantially modify bubble evolution.

A possible explanation for this behaviour can be obtained by combining the bubble observations with the porosity results discussed in the previous section. Figure 3.4 showed that electrostatic repulsion increases the local porosity of the emulsion phase. In classical bubbling fluidization, the excess gas above minimum fluidization contributes to bubble growth and maintenance (Kunii et al. 1991; Kunii et al. 1994). However, when the emulsion phase becomes more permeable, a larger fraction of the gas can flow directly through the particulate phase instead of entering the bubble.

Consequently, the gas available for sustaining the bubble decreases as the bubble rises through the bed. This mechanism increases gas leakage from the bubble into the surrounding emulsion phase and promotes particle penetration into the bubble interior, both of which contribute to bubble shrinkage. At sufficiently high charge levels, the bubble may lose its integrity completely and collapse before reaching the bed surface, as observed in

Figure 3.6.

These observations provide a physical explanation for the smaller bubble sizes observed in charged beds. Rather than being caused solely by changes in bubble shape, the reduction in bubble size appears to be associated with modifications of the local bed structure and gas distribution induced by electrostatic interactions. The increased porosity of the emulsion phase allows more gas to bypass the bubble, thereby reducing the amount of excess gas available for bubble growth and stability.

The results therefore support the hypothesis proposed in the Introduction that electrostatic interactions modify bubble dynamics indirectly through changes in local porosity and gas permeability. This mechanism provides a link between particle-scale electrostatic forces and the macroscopic hydrodynamic behaviour observed in charged fluidized beds.

Comparison with Classical Bubble Theory

The bubble-shrinkage behaviour observed in the simulations can be interpreted in the context of classical bubble theory. In bubbling fluidized beds, the excess gas above minimum fluidization is assumed to form discrete bubbles that rise through a dense emulsion phase (Kunii et al. 1991; Kunii et al. 1994). The bubble size, rise velocity, and growth rate are determined by the partitioning of gas between the bubble and emulsion phases. Consequently, any mechanism that alters gas flow through the emulsion phase has the potential to influence bubble dynamics.

According to the bubble-growth correlation proposed by Mori and Wen (Mori et al. 1975), bubble diameter increases with bed height as bubbles coalesce and absorb excess gas while rising through the bed. Classical bubble models further assume that the emulsion phase remains close to minimum fluidization conditions, such that most of the excess gas is available for bubble growth (Kunii et al. 1991; Kunii et al. 1994). In the uncharged simulations, the observed bubble behaviour is generally consistent with this framework, with the injected bubble remaining clearly distinguishable throughout its ascent.

In contrast, the charged systems exhibit a progressive reduction in bubble area and increased particle penetration into the bubble region. The porosity analysis presented previously suggests that electrostatic repulsion increases the local voidage of the emulsion phase. As a result, a larger fraction of the gas can percolate through the dense phase instead of contributing to bubble growth. This behaviour is not accounted for in classical bubble models, which assume that the emulsion phase remains close to the minimum fluidization condition.

The increased permeability of the emulsion phase provides a plausible mechanism for the observed bubble shrinkage. If a greater fraction of the gas is transported through the particulate phase, the amount of excess gas available to sustain the bubble decreases. Consequently, bubble growth is

suppressed and gas leakage from the bubble into the surrounding emulsion phase becomes more significant. Under sufficiently strong electrostatic interactions, this mechanism may ultimately lead to bubble collapse before the bubble reaches the bed surface.

These observations are consistent with experimental findings reported by Dong et al. (2015), who observed smaller bubble diameters in charged fluidized beds, and with the single-bubble studies of Jalalinejad et al. (2012) and Jalalinejad et al. (2016) and Tan et al. (2019) and Tan et al. (2018), who reported significant electrostatic effects on bubble evolution and gas–solid exchange processes. The present simulations provide additional support for the hypothesis that electrostatic interactions modify bubble behaviour through changes in local bed structure and gas distribution.

The present observations may also help explain some of the contradictory trends reported in the literature regarding the influence of electrostatic charging on bubble size. Bubble identification requires the selection of a threshold separating the bubble from the surrounding emulsion phase. When electrostatic interactions produce a more diffuse gas–solid interface through particle penetration, the measured bubble size becomes sensitive to the adopted criterion. Consequently, different bubble definitions or image-processing methods may lead to different conclusions regarding whether electrostatic charging increases or decreases bubble size.

Although a quantitative modification of the classical bubble correlations is beyond the scope of the present work, the results suggest that electrostatic forces influence bubbling fluidization indirectly by altering emulsion-phase porosity and permeability. The combination of increased gas leakage through the particulate phase and enhanced particle penetration into the bubble provides a consistent physical explanation for the reduced bubble sizes observed in both the simulations and previous experimental studies.

3.5 Particle Dynamics

The previous sections demonstrated that electrostatic interactions modify both fluidization behaviour and bubble dynamics. Changes in bubble size, bubble stability, and local porosity are expected to influence particle motion throughout the bed. Conversely, electrostatic forces act directly on the particles and may alter circulation patterns, mixing behaviour, and velocity fluctuations. To better understand the mechanisms responsible for the observed hydrodynamic changes, the influence of electrostatic interactions on particle circulation and granular temperature is analysed in this section.

Bed Morphology and Bubble Activity

Snapshots of the fluidized bed provide a qualitative overview of the influence of electrostatic interactions on the overall bed structure. Figure 3.8 compares the behavior of uncharged particles with particles carrying 2% of the maximum charge.

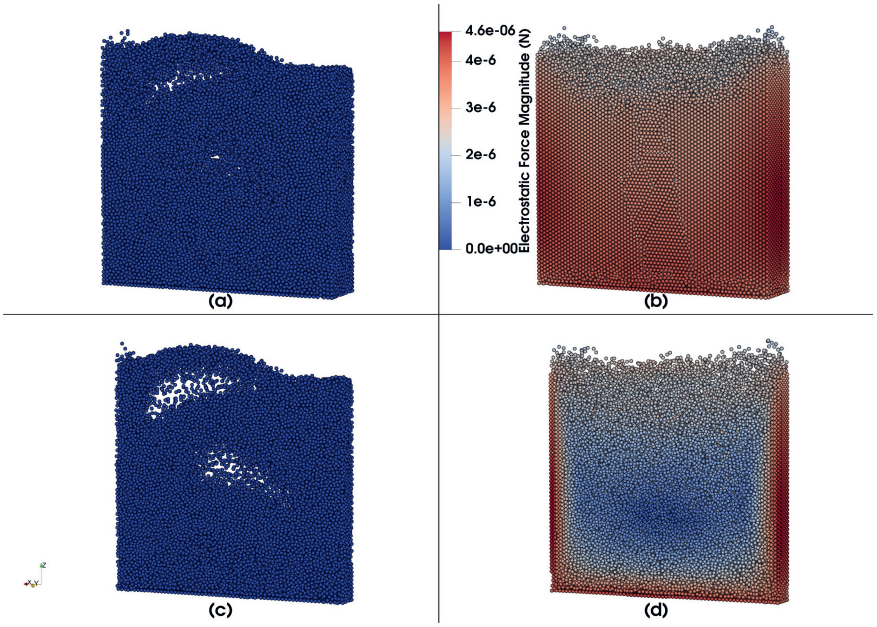


Figure 3.8: Snapshots of uncharged and charged fluidized beds, coloured according to the magnitude of the electrostatic force acting on each particle, with blue indicating low electrostatic forces and red indicating high electrostatic forces: (a) Uncharged bed, wall section (b) Charged bed wall section (c) Uncharged bed, interior section (d) Charged bed, interior section.

The uncharged system exhibits the characteristic bubbling behavior of a Geldart B fluidized bed, with clearly distinguishable bubbles forming, rising, and erupting at the bed surface. In contrast, the charged system displays a substantial reduction in visible bubble activity. The elongated gas regions observed in the charged bed are less clearly distinguishable because particles penetrate into the bubble interior, producing diffuse gas–solid interfaces.

Another notable feature of the charged bed is the increased tendency for particles to accumulate near the walls. This behavior is associated with electrostatic interactions and results in increased particle deposition near the walls. Such wall deposition has frequently been reported as an important operational consequence of electrostatic charging in fluidized beds (Fotovat et al. 2017a; Hendrickson 2006; Zhang et al. 2021).

The snapshots therefore provide visual evidence that electrostatic forces suppress bubble activity while simultaneously promoting particle accumulation near the walls. These observations are consistent with the porosity distributions and bubble analyses discussed previously and suggest that particle motion throughout the bed is significantly altered by electrostatic interactions.

Circulation Patterns

Particle circulation in bubbling fluidized beds is primarily induced by rising bubbles. As bubbles ascend, particles are displaced upwards in the wake region and subsequently descend near the walls, producing large-scale circulation loops throughout the bed (Kunii et al. 1991; Kunii et al. 1994). Since the previous section demonstrated that electrostatic forces suppress bubble growth and increase bubble shrinkage, significant modifications of particle circulation are expected.

Figure 3.9 compares the time-averaged particle velocity field for uncharged particles and particles carrying 2.6 pC of charge. In the uncharged system, the classical circulation pattern of a bubbling fluidized bed is observed, with two dominant circulation loops extending over most of the bed height. Particles rise through the central region of the bed and descend close to the walls.

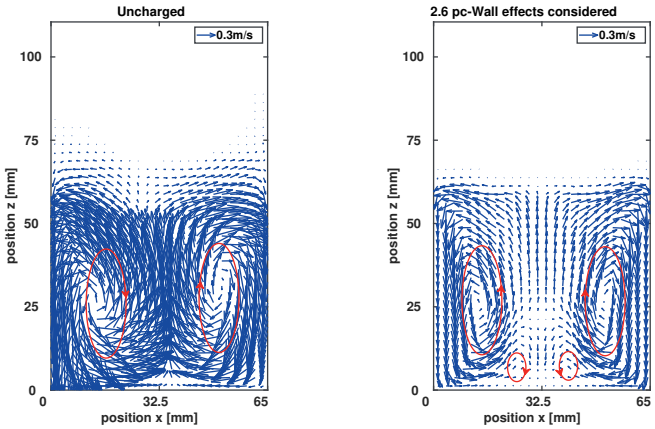


Figure 3.9: Time-averaged particle circulation patterns for uncharged and charged systems.

In the charged system, the circulation structure changes substantially. Although the general circulation pattern remains present, additional local circulation loops appear near the bottom of the bed. At the same time, the magnitude of the particle velocities decreases significantly. These

observations indicate that electrostatic interactions suppress particle mobility while simultaneously introducing local variations in particle motion. The reduction in particle velocity is consistent with the previously observed reduction in bubble activity and bubble size.

The circulation patterns therefore support the conclusion that electrostatic interactions modify fluidized-bed hydrodynamics not only through direct forces acting on particles, but also indirectly through changes in bubble behaviour and gas distribution.

Influence of Wall Interactions

In the main simulations, particle–wall image-charge forces are neglected, as stated in Chapter 2. To separately assess their influence, an additional set of simulations was performed in which image-charge forces generated by the reactor walls were included. These forces may contribute to particle accumulation near the walls and may therefore influence circulation patterns.

Figure 3.10 compares circulation patterns obtained with and without particle–wall image-charge forces. The first row corresponds to simulations in which both particle–particle and particle–wall electrostatic forces are included, whereas the second row corresponds to the main model configuration, in which particle–wall image-charge forces are neglected.

The results indicate that the influence on the circulation pattern appears to be limited. The principal hydrodynamic changes observed in the charged bed are therefore attributed to interparticle electrostatic interactions.

Furthermore, particles exhibit an increased tendency to accumulate near the bottom corners and close to the walls when electrostatic forces are active. This behaviour is consistent with the tendency of charged particles to migrate towards regions of reduced electric field intensity. The accumulation of solids near the walls further contributes to the heterogeneous structure observed previously in the solids-holdup profiles.

Granular Temperature

To further quantify the influence of electrostatic interactions on particle motion, the granular temperature was evaluated throughout the bed. Granular temperature is a measure of the kinetic energy associated with random particle velocity fluctuations and is commonly used to characterize particle mobility in fluidized beds (Godlieb et al. 2008; Wang et al. 2010).

The granular temperature is calculated as

$$\theta = \frac{1}{3}(\theta_x + \theta_y + \theta_z) \tag{3.8}$$

where the granular temperature in each direction is given by

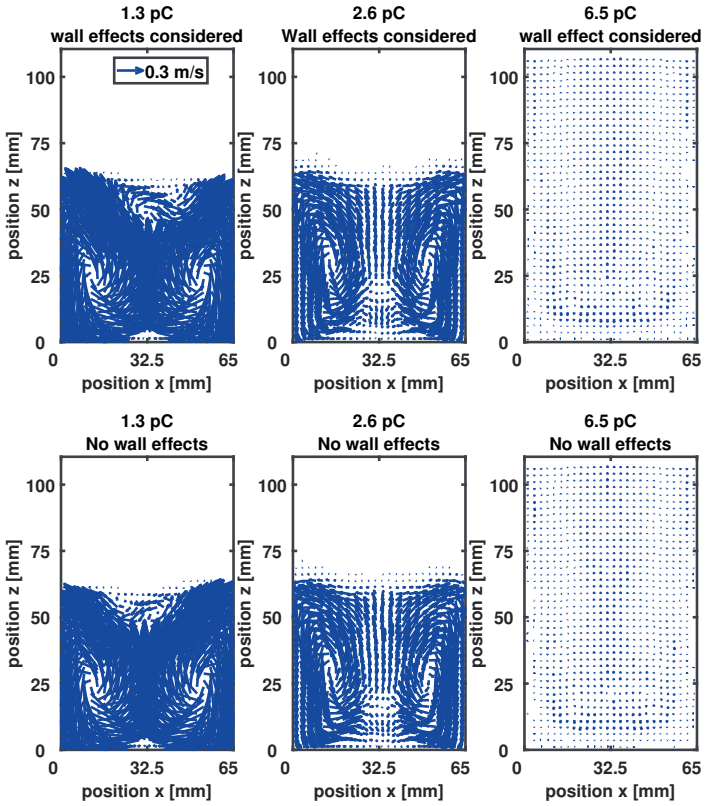


Figure 3.10: Comparison of circulation patterns obtained with and without particle–wall electrostatic interactions.

$$\theta_k = \frac{1}{N_p} \sum_{i=1}^{N_p} (v_{k,i} - \bar{v}_k)^2 \tag{3.9}$$

where N_p is the number of particles within the computational cell, $v_{k,i}$ is the velocity of particle i in direction k, and $\bar{v}_k$ is the mean particle velocity in that direction.

Figure 3.11 compares the time-averaged granular temperature distributions for the charged and uncharged systems.

The uncharged system exhibits relatively high granular temperatures throughout much of the bed, particularly in regions influenced by bubble passage and particle circulation. In contrast, the charged system displays a significant reduction in granular temperature, especially near the walls.

The reduction in granular temperature indicates that electrostatic forces suppress random particle motion and reduce particle velocity fluctuations.

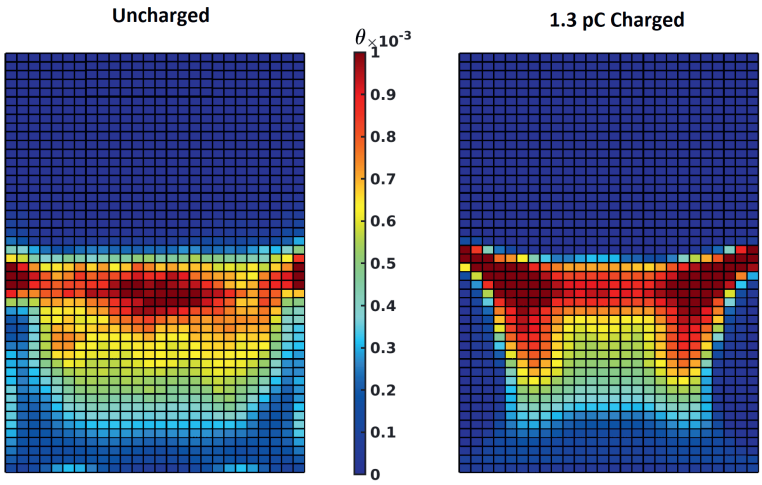


Figure 3.11: Time-averaged granular temperature distributions for uncharged and 1,3 pC charged particles in fluidized beds.

This observation is consistent with the reduced particle circulation velocities observed in Figure 3.9, also provides a possible explanation for the bubble elongation observed in the earlier simulations, as the restricted lateral motion of particles limits bubble expansion in the horizontal direction. Together, these results demonstrate that electrostatic interactions decrease particle mobility throughout the bed, leading to weaker mixing and a more heterogeneous fluidization state.

The circulation and granular-temperature analyses therefore provide further evidence that electrostatic interactions influence fluidized-bed hydrodynamics through a combination of direct particle forcing and indirect modifications of bubble dynamics and local bed structure.

3.6 Discussion

Electrostatic Modification of Bed Structure

The pressure-drop and solids-holdup analyses demonstrate that electrostatic interactions modify the internal structure of the fluidized bed. While the uncharged bed exhibits relatively uniform fluidization, charged beds develop significant vertical variations in solids holdup. Increased solids accumulation near the bottom of the bed and increased porosity in the upper regions indicate the development of bed heterogeneity.

These observations suggest that electrostatic repulsion alters particle

packing and local voidage distributions throughout the bed. As a consequence, the gas encounters regions of different permeability, resulting in non-uniform gas distribution and fluidization behaviour.

Mechanism of Bubble Shrinkage

The bubble analyses showed that increasing particle charge decreases bubble area and promotes bubble collapse. Combining these observations with the porosity measurements suggests a consistent physical mechanism.

Electrostatic repulsion increases the porosity of the emulsion phase. Consequently, a larger fraction of the gas flow can permeate through the particulate phase rather than being incorporated into bubbles. This reduces the amount of excess gas available for bubble growth and maintenance. As a result, bubbles become smaller, particle penetration into the bubble increases, and bubble collapse may occur before the bubble reaches the bed surface.

The observed reduction in bubble size is therefore interpreted as an indirect consequence of porosity modifications induced by electrostatic forces.

This interpretation is consistent with the smaller bubble sizes reported by Dong et al. (2015) and provides a possible explanation for the bubble behaviour observed experimentally and numerically in charged fluidized beds.

Implications for Classical Fluidization Theory

Classical bubble theories such as those of Mori and Wen (Mori et al. 1975) and Kunii and Levenspiel (Kunii et al. 1991; Kunii et al. 1994) assume that the emulsion phase remains close to minimum fluidization conditions and that excess gas is predominantly available for bubble growth. The present results suggest that electrostatic interactions can modify this assumption by increasing emulsion-phase permeability.

Under such conditions, a larger portion of the gas flow bypasses the bubble phase and travels through the emulsion phase. Consequently, classical bubble-growth behaviour is weakened, resulting in a reduction of the particle-free bubble core and the measured bubble area. The present results therefore indicate that electrostatic interactions influence bubbling fluidization primarily through their effect on local bed structure rather than through direct modification of bubble mechanics.

Consequences for Particle Dynamics

The reduction in bubble activity has direct implications for particle motion. Smaller and less stable bubbles generate weaker solids circulation, resulting

in lower particle velocities throughout the bed. This effect is reflected in both the circulation-pattern analysis and the granular-temperature distributions.

The reduced granular temperature indicates weaker particle velocity fluctuations and therefore reduced particle mixing. Electrostatic interactions thus influence fluidized-bed hydrodynamics at multiple scales, from particle-scale forces to bed-scale circulation behaviour.

Overall, the results support the following mechanism. Electrostatic repulsion modifies the local bed structure by increasing emulsion-phase porosity and introducing bed heterogeneity. The resulting increase in gas permeability allows a larger fraction of the gas flow to pass through the emulsion phase, reducing the amount of excess gas available for bubble formation and growth. Consequently, bubble size decreases, bubble stability is reduced, particle circulation weakens, and granular temperature decreases. Through this sequence of effects, particle-scale electrostatic interactions produce significant changes in macroscopic fluidized-bed hydrodynamics.

3.7 Conclusions

The influence of electrostatic interactions on fluidized-bed hydrodynamics was investigated using DPM simulations of charged and uncharged particle systems. Based on the results presented in this chapter , the following conclusions can be drawn:

1. Electrostatic interactions modify the fluidization behaviour of gas–solid beds and increase bed heterogeneity. While the uncharged bed exhibits relatively uniform fluidization, charged beds develop significant vertical variations in solids holdup and porosity.

2. Pressure-drop measurements suggest that increasing particle charge makes the transition from the fixed-bed to fluidized state less distinct. At high charge levels, local heterogeneity introduces oscillations in the pressure-drop curve, complicating determination of the minimum fluidization velocity.

3. Electrostatic repulsion increases the porosity of the emulsion phase, allowing a larger fraction of the gas flow to pass through the particulate phase. This modifies the gas distribution within the bed and reduces the amount of excess gas available for bubble growth.

4. Single-bubble simulations show that electrostatic interactions reduce bubble size, promote particle penetration into the bubble interior, and decrease bubble stability. Bubble area decreases by approximately 4% and 10% for particles carrying 0.5% and 1% of the maximum particle charge, respectively.

5. Comparison with classical bubble theory suggests that the observed bubble shrinkage results from increased emulsion-phase permeability rather than direct modification of bubble mechanics. Enhanced gas leakage through the emulsion phase provides a physical explanation for the reduced bubble sizes observed in charged beds.

6. Electrostatic interactions significantly alter particle dynamics. Particle circulation velocities decrease, additional local circulation loops appear, and granular temperature is reduced throughout much of the bed, indicating weaker particle mixing and mobility.

7. Overall, the simulations support a mechanistic picture in which electrostatic repulsion increases local bed porosity, modifies gas distribution, suppresses bubble growth, weakens solids circulation, and ultimately changes the macroscopic hydrodynamics of the fluidized bed.

CHAPTER 4

Experimental study of electrostatic charge effect on hydrodynamics of gas-solid fluidized beds

Abstract

Electrostatic charging is an inherent phenomenon in gas–solid fluidized beds containing electrically insulating particles and can significantly influence bed hydrodynamics. However, previous experimental studies have reported conflicting observations regarding its effect on fluidization behavior and bubble dynamics. This work presents a systematic experimental investigation of the influence of electrostatic charging on the hydrodynamics of Geldart B glass particles fluidized in a pseudo-two-dimensional polymethylmethacrylate (PMMA) column.

Electrostatic charges were generated by fluidizing the bed with dry nitrogen, while humidified nitrogen was used to obtain nearly uncharged conditions. Pressure-drop measurements, Faraday cup charge measurements, and high-speed imaging combined with digital image analysis were employed to quantify the effects of charging on fluidization characteristics and bubble behavior.

Electrostatic charging increased the minimum fluidization velocity by approximately 33%, while the minimum bubbling

velocity remained largely unchanged. Analysis of the pressure-drop characteristics indicates that this increase originates from an increase in bed voidage caused by electrostatic repulsion between particles, allowing the charged bed to behave as an expanded fixed bed over a wider range of gas velocities. Sectional pressure measurements further revealed that charging produces a heterogeneous voidage distribution throughout the bed, resulting in local bubble formation even below the global minimum fluidization velocity.

Single-bubble injection experiments demonstrated that electrostatic charging decreases the average visible bubble area by approximately 16%, as a larger fraction of the injected gas leaks through the more porous emulsion phase. Charged beds also exhibited increased bubble instability, reduced probability of stable bubble formation, and more frequent bubble collapse, whereas bubble shape and rise velocity were only weakly affected. Under freely bubbling conditions, however, bubble sizes were comparable for charged and uncharged beds, indicating that electrostatic effects are most pronounced near the onset of fluidization.

These results provide experimental evidence that electrostatic charging fundamentally alters fluidized-bed hydrodynamics through changes in local bed structure rather than by directly modifying bubble motion. The findings demonstrate that electrostatic effects should be explicitly incorporated into hydrodynamic models to accurately predict fluidization behavior, gas distribution, and bubble dynamics in insulating particle systems.

4.1 Introduction

Fluidized bed reactors have been in operation in industrial applications since as early as the 1920s, initially as coal gasifiers. In the 1940s, this reactor technology was further developed for the production of high-octane gasoline through Fluid Catalytic Cracking (FCC). Over time, fluidized bed reactors have become widely utilized across various industries, including hydrocracking processes, polymer production, pharmaceutical manufacturing, solids drying, and numerous other applications. Their versatility and efficiency make them indispensable tools in modern industrial processes.

A fluidized bed comprises solid particles suspended by a gas fed from the bottom of the column, which permeates the bed through the interstitial space. This amalgamation of suspended solids and interstitial gas forms what is known as the emulsion phase, exhibiting fluid-like behavior. Excess gas passes through this emulsion phase in the form of bubbles, dragging particles along in their wakes, creating macroscopic circulation patterns. Fluidized

bed reactors offer numerous advantages stemming from this unique behavior, including exceptional gas-to-solid mass transfer facilitated by intense gas-solid contacting, efficient gas-solid heat transfer, maintenance of uniform temperatures, and versatility in handling a wide range of feedstocks.(Cocco et al. 2014; Fotovat et al. 2017a; Jahnig et al. 1980; Kunii et al. 1994).

The conditions inside a fluidized bed in general cause the generation of electrostatic charges on the particles and reactor walls. This occurs due to constant collisions between particles and between particles and walls, a phenomenon known as triboelectrification—a type of contact electrification. These charges can lead to various operational issues. For instance, the effect of electrostatic charges has been observed in the form of wall sheeting in the 1940s (Cross 1987). Most effort since then has generally been put towards minimizing this effect, even though the entire extent of the phenomenon is still unknown (Mehrani et al. 2005). Apart from wall sheeting, electrostatic charges may cause particle agglomeration, channeling inside the reactor, interference with instrumentation, and even electrostatic discharge that can potentially lead to fire and explosions(Matsusaka et al. 2010). Particularly in polymer production, where low-weight particles are prevalent and more susceptible to electrostatic forces, these effects are of significant concern. They can adversely impact production quality and necessitate reactor shutdowns. Therefore, it is crucial to thoroughly understand this phenomenon and its implications for fluidized bed operation (Hendrickson 2006).

Recent studies have investigated the impact of electrostatic charges using numerical and experimental approaches. Much of this research has concentrated on understanding how hydrodynamic conditions within the bed influence the magnitude of electrostatic charge generation.

Experiments have shown that the charge generation inside fluidized beds increases with increasing superficial gas velocity. This is due to the increased inter-particle and particle-wall collisions caused by the increasing gas velocity. The effect of electrostatic charges on hydrodynamics has primarily been investigated using single bubble injection experiments and simulations, by measuring the bubble size and velocity (Jalalinejad et al. 2016; Tan et al. 2018).

Comparisons of bubbles injected in charged vs uncharged beds have indicated that electrostatic forces can affect the bubble size. However, similar experiments have led to contradicting results in the literature. The study by Jalalinejad et al. (2016) predicted a significant increase in bubble size with rising average charge density of the particles, whereas Tan et al. (2018)'s study suggested a reduction in bubble size. Both experiments utilized a Faraday cup method to measure the overall bed charge, and employed a plexiglass column with glass particles. The one apparent difference between these two works was the particle sizes used, potentially impacting the final outcomes.

The minimum fluidization velocity, or U_{mf}, is a key parameter used to characterize the behavior of fluidized beds; the parameter is crucial in many

correlations, such as those describing the bubble size and rise velocity, rates of mass and heat transfer, and to predict the circulation and mixing rates. The effect of electrostatic charges on U_{mf} has also been investigated; in experiments it was found that the minimum fluidization velocity increases as a result of charged particles (Dong et al. 2015). This effect has also been shown by other experiments, which found a decrease in bubble size for charged particles (Alsmari et al. 2015; Kezeng et al. 2015; Mehrani et al. 2005). Using the bubble size correlation of (Mori et al. 1975), an increase in minimum fluidization velocity was predicted (Dong et al. 2015).

The objective of this study is to assess and quantify the impact of electrostatic charges on the hydrodynamic behavior within a fluidized bed through experimental investigation. To achieve this goal, an experimental setup is designed to investigate the hydrodynamics of a fluidized bed both with and without electrostatic charges. The generation of charges in the bed is investigated using an electrometer. The influence of these charges on the minimum fluidization and bubbling velocity is measured. Single bubble injections are conducted and analyzed using digital image analysis (DIA), enabling the examination of bubble size, shape and velocity from (high-speed) image recordings.

This paper is organized as follows; in the following section, we will detail the experimental setup and procedures. Thereafter, we outline the findings, in particular how electrostatic charges affect the minimum fluidization velocity, single rising bubble behavior, and on the minimum bubbling velocity. Moreover, we study the freely bubbling behavior for charged and uncharged situations. In the conclusions we wrap up with the general observations that should be accounted for when studying electrostatics in fluidized beds.

4.2 Experimental Methods and Materials

Experimental Setup

The experimental setup consists of a pseudo two-dimensional fluidized bed, with dimensions of 1000 mm in height, 202 mm in width, and 11 mm in depth. Only a small part of the height is actually filled with particles, while the remainder of the column acts as a defluidization zone. The column is made of polymethylmethacrylate (PMMA) and contains a stainless steel 316, sintered, porous plate with the average pore size of 40 µm, serving as a gas distributor. The distributor is located on top of a windbox, to which the gas inlet is connected, with dimensions of 35 mm in height, 208 mm in width, and 40 mm in depth. The fluidizing gas was nitrogen, which was fed with a pressure of 1 bar to the distributor. The gas flow rate was regulated with a control valve which allowed for a maximum flow rate of up to 120 $\mathrm{Nl\,min^{-1}}$, the gas feed could be stopped with a shut-off valve. The gas line for bubble

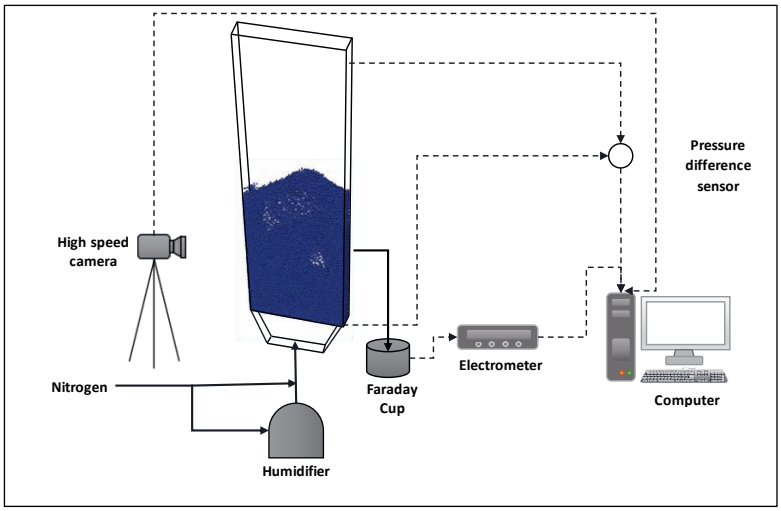
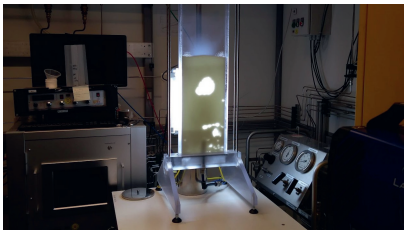


Figure 4.1: Experimental set-up schematics.

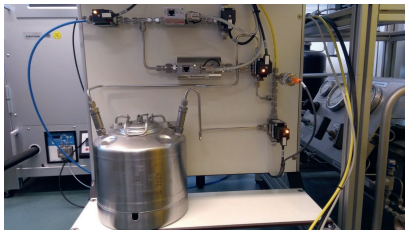
injection is controlled separately; this line allows for a maximum gas flow rate of 30 $\mathrm{Nl\,min^{-1}}$, and is connected to a 1 cm diameter hole located in the center of the distributor. The gas can optionally be passed through a humidifier before entering the distributor, in case the bed needs to be kept at uncharged state. This humidifier comprises a vessel filled with demineralized water. The experimental setup is depicted in Figures 4.1 and 4.2, illustrating the column, the humidifier, the Faraday cup, and the high-speed camera utilized for the experiments.

Since the column is made of transparent PMMA, it offers the possibility to see and record the hydrodynamic behavior of the bed. For this purpose a high-speed camera was set-up in front of the column. A LaVision HS4M camera was used, equipped with a Nikon 55 mm lens. To clearly distinguish between the emulsion phase and bubbles a bright LED light was located directly behind the column. The obtained recordings were processed using a digital image analysis (DIA) script, which was programmed in MATLAB, as outlined in the next section.

The bed material consists of glass particles with a mean diameter of 475.9 µm with a standard deviation of 22.3 µm, which are classified as Geldart B-type particles. Sieved particles with a size distribution bound by 420 and 500 µm were used for the experiments. This distribution was obtained by taking high-resolution images using a Nikon DLSR camera with a 200 mm lens and analyzing the radii distance in pixels using MATLAB. The particles were obtained by sieving particles with a size distribution



(a) Fluidized bed in operation.



(b) Humidifier and control valves.



(c) Faraday cup underneath sampling valve.



(d) LaVision HS4M high-speed camera.

Figure 4.2: Experimental set-up parts overview.

between 400 and 600 µm, the fraction between 420 and 500 µm was used for the experiments.

Digital image analysis

To examine the bubble rise behavior, high-speed image recordings of bubbles injected into the fluidized bed were captured. These recordings, obtained in grayscale at speeds of up to 240 frames per second, were acquired using the LaVision HS4M high-speed camera (see Figure 4.2d). Subsequently, the recordings were imported as numerical arrays into a digital image analysis (DIA) script developed in MATLAB 2020b.

The grayscale pixel intensity values in the arrays were normalized using bounds measured separately; the upper bound corresponded to an empty bed (i.e. no particles were obstructing the view of the light source behind the column), and the lower bound corresponded to a fixed bed, where the maximum amount of solids blocked the view of the light source. If values exceeded the upper or lower bound they were capped to the threshold they exceeded. This process results in a normalized pixel intensity constrained between 0 and 1.

Subsequently, the values were inverted such that empty column values correspond to 0 and the fixed bed corresponds to 1. This was required for the next step, where these normalized pixel intensity values are converted to three-dimensional solids porosity values. For this conversion,

a correlation was developed by De Jong et al. (2012), by creating artificial photorealistic 2D images using Discrete Particle Model (DPM) simulation results; their simulation produced frames with an exactly known solids porosity distribution, and the artificial images made it possible to construct an intensity-3D porosity conversion correlation for a pseudo-2D bed - the bed was deep enough to fit multiple particles but bubbles would still be visible. The correlation is shown in equation 4.1.

$$\varepsilon_{s,3D} = \begin{cases} \varepsilon_{s,3D,max} & \text{for } \varepsilon_{s,3D} \geq \varepsilon_{s,3D,max} \\ \dfrac{A \cdot \varepsilon_{s,2D}}{1 - \dfrac{1}{B}\varepsilon_{s,2D}} & \text{for } \varepsilon_{s,3D} < \varepsilon_{s,3D,max} \end{cases} \tag{4.1}$$

Here, A and B are fitting parameters, which were determined as 0.021 and 0.882 respectively, $\varepsilon_{s,3D,max}$ is the maximum 3D solids fraction threshold, set to 0.64, and $\varepsilon_{s,2D}$ is the 2D solids fraction that could be related to the normalized pixel intensity.

Using these settings, the weight in case of a fixed-bed can be calculated from an image taken at zero flow conditions, which resulted in about 1.4 kg, approximately the same weight of the particles in the bed. A graph of Equation 4.1 is shown in Figure 4.3. The dashed line denotes the threshold for the bubble phase, while the colored area beneath the curve signifies all normalized pixel intensity values falling below this threshold, hence constituting part of the bubble phase. Consequently, any pixel intensity below 0.785 was categorized as being part of the bubble phase (De Jong et al. 2012).

Next, the image is converted to a binary image, explicitly separating the two phases. Here, a threshold of 0.15 is used, as indicated in Figure 4.3. All porosity values equal or less than 0.15 were converted to 1 (representing the bubble) and all bigger values were converted to 0 (representing the emulsion phase). Consequently, the bubble area, diameter, center-of-mass, sphericity and aspect-ratio are calculated and converted from pixel units to SI units by using the width of the column as a scaling factor. The bubble rise velocity was also obtained by using the center-of-mass coordinates of the bubble and the time between each frame of the recording, which was obtained by taking the inverse of the frame rate.

An example of the different stages of the DIA script is shown in Figure 4.4. Figure 4.4A shows the normalized pixel intensity values of the image, which are between 0 and 1. Figure 4.4B shows the solid porosity values, which are between 0 and 0.64. Figure 4.4C shows the binary image, in which the bubble area is shown in white with a red contour. The red dot represents the center-of-mass of the bubble. Finally, Figure 4.4D shows the overlay of the detected bubble on the original image.

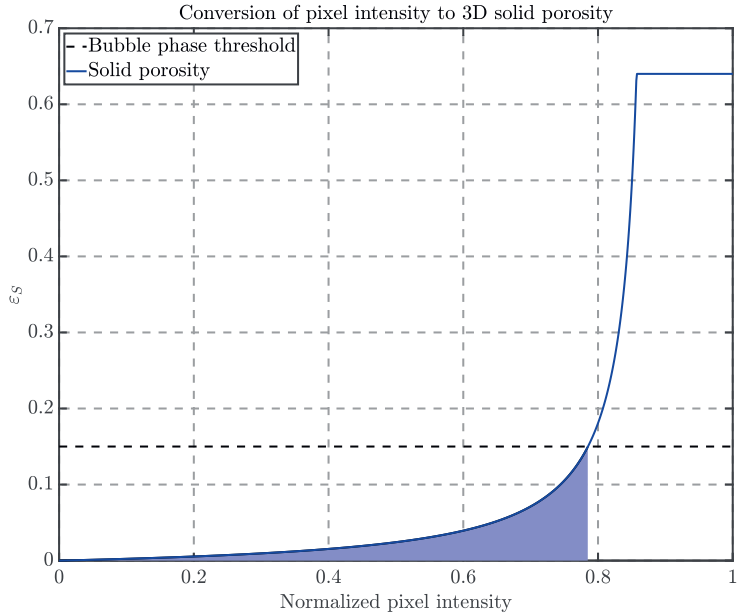


Figure 4.3: Correlation between the normalized pixel intensity and the 3D solids porosity.

Table 4.1: Camera and software settings.

Operation	Exposure [µs]	Frequency [Hz]	ROI	Aperture
Bubble injection	3999	240	[533,1464,1,2016]	f/8
Freely bubbling	3999	30	[533,1464,1,2016]	f/8

The software and camera settings used during the experiments are shown in Table 4.1. The aperture was set to f/8 and the exposure, frequency and region of interest (ROI) were set in the camera software (pco.camware), which was used to control the high-speed camera through tethering. The focus of the lens was adjusted manually to focus on the column, using the live preview setting in the software. The only difference between bubble injection recordings and freely bubbling bed recordings is the frame rate. A much lower frame rate was used in case of the freely bubbling bed, to record for longer times without generating extremely large files.

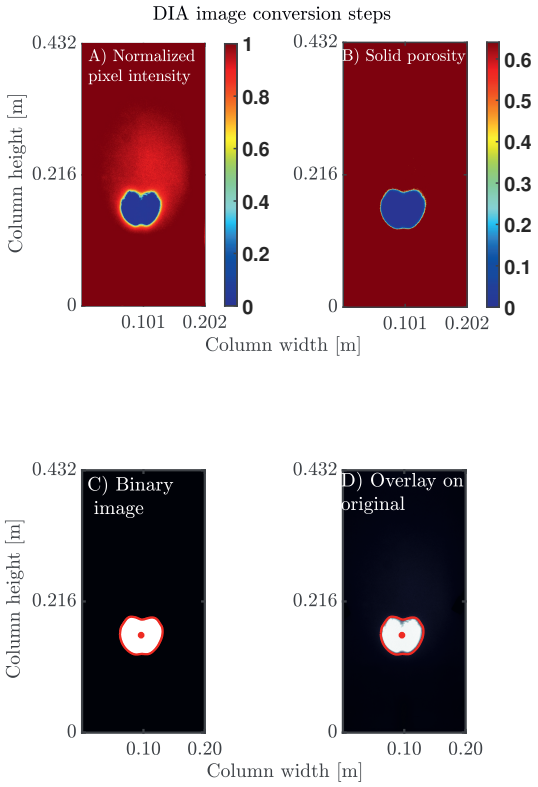


Figure 4.4: Example of the image conversions in the DIA script. A shows the normalized pixel intensity. B shows the solid porosity. C shows the binary image and D shows the bubble overlay on the original image.

Validation of Faraday cup

The charge density of the solids samples was measured using a Faraday cup. A verification procedure has been conducted to make sure that the results are (i) reproducible and (ii) provide an accurate measure for the absolute charge inside the cup.

Optimally, the verification would be done by measuring a sample of the particles used in our experiments repeatedly, however, performing this measurement will change the charge density due to particle handling and contact with the inner cup. Instead, a piece of copper, suspended by a Nylon string, has been used to perform a reproducibility test. This test was heavily inspired by the experiment done by Michael Faraday himself, who was using a brass ball suspended by a silk thread for the same purpose.

The Faraday cup measures the charge when the object is almost

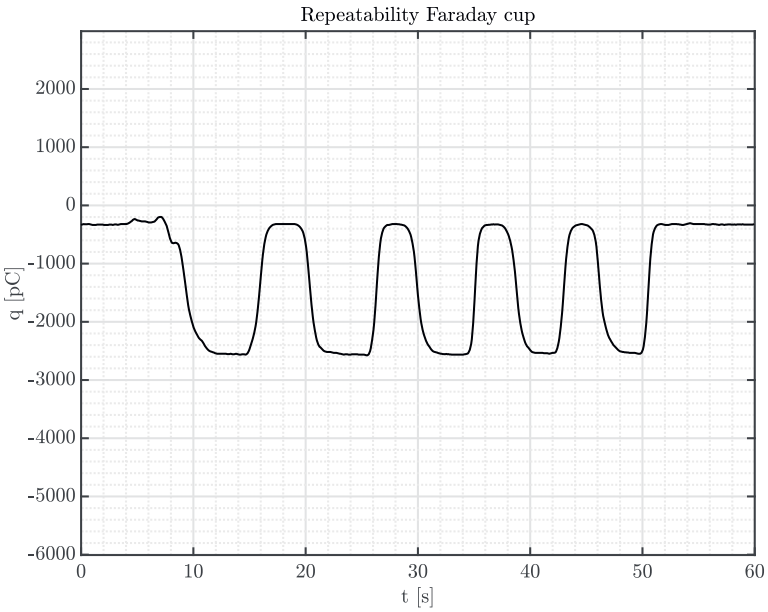


Figure 4.5: Consecutive measurements of a charged copper object suspended by a non-conductive Nylon thread moving into and out of the Faraday cup five times consecutively .

completely surrounded by the inner cup. Since the copper piece will not be in contact with any other conducting materials, or the inner cup itself, the charge on the object should not change significantly within the time-span of the experiment.

The copper object was lowered into the inner cup until it completely surrounded the object, and then elevated again for a total of five times. The results are shown in Figure 4.5.

The average charge of the measurement piece was roughly 2300 pC, with a deviation of 17.4 pC between the measurements. This deviation was deemed negligible with respect to the measuring range and therefore it was concluded that the Faraday cup allows for reproducible measurements.

A measuring range of 3000±0.5 pC was used during this experiment, which allows for a reproducibility of 1.5 pC of the electrometer. Nonetheless, the results show that using this method the Faraday cup is able to differentiate between positively and negatively charged objects consistently.

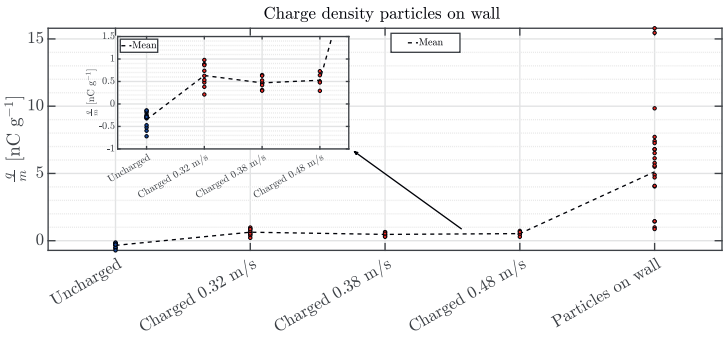


Figure 4.6: Results of multiple charge density measurements at different operating conditions.

4.3 Results & Discussion

This section begins with a discussion of the results pertaining to charge generation, followed by an examination of its impact on minimum fluidization and bubbling velocity. Subsequently, the outcomes obtained through the digital image analysis script are deliberated upon, commencing with the analysis of single bubble injection experiments and proceeding to the exploration of freely bubbling bed experiments. Finally, several general observations are summarized and discussed.

Charge generation

In this section, we will assess how the charge generation is influenced by different superficial gas velocities. The bed was filled to around 40 cm in the column, and subsequently, the bed was fluidized using dry nitrogen for 30 minutes at particular gas flow rates of 0.32, 0.38 and 0.48 $\mathrm{m\,s^{-1}}$, which roughly corresponds to a $U_g/U_{\mathrm{mf}} \approx 1.71$, 2.15 and 2.71. This procedure fluidizes the bed, and charges are generated on the particle surfaces.

The charge density was measured for the different superficial velocities used; the bed was transferred by opening the solids valve at the bottom, and the particles flow into the Faraday cup, which measures the average charge density. As the location of the particle drain is placed slightly above the porous plate, and because some particles stuck to the walls, not all particles could be transferred to the Faraday cup. The total deficit amounts up to about 10% of the total bed.

Generally the charge density was found to be positive. The particles adhering to the wall and the free particles inside the system (bulk) were collected separately to get a best possible estimate on how the charges are distributed throughout the system. The results of multiple experiments are shown in Figure 4.6.

It was shown in some studies that the charge density depends on the superficial gas velocity. (Jalalinejad et al. 2016; Manafi et al. 2019; Tan et al. 2018) all reported an increase in the charge density for increasing gas velocities (with similar increments of U_{mf}). However, the results in Figure 4.6 show more or less the same charge density for all investigated velocities. The charge density seems to plateau around +0.5 nC/g as 'bulk' charge density (as opposed to 'wall particles' charge density outlined further on).

The amount of generated charge due to the triboelectric effect seems to be around +1 nC/g on average, including both the bulk and wall sticking particles. The fact that the charges are positive can be hypothesized based on the triboelectric series tables. After the bulk of the bed was removed for the initial charge measurement, to measure the particles stuck on the wall, they were carefully extracted by tapping on the wall or using pressurized air to blow them off, when the bulk of the bed was already removed from the column.

By far the highest charge densities have been found for particles that were stuck on the column walls. The measured charge density of these particles is also shown Figure 4.6. Clearly, the magnitude of the charge density is much higher for the particles stuck on the wall, on average a factor 10 times bigger. The difference is likely even bigger, since due to the position of the sampling valve, it was impossible to prevent any 'bulk' particles from ending up in the Faraday cup.

Additionally, we note that it was not feasible to remove all the particles from the column walls. As mentioned, tapping the column walls and applying pressurized air were used to get as much particles from the walls. The latter method being more effective, but might also introduce additional particle-wall interactions which affect the measurement. The particles that remained on the walls, despite the efforts of removing them, most likely had the highest charge, since this results in the strongest electrostatic force between the particle and wall.

Particles forming sheets on the walls were reported in other experimental studies, but their increased charge density with respect to the bulk was not quantified . The relatively large scatter observed can be explained by the fact that the wall-stuck particles are only limited in number (and not all of them can be removed without the risk of changing their charge). Moreover, these particles act as a shielding layer, protecting the bulk of the particles in the bed from further particle-wall interactions hence avoiding further charge transfer to the bulk particles. This would explain why the average charge density seems to be limited to about 0.5 $\mathrm{nC\,g^{-1}}$, even though the maximum calculated theoretical charge density is around 133 $\mathrm{nC\,g^{-1}}$ (Jiang et al. 1994).

Minimum fluidization velocity

The minimum fluidization velocity is an important parameter for the characterization of the hydrodynamics in fluidized beds; countless correlations on heat and mass transfer, bubble behavior and solids mixing depend on a correct value for U_{mf}, hence its correct calculation is crucial for accurate phenomenological modelling.

U_{mf} can be obtained by observing the evolution of the pressure drop across the bed, for increasing and decreasing gas velocity. Before fluidization starts, the particles behave as a fixed bed, and therefore the pressure drop scales with the velocity according to the Ergun equation (Eq. 4.2) (Ergun 1952).

$$\frac{\Delta p}{L} = \frac{150\mu_g}{d_p^2}\frac{(1-\epsilon_g)^2}{\epsilon_g^3}U_g + \frac{1.75\rho_g}{d_p}\frac{(1-\varepsilon_g)}{\epsilon_g^3}U_g^2 \tag{4.2}$$

Here, Δp, μ_g, L, d_p, ϵ_g, U_g, and ρ_g indicate the pressure drop, fluid dynamic viscosity, characteristic length, particle diameter, bed voidage, superficial gas velocity, and fluid density respectively. When the gas velocity surpasses the minimum fluidization velocity, the time-averaged pressure drop across the bed becomes stable (plateaus), as it becomes solely dependent on the weight of the suspended bed (Eq. 4.3). Beyond the minimum fluidization velocity, the pressure drop fluctuates due to bubbles forming and erupting, but the pressure drop is constant under pseudo-steady-state assumption.

$$\Delta p_{bed} = H_{bed}\, g\, (\rho_p(1-\epsilon_g) - \rho_g) = H_{bed}\, g\, \rho_{bulk} \tag{4.3}$$

Here, Δp_{bed}, H_{bed}, g, ϵ_g, ρ_p, ρ_g, and ρ_{bulk} refer to the pressure drop over the bed, the height of the bed, the gravitational acceleration constant, the bed voidage, the solid density, the gas density, and the bulk density respectively. Consequently, with increasing gas velocity the pressure drop across the bed will initially increase, until it reaches the pressure drop of the maximally expanded bed, which is at minimum fluidization velocity.

The minimum fluidization velocity can be obtained by measuring the pressure drop over a range of gas velocities. The gas velocity at which the pressure drop no longer increases is the minimum fluidization velocity. The typical procedure to find this point, is to increase the gas velocity from zero, up to and beyond the U_{mf} point, and then decrease the gas velocity back to zero. The intersection of the two linear interpolants (of the expanding bed regime and the constant pressure drop regime) indicates the U_{mf} point. The decreasing of the gas velocity is a practical aspect that helps to mitigate hysteretic effects of the bed expansion (Kunii et al. 1994).

The minimum fluidization velocity of a bed of charged particles was investigated using dry nitrogen gas. The bed was fluidized beforehand to charge the particles at $2U_{\mathrm{mf}}$ for 60 min that build up the charge to 1nC/g on average. Again, a bed height of 42 cm was used and the gas velocity decreased with 1 $\mathrm{L\,min^{-1}}$ and was held constant for 10 min. A similar procedure (but without the charge build-up step) was done using humidified nitrogen, in order to also determine the U_{mf} for an uncharged bed.

Figure 4.7 shows the pressure drop across the bed as a function of the superficial gas velocity for both cases. For the uncharged bed, U_{mf} was determined to be 0.191 $\mathrm{m\,s^{-1}}$, measuring a pressure drop across the bed of 0.056 bar. The charged bed showed a U_{mf} of 0.254 $\mathrm{m\,s^{-1}}$, exceeding the uncharged U_{mf} with roughly 33%. The bed pressure drop stayed the same, within measurement uncertainty. The observed increase of U_{mf} with electrostatic charges is in accordance with results of Manafi et al. (2019), which showed also an increase in U_{mf} for charged particles.

One noticeable aspect of Figure 4.7 is the negative slopes at gas velocities above U_{mf}. This phenomenon initially arose due to a slight protrusion of the column in the depth (viewing) direction at higher flow rates. This is due to very slightly expanding, PMMA walls, being unable to withstand the weight of the bed under fluidization conditions, in spite of adding another 8 mm plexiglass reinforcement layer in addition to the original 3 mm-thick PMMA walls. The bed would collapse as bubbles formed and rose, exerting significant additional force on the walls compared to a static bed. While these thin walls were initially chosen to accommodate electrostatic induction sensors, these measurements were not conducted for this study. The protrusion was largely mitigated by affixing stiff plates on the front and back walls of the column. However, complete elimination of this expansion in the plexiglass bed could not be achieved.

When using charged particles, the formation of bubbles becomes significantly more pronounced, as evident from the pressure drop curves. The error bars, representing the standard deviation of the pressure drop during the sampling period (10 min), exhibit a greater magnitude for higher velocities, indicating substantially larger pressure fluctuations. This phenomenon arises from the formation and subsequent collapse of bubbles, which occur after surpassing the minimum fluidization velocity.

It is clearly seen that initially the slope of the pressure curve for the charged bed is much lower than that of the uncharged bed. According to Equation 4.3, the bed voidage should be roughly 0.43 to yield this bed pressure drop. This voidage is on the high side but not implausible. In the velocity range of 0–U_{mf} the pressure drop curves follow the Ergun equation (Eq. 4.2). Since the eventual pressure drop doesn't change, but U_{mf} does, the slope of the initial part has to change. This is clearly visible in Figure 4.7. The slope of the uncharged bed is equal to 0.721 $\mathrm{bar\,s\,m^{-2}}$ and for the charged bed it is 0.545 $\mathrm{bar\,s\,m^{-2}}$, this gives a ratio of roughly 1.32. This change in ratio can be correlated to the Ergun equation. Since the gas viscosity and density are hardly influenced by the humidity at 20 °C they can be regarded as constant, and since the particle diameter also remains constant this only leaves the bed voidage as a possible explanation for this reduction in slope.(Tsilingiris 2008)

Equation 4.4 shows the equation that has to be solved to obtain the ratio in bed voidage to explain the difference in slope for the pressure drop curves. The ratio between the slopes is 1.32.

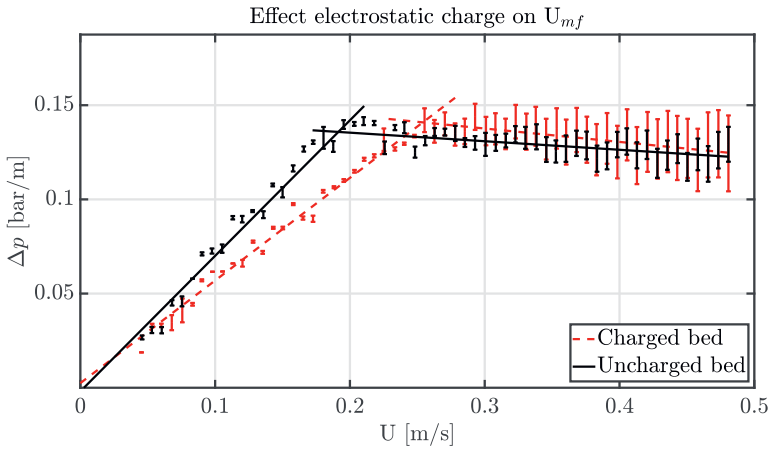


Figure 4.7: Comparison of minimum fluidization velocity in case of using humidified nitrogen gas (less/no charged particles) and dry nitrogen gas (charged particles).

$$\frac{(\frac{\Delta p}{L})^1}{(\frac{\Delta p}{L})^2} = \frac{f_1}{f_2} = \frac{(\frac{150\mu}{d_p^2}\frac{(1-\epsilon_g)^2}{\epsilon_g^3}U_g + \frac{1.75\rho}{d_p}\frac{(1-\epsilon_g)}{\epsilon_g^3}U_g^2)^1}{(\frac{150\mu}{d_p^2}\frac{(1-\epsilon_g)^2}{\epsilon_g^3}U_g + \frac{1.75\rho}{d_p}\frac{(1-\epsilon_g)}{\epsilon_g^3}U_g^2)^2} \approx 1.32 \tag{4.4}$$

For a bed voidage of 0.43 in case of the uncharged bed, a bed voidage of 0.45 would be estimated for the charged bed to get this ratio between the pressure curve slopes according to the Ergun equation. Since the bed voidage for the uncharged bed could be different, the result has been plotted over a wide range of bed voidage and for different velocities within the fixed-bed regime, this result is shown in Figure 4.8. It clearly shows that this difference can only be explained if the bed voidage is higher in case of the charged bed (which corresponds to a lower solid holdup as shown in the Fig. 4.8). This increased voidage could be explained by the repulsive force between the particles, which was also observed for the particles stuck on the column walls. Since the particles repel each other, more free space is created, resulting in a higher bed voidage.

Moreover, the increase in bed voidage should theoretically result in a higher bed height for the charged bed, which was also investigated. Initially, the bed height measured 40.1 cm at minimum fluidization with an uncharged bed. Considering the difference in bed voidage, this should theoretically lead to a bed height increase to 42.1 cm. However, multiple measurements yielded an average bed height of 41.3 cm with a deviation of 0.2 cm over four different measurements. Thus, there was an increase of approximately 1.2 cm, instead of the expected theoretical increase of 2.0 cm. This deviation could partly be explained by particles adhering to the wall, which occurs

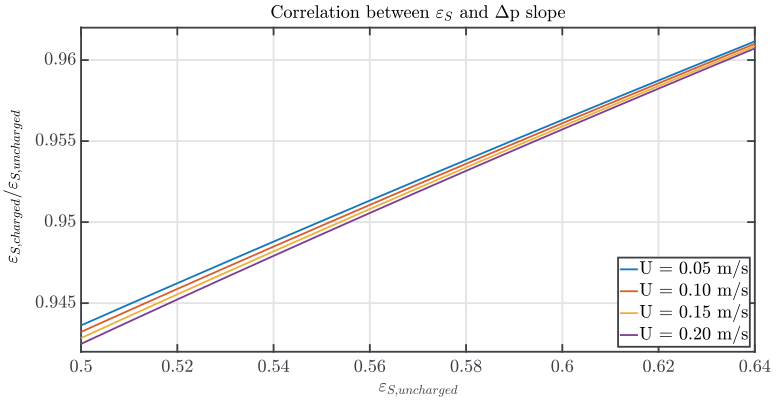


Figure 4.8: The difference in solid holdup between a charged and uncharged bed required to explain the difference in pressure drop slope during the fixed-bed state.

only when the bed is charged. Roughly 24 g of glass particles would need to be stuck on the wall to account for the 0.8 cm difference from the theoretical height. The images of the bed height clearly show the particles adhering to the walls. This increased bed height further confirms the increased bed voidage in the case of charged glass particles.

Minimum bubbling velocity

Apart from the minimum fluidization velocity, also the minimum bubbling velocity (U_{mb}) has been investigated, which is defined as the velocity at which bubbles start to form. For Geldart B particles, this is usually right after U_{mf} has been surpassed. Some snapshots of the uncharged bed at different gas velocities are shown in Figure 4.9. It clearly shows the expected behavior for Geldart B type particles, with no bubble formation at U_{mf} (Fig. 4.9.A) and clear bubbles forming already at 1.1 U_{mf} (Fig. 4.9.C). Even at 1.05 U_{mf} (Fig. 4.9.B) small bubbles already start to form at certain areas in the bed.

The same was done for a charged bed. Note that in this case U_{mf} increases, as was shown in the other results. Since U_{mf} tends to vary a bit between the measurements the average value was used, which was determined at 0.254 $\mathrm{m\,s^{-1}}$. Figure 4.10 shows snapshots of the bed at different gas velocities in case of a charged bed.

It is clear that bubbles in the charged bed, at the same u/U_{mf} ratios, are much more prevalent when compared to the uncharged bed when the gas velocity exceeds U_{mf}. Additionally, it was observed that some bubbles would form and rise from the middle and upper region of the bed, even when the

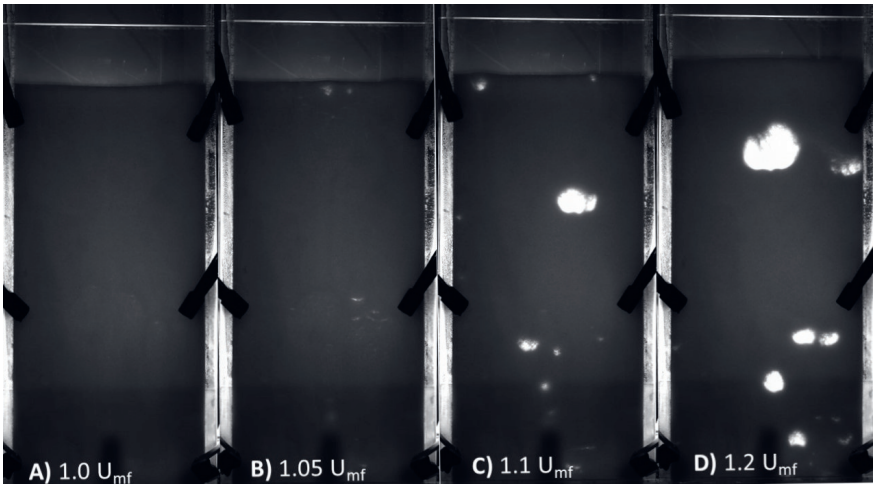


Figure 4.9: Investigation of U_{mb} for an uncharged bed. Bubble formation shown at different superficial velocities, A) shows 1.0 U_{mf} B) shows 1.05 U_{mf} C) shows 1.1 U_{mf} and D) shows 1.2 U_{mf}

gas velocity was still below U_{mf}. Bubbles would also appear in the lower region of the bed, but these do not rise to the top of the bed completely, but instead deflate into the interstitial space somewhat higher in the bed. These results suggest a degree of heterogeneity of the bed voidage for charged beds, playing a significant role in the bubble dynamics; apparently the excess gas flow rate changes along the column height, having implications on the bubble diameter, use velocity and bubble growth relations.

By measuring the pressure drop over different height sections in the bed we were able to determine the porosity profile in the bed. In Figure 4.11, the sectional pressure shows a decreasing trend as a function of the height.

These results demonstrate that at gas velocities just below U_{mf}, the top of the bed already achieves the fully expanded, fluidized state, whereas the lower areas of the bed are more densely packed. Bubbles that form in the lower regions can therefore more easily deflate into the more open structure higher in the bed. We believe that this is caused by the hydrostatic pressure of the bed, which increases towards the bottom of the bed, and herewith (partly) overcomes the repulsive action of the electrostatic charges. This, in turn, will affect the pressure drop and therefore the measurement of U_{mf} and explain the variability of U_{mf} in the charged beds in the first place.

The gas velocity could be reduced to 0.9 U_{mf}, and still bubbles occasionally formed in the upper part of the bed. Since this concerns only a small area of the bed, these occurrences cannot be considered as the overall onset of bubbling; these bubbles have appeared due to the heterogeneity of the bed. This observation suggests that the definitions of U_{mf} and U_{mb} may need to be reconsidered or adjusted to accommodate such variability.

[!t]

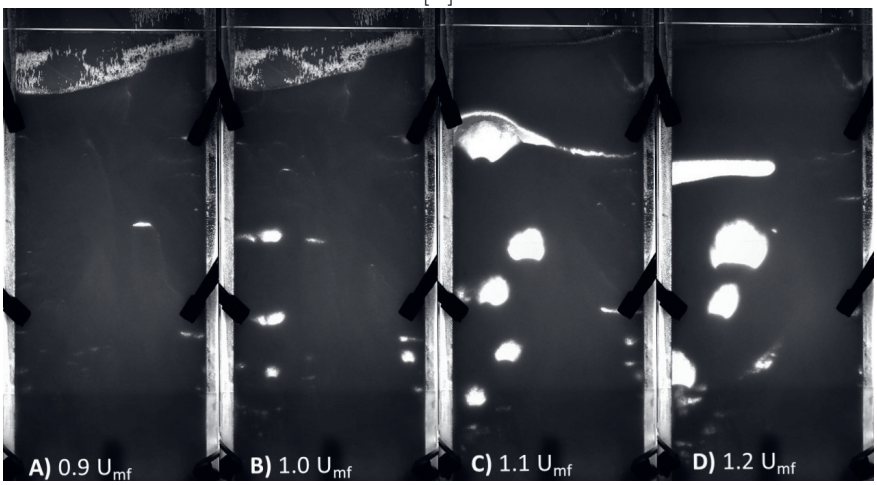


Figure 4.10: Investigation of U_{mb} for a charged bed. Bubble formation shown at different superficial velocities, A) shows 0.9 U_{mf}, B) shows 1.0 U_{mf}, C) shows 1.1 U_{mf} and D) shows 1.2 U_{mf}.

[!t]

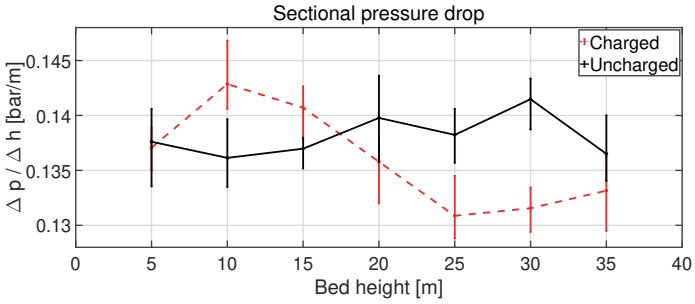


Figure 4.11: Sectional pressure drop for uncharged (black) and charged (red) bed.

Single bubble injections

Bubble phenomena play an important role in gas-solid contact and solids circulation, therefore it is an important (hydrodynamic) property to investigate. Injection of single bubbles in the fluidized bed was investigated using high-speed recordings and analyzed using digital image analysis (DIA) (Laverman et al. 2008). Accordingly, 30 bubbles were recorded during their rise trajectory, using a high-speed camera. The orifice used for bubble injection has a diameter of 1 cm, therefore with a flow rate of 15 L min^{-1} the injection velocity equals 3.18 m s^{-1}.

For conducting experiments in an uncharged bed, humidified gas was used to generate the minimum fluidization state. The bed was also charged

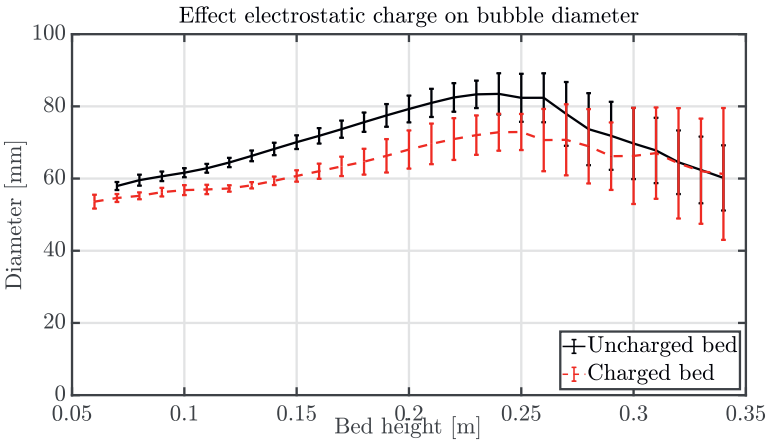


Figure 4.12: Average bubble diameter in the uncharged bed (black) and charged bed (red) as function of the height in the bed.

by first fluidizing the bed at 2 U_{mf} for an hour, before recording any bubble injections.

At these conditions, 30 bubble injections were performed using an injection volume of 50.0 mL, and their results were averaged over increments in height of 1 cm. The bubble diameter, area, aspect-ratio and velocity were obtained. The average bubble diameter, in case of uncharged and charged particles is shown in Figure 4.12. When multiple bubbles would be detected, the largest bubble in-frame was tracked to determine the bubble diameter over the vertical position. This explains why the error bars are much smaller in the lower part of the bed, since near the top of the bed the bubbles tend to become unstable and break up. Nonetheless, the results show that, on average, the bubbles in an uncharged bed are slightly bigger, when the same injection volume of gas is used.

Figure 4.13 shows the total visible bubble area in case of an uncharged and a charged bed. This total area also includes bubbles that are split, which explains why the error bars are much smaller compared to the bubble diameter. Again, it shows clearly that the bubbles are larger in case of an uncharged bed. This can be explained by the increased bed voidage for the charged bed, that was found for the previous results. More gas leaks to the emulsion phase, due to the increased bed voidage caused by the repulsive forces between particles in a charged bed. Therefore, less gas travels as bubbles through the bed which results in smaller bubbles. On average, the bubble area in an uncharged bed is 3575 mm^2 and 2848 mm^2 for a charged bed. The bubble volume can be calculated with the depth of the bed, which is 11 mm. This results in an average bubble volume of 39.3 mL and 31.3 mL for an uncharged and a charged bed respectively. Since the injection volume is equal to 50.0 mL, on average 78.7% of the injected volume travels as a

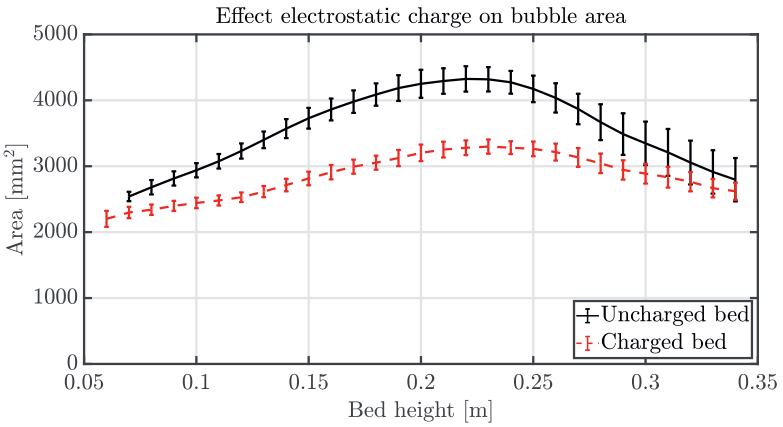


Figure 4.13: Average bubble area in the uncharged bed (black) and charged bed (red) as function of the bubble height in the bed.

bubble for an uncharged bed and 62.7% in case of a charged bed. As a result, in case of a charged bed the average bubble size decreases with 16.0%, due to greater leakage of gas to the emulsion phase caused by the increased bed voidage.The observed reduction in bubble size is consistent with the experimental findings of Jalalinejad et al. (2016), who reported that bubbles in highly charged beds were approximately 15% smaller than those in less charged beds. Their results were likewise attributed to modifications of the gas-solid hydrodynamics caused by electrostatic effects. However, this trend differs from the observations of Tan et al. (2018), who reported an increase in bubble area with increasing charge density. These conflicting observations suggest that the influence of electrostatics on bubble size may depend strongly on factors such as charge distribution, particle properties, and bed operating conditions.

Next, the influence of electrostatic charge on the shape of the bubble was analyzed; this feature is of particular importance for the solids mixing process, which is driven mainly by the particles travelling in the wake of the bubbles (Mehrani et al. 2017). If the bubble shape changes, so does the solids mixing intensity. The most common attribute is the bubble aspect-ratio, which was determined by dividing the bubble width over the bubble height (Kunii et al. 1991). Figure 4.14 shows the average aspect-ratio along the vertical position. In the bottom part of the bed, the bubbles have a very similar aspect-ratio, slightly above one. The bubbles tend to get wider in both cases as they rise through the bed. On average the aspect-ratio of a bubble in an uncharged bed was 1.65, while it was slightly wider (1.84) in a charged bed. However, the error bars also indicate that the results vary a lot more in the charged bed. This might be due to the heterogeneity of the bed porosity. Overall, the shape of the bubbles does not seem to be strongly influenced by the bed charge. This observation differs from the CFD

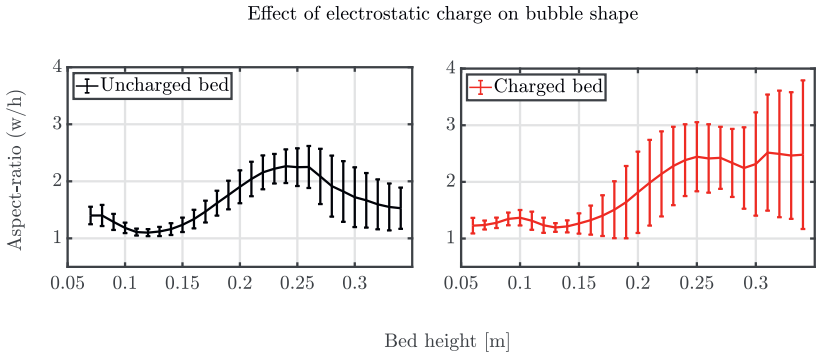


Figure 4.14: Average bubble aspect-ratio (bubble width over bubble height) for an uncharged bed (black) and charged bed (red).

predictions of Jalalinejad et al. (2012), who reported substantial bubble elongation in the direction of bubble motion as particle charge increased. In subsequent experiments, Jalalinejad et al. (2016) observed approximately 15% larger bubble height-to-width ratios in highly charged beds. In contrast, Tan et al. (2018) found that bubbles became progressively flatter as charge density increased. The present results indicate that, although electrostatic charging clearly affects bubble size and stability, its influence on the mean bubble aspect ratio is comparatively modest under the conditions studied here. Figure 4.15 and 4.16 show examples of bubble paths for the uncharged and charged case respectively. It was observed that the general shape of the bubble does not change drastically. It only shows that the bubbles are slightly smaller in case of a charged bed.

The results visualised are representing stable bubbles, that managed to reach the top of the bed. However, injections would often not lead to any bubble at all, or it would quickly burst and disappear in the bed after injection, in particular when the bed was charged. Similar results were observed in other experimental studies (Jalalinejad et al. 2016). The observed heterogeneity of the bed in combination with the increased bed voidage may cause this. Since gas is more likely to pass through the emulsion phase, forming a stable bubble is more challenging; any correlations describing the formation of bubbles should include this bifurcation as it would influence the total number of bubbles. The lower the injection volume, the stronger this effect was observed. Bubble injections into an uncharged bed never resulted in unstable bubbles, and even extremely modest injection volumes formed stable bubbles. While increased bubble instability has previously been reported for charged beds by Jalalinejad et al. (2016) and Tan et al. (2018), the present experiments additionally demonstrate that electrostatic charging strongly affects the probability of successful bubble formation itself.

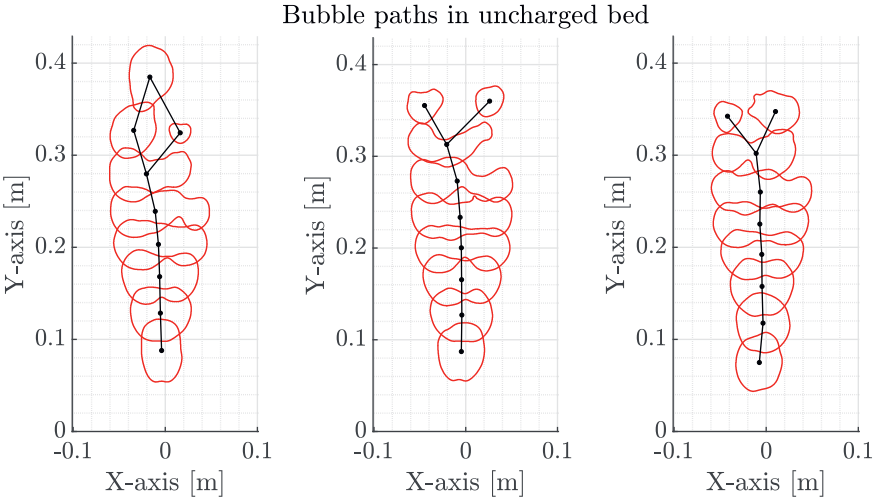


Figure 4.15: Paths of bubbles in an uncharged bed with an injection volume of 50.0 mL.

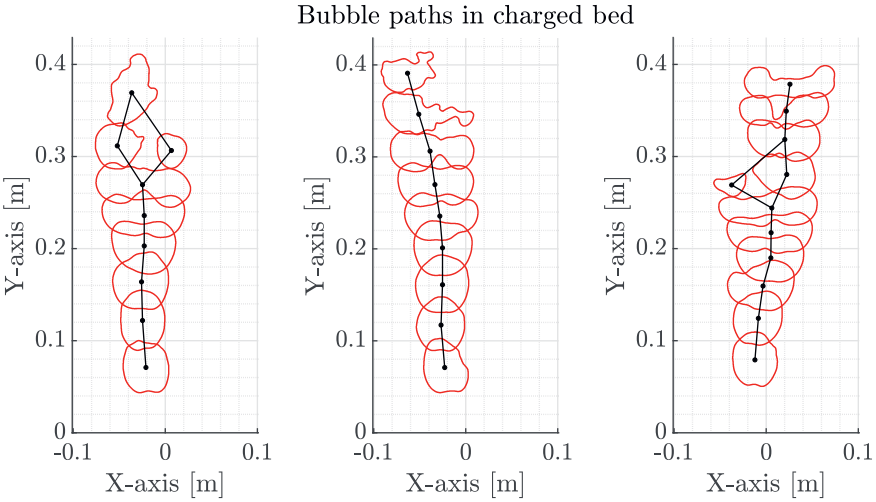


Figure 4.16: Paths of bubbles in a charged bed with an injection volume of 50.0 mL.

To the authors' knowledge, this reduction in the likelihood of generating a stable injected bubble has not been explicitly quantified in previous studies.

The break-up of these initially stable bubbles was also studied. Figure 4.17 shows the percentage of bubbles that are split over the height of the bed. The percentage is taken of the 30 recorded bubbles. The data demonstrate that the chance of bubble splitting increases near the top of the bed in both situations. Once a stable bubble has developed, there does not appear

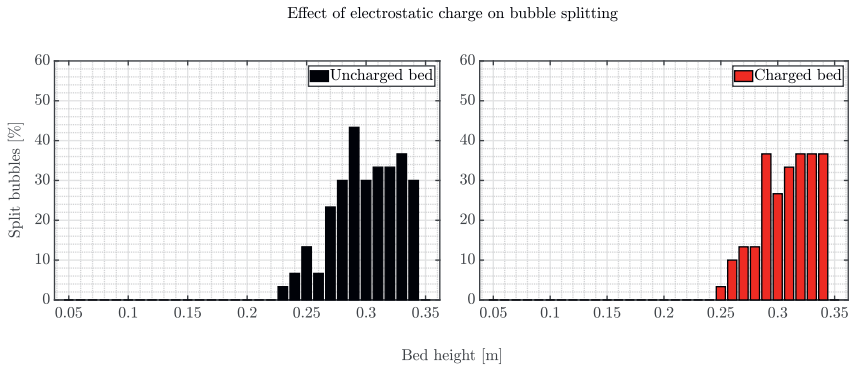


Figure 4.17: Percentage of bubbles that are split over the vertical position. The percentage is taken from the 30 bubble recordings for each case.

to be much of a difference between the charged and uncharged beds. The larger error bars for the aspect-ratio and bubble diameter can be explained by the increased probability of splitting towards the top, although both characteristics vary dramatically when a bubble splits or coalesces. The increase in bubble splitting towards the top of the bed is consistent with previous observations by Jalalinejad et al. (2016) and Tan et al. (2018), who reported particle raining from the bubble roof and eventual bubble break-up in charged fluidized beds. However, once a stable bubble was established, the present results indicate that the overall splitting frequency was not strongly affected by electrostatic charging.

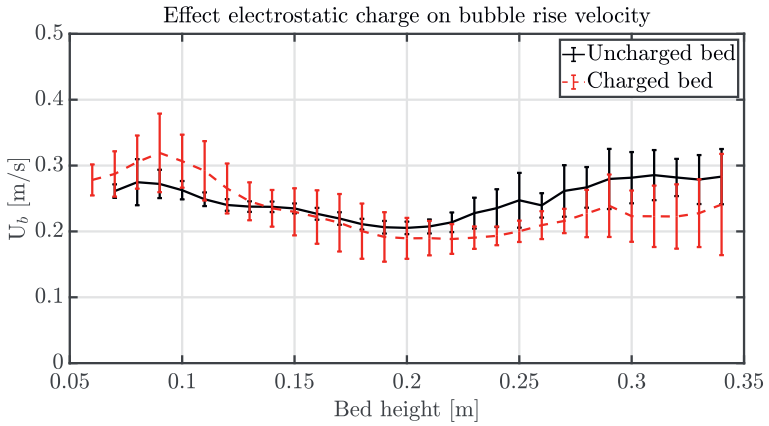


Figure 4.18: Average bubble rise velocity in an uncharged bed (black) and charged bed (red).

Finally, Figure 4.18 depicts the difference in injected bubble rise velocity. In the uncharged bed the average bubble rise velocity is 0.248 $\mathrm{m\,s^{-1}}$ and in the charged bed it is 0.234 $\mathrm{m\,s^{-1}}$ which are quite similar. The rise velocity of bubbles for Geldart B type particles is mostly influenced by the interstitial velocity, which is influenced by the background velocity. Since U_{mf} increases for charged beds, a higher background velocity was used of 0.240 $\mathrm{m\,s^{-1}}$ as opposed to the 0.191 $\mathrm{m\,s^{-1}}$ used in the uncharged bed. However, on average the rise velocity is still slightly lower for the charged bed. This might be due to an increase in bed voidage, which should reduce the interstitial velocity.The relatively small influence of charging on bubble rise velocity contrasts with the numerical predictions of Jalalinejad et al. (2012), who predicted that electrostatically elongated bubbles would rise faster than bubbles in uncharged beds. The absence of a significant velocity increase in the present work is consistent with the limited changes observed in bubble shape and suggests that electrostatic effects primarily alter gas leakage and bubble stability rather than bubble acceleration.

To check if these results are consistent with different injection volumes, the injection volume was reduced to 33.3 mL. The results, shown in Figure 4.19, demonstrate that again the bubble area is smaller in the charged bed. The visible bubble volume accounted for 55.1% and 24.5% of the injected volume for uncharged and charged beds respectively. Hence, when the bed is charged, the bubble hold-up drops by 30.6% on average, which is nearly twice as much as when a 50.0 mL injection volume was utilized.

In comparison to the prior results, the bubble volumes are often smaller. The maximum average bubble volumes are just 70.4% and 33.6% of the injected volume for the uncharged and charged bed respectively. So, significantly less gas from the injected volume travels through the bed in the bubble phase relative to when a bigger injection volume is used. The

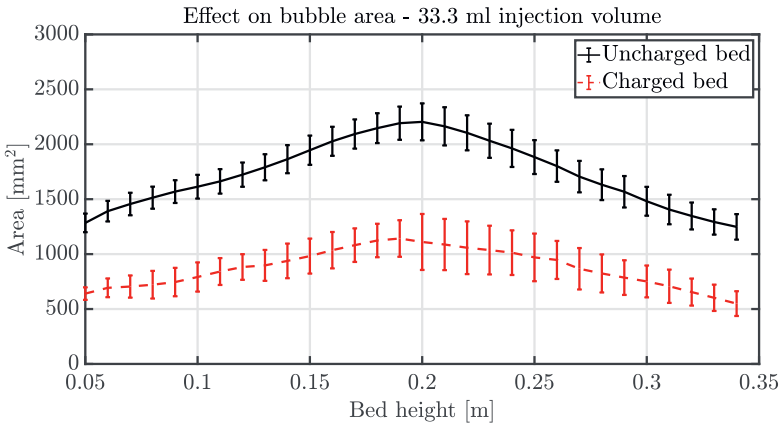


Figure 4.19: Average bubble area in uncharged bed (black) and charged bed (red) as a function of the height in the bed with a smaller injection volume of 33.3 mL.

bubbles tend to get substantially wider and split more often in a charged bed according to these results. The higher tendency of the bubbles to split is not only caused by the actual splitting of bubbles themselves, but rather the formation of multiple bubbles during the injection. An example of this is shown in Figure 4.20. It obviously shows the bubble that formed at the injection hole (1), as well as another bubble that formed higher in the bed (2). This is due to the earlier described heterogeneity of the charged bed. Some locations in the bed have a higher voidage, which allows for bubble formation when the additional volume of gas is introduced into the bed. So that multiple bubbles were presented at the same time, which was recorded as a 'split bubble'. Since the bubbles are much smaller they tend to get wider when they are breaking higher in the bed, as it is more difficult for the smaller gas volume to displace the solid particles.

The occurrence of multiple bubbles at different heights following a single gas injection appears to be associated with the heterogeneous voidage structure observed in charged beds. Although bubble splitting and instability have previously been reported in charged fluidized beds (Jalalinejad et al. 2016; Tan et al. 2018), similar observations of bubble formation at multiple locations within the bed were not found in the literature consulted for this work. Further research is required to determine the generality and underlying mechanisms of this phenomenon.

To make sure that these results are not exaggerated by the absolute difference in background gas velocity between the charged and uncharged cases because of the differences in the minimum fluidization velocities, , another set of experiments was performed using the same absolute background velocity. We opted to use the minimum fluidization velocity as observed for uncharged beds ($U_g = 0.191$ m s^{-1}), which sets the relative

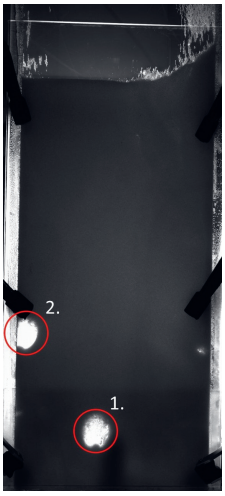


Figure 4.20: Bubbles forming in multiple locations during bubble injection with a 33.3 mL injection volume in a charged bed.

velocity for the charged bed to approximately 0.8 U_{mf}. The injection velocity was set to 4.24 $\mathrm{m\,s^{-1}}$, which results in an injection volume of 66.7 mL. To induce bubble formation in the charged bed, this relatively larger injection volume was required. A total of 10 bubbles were recorded and analyzed for both an uncharged and a charged bed, and the results for the average bubble area is shown in Figure 4.21.

Clearly, the area of the bubbles in the charged bed is much lower, which is expected since the background velocity does not equal the minimum fluidization velocity. On average, the bubble volume in the uncharged bed is 53.7 mL and only 14.8 mL in the charged bed. This decrease of 58.3% is much more significant than those observed in previous results. These results support that the minimum fluidization velocity is indeed higher in case of a charged bed. Apart from the significantly smaller bubbles, the shape of the bubble does not seem to be strongly influenced by the charge on the particles.

Freely bubbling bed

In this section we investigate how electrostatic charges affect the behavior of fluidization under freely bubbling conditions. Both uncharged and charged beds are used, and the bed was operated at 1.3, 1.6, and 2.0 times the respective value of U_{mf}. Each experiment was recorded for three minutes at a frame rate of 30 frames per second, yielding 5400 frames in total. The experimental data was compared with a correlation by Shen et al. (2004), which predicts the bubble diameter as a function of the height for pseudo

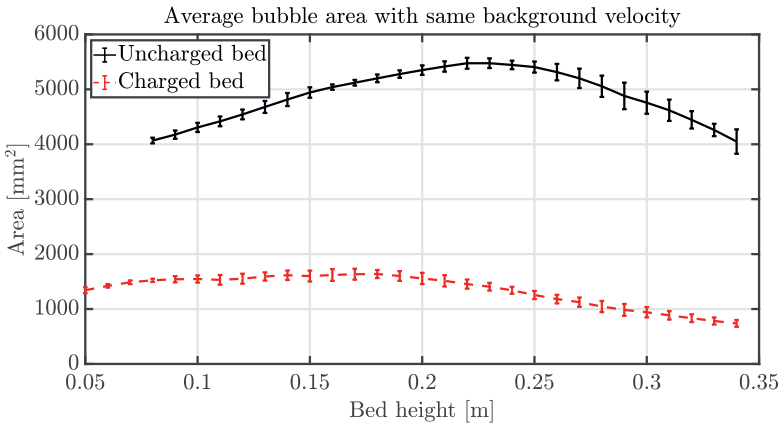


Figure 4.21: Average bubble area in uncharged bed (black) and charged bed (red) as function of the height in the bed when the same background velocity was used (0.191 m s^{-1}) with an injection volume of 66.7 mL.

2D fluidized beds with Geldart B type solids. The correlation is shown in equation 4.5.

$$d_b = 0.89 \left((U_0 - U_{mf}) \left(h + 3.0 \frac{A_0}{t} \right) \right)^{\frac{2}{3}} g^{\frac{1}{3}} \tag{4.5}$$

Here, h is the height, A_0 is the catchment area, t is the depth of the bed and g is the gravitational acceleration constant. Their work was based on a fluidized bed with a larger width and depth (0.68×0.07 m) compared to the bed used in this work (0.202×0.011 m). So that their correlation probably overpredicts the experimental results as bubbles can grow to larger diameters in their set-up (Laverman et al. 2008; Shen et al. 2004). Figure 4.22 shows the equivalent bubble diameter as a function of the vertical position in case of an uncharged bed. The equivalent bubble diameter is defined as in equation 4.6.

$$d_b = \sqrt{\frac{4S_b}{\pi}} \tag{4.6}$$

Here S_b is equal to the bubble area in the pseudo 2D bed. The results show that the correlation by Shen et al. (2004) slightly underestimates the bubble diameter obtained from the experimental results, but the general trend of bubbles growing as they rise clearly corresponds reasonably well.

Figure 4.23 illustrates the findings of the same experiments with a charged bed. Take into account that even though U_{mf} is increased for the charged bed, the correlation values are indeed slightly higher. The observations indicate that the correlation, once again, underestimates the experimental results. The difference appears to be larger in the case of the charged bed than in the case of the uncharged bed. The single bubble injection tests

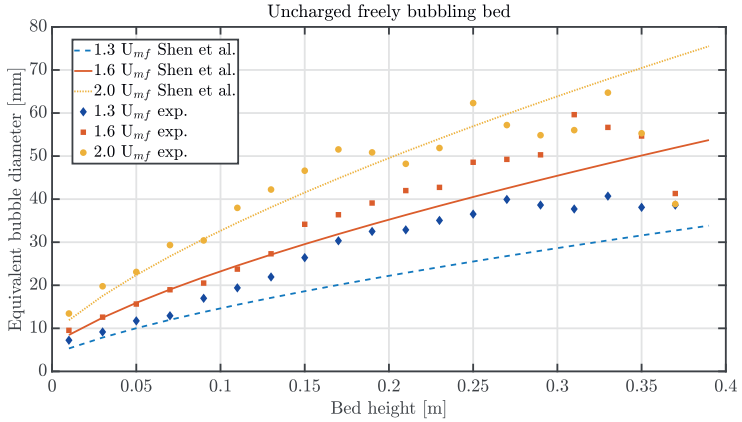


Figure 4.22: Equivalent bubble diameter over the height for 1.3, 1.6 and 2.0 times U_{mf} in an uncharged bed compared to the correlation by Shen et al. (2004)

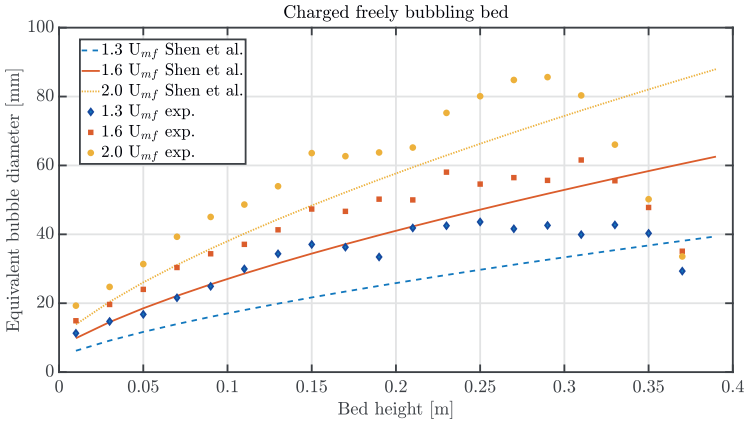


Figure 4.23: Equivalent bubble diameter over the height for 1.3, 1.6 and 2.0 times U_{mf} in a charged bed compared to the correlation by Shen et al. (2004)

revealed that the size of bubbles in a charged bed decreased, which was attributed to an increase in bed voidage. As a result, comparable findings were predicted for the freely bubbling bed results. It seems however, that in a freely bubbling bed the bubbles are slightly larger compared to the uncharged bed. To rule out that this is not caused by the increase in gas flow rate due to the increase in U_{mf}. Experiments were performed with the same background velocity, the result is shown in Figure 4.24 and clearly shows that the obtained bubble diameters are very similar for the charged and uncharged beds.

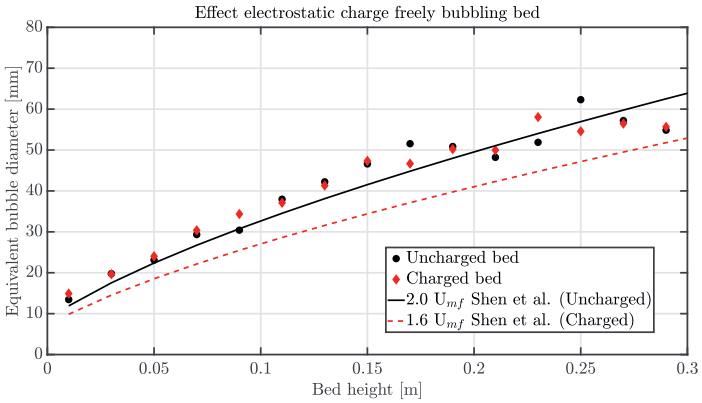


Figure 4.24: The equivalent bubble diameter in a freely bubbling bed in case of an uncharged bed (black) and charged bed (red) when the gas flow rate is very similar (50.9 and 51.2 l/min respectively).

These results indicate that the bubble size is not affected by the charged particles in case of a freely bubbling bed. This could be explained by the change to the bubbling regime, when compared to the single bubble injection experiments; the most distinctive feature of the bed under minimum fluidization condition, i.e. the increased and inhomogeneous bed voidage, becomes less noticeable as the overall bed voidage significantly increases for bubbling fluidization in the first place. The small increase in voidage due to the repulsive force between the particles has a negligible impact. However, due to the increase in U_{mf}, the bubble diameter should also be smaller in case of the charged bed, as is indicated by the dashed lines in Figure 4.24. Also this characteristic seems to become less prevalent, due to the change to a bubbling fluidization regime, suggesting that the electrostatic charge mostly influences the hydrodynamics at lower gas velocities around U_{mf} and below, while it still does affect the absolute value for U_{mf}, of course.

Since U_{mf} is increased for charged beds, the excess gas flow at a given U_g/U_{mf} ratio is actually higher for charged beds. The excess gas can, to a large extent, pass through the interstitial zone (further expanding the bed in the case of charged particles), keeping bubbles of similar size, but affecting the amount of gas flowing through the emulsion phase.

Finally, the average bubble flow rate in the freely bubbling beds were analyzed and compared to thee case of an uncharged and a charged bed for the different superficial gas velocities. Figure 4.25 shows the results for the uncharged bed and Figure 4.26 shows the results for the charged bed. Clearly, for both cases at lower gas velocities the gas is not homogeneously distributed over the bed. This was likely due to inconsistencies in the porous plate that acts as gas distributor; this could result in bigger bubbles locally, and explain the underestimation by Shen et al. (2004) correlation. However, in case of the highest flow rates (Fig. 4.25C and Fig. 4.26C) the gas is

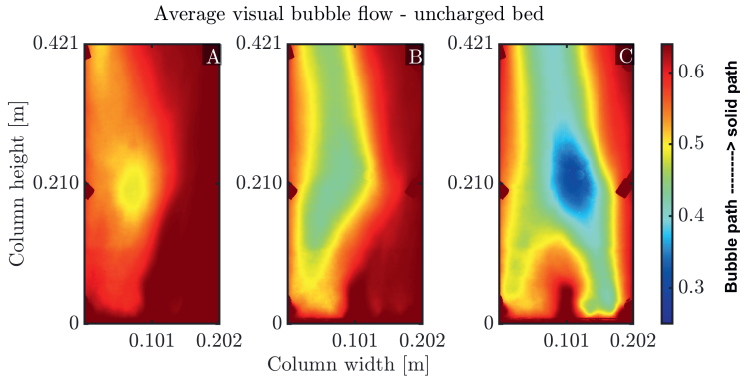


Figure 4.25: Average visual bubble flow for an uncharged bed at 1.3 U_{mf} (A), 1.6 U_{mf} (B) and 2.0 U_{mf} (C).

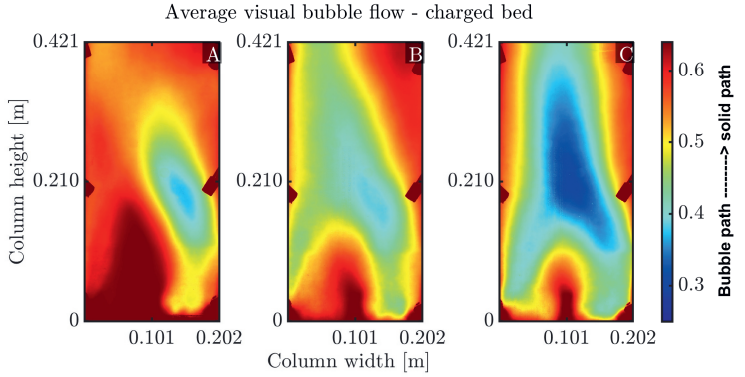


Figure 4.26: Average visual bubble flow rate for a charged bed at 1.3 U_{mf} (A), 1.6 U_{mf} (B) and 2.0 U_{mf} (C).

distributed homogeneously, yet the experimental bubble diameter in the charged beds is still larger than the one predicted by equation 4.6. The results also show the similarity between Figure 4.25C and 4.26B, which correspond with the results shown in Figure 4.24. This also suggest that the hydrodynamics for these situations are very similar.

General observations

In this final section of the results some general observations will be discussed that were observed during the experiments. One of these observations was the deposition of particles on the column walls. Charged particles would stick to the inside of the column wall, forming layers of deposited particles. This is caused by the attracting force between the particles and walls. These

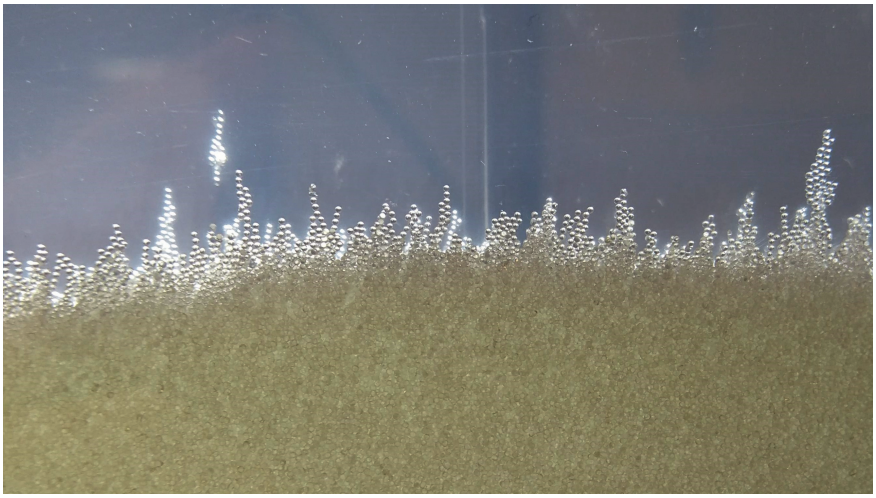


Figure 4.27: Particles attracting each other on the walls at the bed surface.

deposited particle layers were very difficult to remove and the only successful method was to supply humidified gas to the column. The particles on the walls seemed to mostly repel each other, since they had charges of the same sign. However, since glass is an insulating material,its surface may be covered with zones of positive and negative charge. This was also observed during the experiments, as stacks of particles formed at the surface of the bed. These stacks did not form by chance, but were caused by an attracting force between the particles. This shows that the glass particles had zones of opposite charge which allowed them to attract each other. An example of this is shown in Figure 4.27.

Next, particle bridges were detected forming within the bed. These were only observed when the bed was charged and frequently happened when switching from a high gas velocity to U_{mf}. Figure 4.28 shows an extreme example of such a particle bridge. The image shows a snapshot of a 30 frames per seconds recording made when a particle bridge was present. It demonstrates that this bridge was stable for an extended period of time. This shows not just the development of particle bridges, but also the impact of increasing bed voidage on bubble movement. No bubbles can be seen flowing through the section of the bed below and above the gap created by the bridge in the images. The bed above the bubbles is noticeably lighter, indicating a higher level of bed voidage. In certain parts of the bed, all the gas passes through the emulsion phase.

After the gas flow was shut off, the particle bridge collapsed, in Figures 4.29A gas is still supplied at 1 U_{mf}, in 4.29B the gas is shut off and the bed starts to collapse, in 4.29C the bridge has already collapsed and is falling down, and in 4.29D the bed has fully collapsed to itself. It only took 0.3 seconds for the bed to collapse after the gas was shut off. The formation

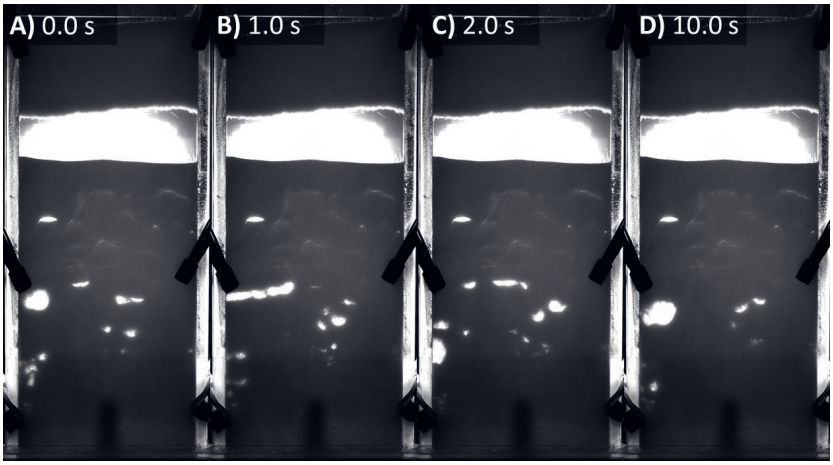


Figure 4.28: Formation of a bridge (at top of the bed) during switching from high gas flow to minimum fluidization gas flow.

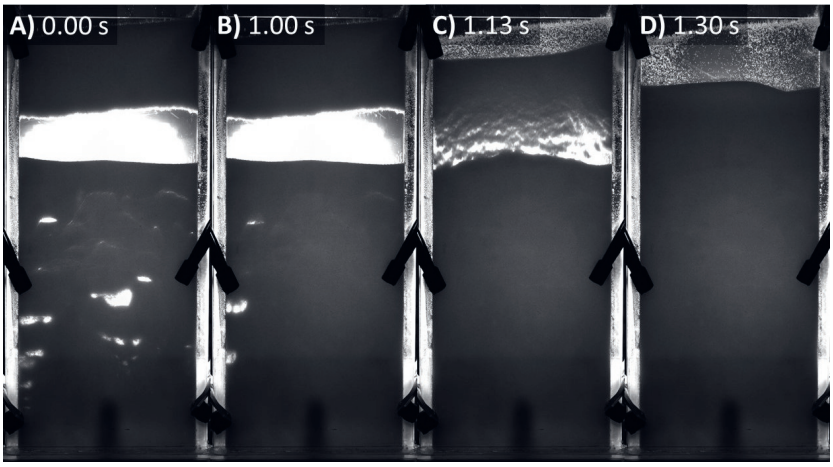


Figure 4.29: Collapse of the bridge after gas flow is turned off after 1 second (B).

of these bridges contributed to the heterogeneity observed in the charged beds, since no bubbles traveled through these parts of the bed.

4.4 Conclusions

Experiments have been conducted to investigate the effect of electrostatic charge on the hydrodynamics in gas-solid fluidized beds. The designed experimental set-up proved to be able to generate electrostatic charge

on the glass particles. It was revealed that, on average, particles gained approximately 1 $\mathrm{nC\,g^{-1}}$ of electrostatic charge. The results also showed that the generation of electrostatic charge is suppressed when the fluidizing gas is humidified, as no significant generation of charge was observed. An important finding was that particles that got stuck on the column walls carried a significantly higher charge. These particles had gained on average 5.0 $\mathrm{nC\,g^{-1}}$, with individual measurements going as high as 15 $\mathrm{nC\,g^{-1}}$.

Experiments revealed an increase in minimum fluidization velocity in case of charged particles. This increase is caused by the increased bed voidage, due to the repulsive electrostatic forces between the particles. The increased bed voidage results in a higher gas velocity needed to reach the pressure drop over the bed, at which the particles start to fluidize, therefore resulting in a higher minimum fluidization velocity. The increased bed voidage also resulted in a slightly higher bed height, albeit with only a small difference. An increase in minimum fluidization velocity was also found by other experimental studies, which validate these results (Manafi et al. 2019).

The minimum bubbling velocity was determined visually, using recordings of the fluidized bed. The analysis shows expected behavior for the uncharged bed, with bubble formation when U_{mf} is exceeded, as is expected for Geldart B type particles. However, in case of the charged bed, bubbles were formed at U_{mf} and required a lower velocity to completely stop bubble formation. The formed bubbles at U_{mf} were only present in some parts of the bed, indicating that the bed voidage was not homogeneous, which has been confirmed by a separate measurement.

Single bubble injection experiments were conducted and showed a decrease in the average bubble area in case of a charged bed. A decrease of 16% visible bubble flow was observed when a bubble injection volume of 50.0 mL was used. The decreased bubble area can be linked to the increase in bed voidage, as more gas of the bubble injectied is able to leak to the emulsion phase. No significant differences in bubble shape were observed, apart from the bubbles being 11% wider on average, in case of a charged bed. One important difference was the stability of the injected bubbles. In case of a charged bed it was much more difficult to produce a stable bubble. However, once a stable bubble was formed they did not seem more likely to collapse in the charged bed. In future studies, the effect of the inhomogeneous voidage profile on the bubble formation, rise and growth should be investigated in more detail, in order to better describe empirical (phenomenological) models for fluidized beds; existing correlations do not fully account for this effect.

The influence of electrostatic charging on bubble behaviour was found to depend on the fluidization regime. While pronounced effects were observed during the single-bubble injection experiments, the average bubble diameters in freely bubbling beds were comparable for charged and uncharged particles at similar gas velocities relative to U_{mf}. This suggests that the increase in bed voidage caused by electrostatic repulsion has a smaller influence on the average bubble size under freely bubbling conditions, where the overall

bed voidage is already substantially increased by the higher gas velocity. Nevertheless, differences in the spatial distribution of bubble activity indicate that electrostatic charging may still affect the local hydrodynamics of the bed.

CHAPTER 5

Heat transfer coefficient in the presence of fouling

Abstract

Electrostatic charging, arising from particle interactions in gas-solid fluidized beds, poses significant operational challenges in industrial processes involving insulating materials such as high-density polyethylene (HDPE). This chapter investigates the influence of electrostatic charge accumulation on fouling and the resulting deterioration of heat-transfer performance in a laboratory-scale fluidized bed with an immersed heating cartridge. The effects of operating temperature, particle size distribution, and superficial gas velocity on electrostatic charging, fouling behaviour, and heat transfer were systematically investigated. Electrostatic charge densities of bulk and fouling particles were measured using a Faraday cup, while the heat-transfer coefficient of an immersed heating element was determined from temperature measurements under controlled operating conditions. The results showed that particles deposited on the heating element consistently carried substantially higher negative charge densities than the bulk particles, while no conclusive dependence of charge accumulation on operating temperature was observed. The unsieved HDPE particles exhibited the highest charge densities and the greatest fouling deposition, whereas gas velocity had only a limited influence on particle charging but significantly affected fouling formation. Comparison with the theoretical correlation of Molerus et al. (1995) showed that progressive fouling reduced the measured heat-transfer coefficient to less than half of the value predicted for a clean fluidized

bed. These findings establish a direct relationship between electrostatic charge accumulation, fouling development, and heat-transfer deterioration, providing valuable insight for improving the thermal efficiency and operational reliability of industrial polymer fluidized-bed drying systems.

5.1 Introduction

Fluidized beds are widely employed in industrial processes such as catalytic cracking, combustion, drying, coating, and polymerization because they provide excellent gas–solid mixing, nearly uniform temperature distributions, and high heat and mass transfer rates. In many of these applications, heat is supplied to or removed from the bed through immersed heating or cooling surfaces, allowing efficient temperature control even in highly exothermic or endothermic processes. Heat transfer in bubbling fluidized beds is governed by gas convection, particle convection, and particle conduction, with continuous particle renewal at the heat-transfer surface representing the dominant heat-transfer mechanism under most operating conditions (Li et al. 2019; Molerus et al. 1995; Molerus et al. 1997). Consequently, fluidized beds exhibit heat-transfer coefficients that are considerably higher than those of many other gas–solid contactors, making them particularly attractive for industrial processes requiring efficient thermal management.

The excellent heat-transfer performance of fluidized beds relies on the continuous replacement of particles at the heat-transfer surface. Any mechanism that suppresses particle renewal or introduces an additional thermal resistance between the particles and the heat-exchanging surface can significantly reduce the heat-transfer coefficient. One of the principal causes of this deterioration is fouling, whereby particles gradually accumulate on immersed heat-transfer surfaces and reactor walls, forming an insulating deposit layer that impedes heat transfer and may eventually impair reactor performance (Hendrickson 2006; Oliveira 1997).

The numerical and experimental investigations presented in the preceding chapters have established that electrostatic charging plays an important role in modifying the behaviour of gas–solid fluidized beds. Chapter 3 demonstrated, through numerical simulations, that electrostatic interactions alter particle motion and fluidization hydrodynamics, whereas Chapter 4 experimentally confirmed their influence on particle charging and bubble dynamics. In addition to these hydrodynamic effects, electrostatic charging promotes particle deposition on solid surfaces and is expected to contribute to fouling formation on immersed heat-transfer surfaces. As the fouling layer grows, an additional thermal resistance is introduced between the heat-transfer surface and the fluidized particles, leading to a progressive deterioration of heat-transfer performance (Hendrickson 2006; Mehrani et al. 2005; Mehrani et al. 2017; Salama et al. 2013). This progression naturally

motivates the present chapter, in which the engineering consequences of electrostatic charging are investigated through their influence on fouling development and heat-transfer performance.

One important industrial process affected by these phenomena is the drying of high-density polyethylene (HDPE) particles following slurry-phase polymerization. Fluidized-bed dryers are widely used because of their excellent heat and mass transfer characteristics. However, repeated particle–particle and particle–wall collisions during fluidization generate electrostatic charges that are retained by the electrically insulating polymer particles. The resulting particle deposition on heated surfaces promotes fouling, reduces heat-transfer efficiency, increases maintenance requirements, and may ultimately lead to unplanned shutdowns and significant economic losses (Hendrickson 2006; Salama et al. 2013). Increasing the temperature of the immersed heat-exchange surfaces is not feasible because the operating temperature is limited by the melting point of the HDPE particles. Moreover, even at temperatures below the melting point, the particles become increasingly sticky, promoting agglomeration and adhesion to the surfaces of the immersed heat exchangers.

Previous studies have shown that electrostatic charging and fouling are strongly influenced by operating conditions such as particle size distribution, superficial gas velocity, temperature, humidity, and material properties (Mehrani et al. 2017; Nifuku et al. 2003; Sowinski et al. 2012; Sowinski et al. 2010). These parameters influence not only charge generation and dissipation but also particle transport, wall deposition, and fluidization hydrodynamics. Fine particles generally exhibit higher charge-to-mass ratios and a greater tendency to adhere to reactor walls and heated surfaces than coarse particles (Sowinski et al. 2012; Sowinski et al. 2010). Consequently, the combined influence of these operating conditions on fouling development and heat-transfer performance remains highly coupled and difficult to predict.

Although electrostatic charging, particle deposition, fluidized-bed hydrodynamics, and heat-transfer mechanisms have each been investigated extensively, these phenomena have generally been studied independently. Relatively few experimental studies have quantitatively established the complete relationship between electrostatic charge accumulation, fouling development, and the resulting deterioration of heat-transfer performance under controlled operating conditions. A systematic understanding of this relationship is essential for developing effective mitigation strategies aimed at improving the thermal efficiency and operational reliability of industrial polymer fluidized-bed processes.

The objective of this chapter is therefore to experimentally investigate the influence of operating temperature, superficial gas velocity, and particle size distribution on electrostatic charging, fouling behaviour, and heat transfer in a laboratory-scale gas–solid fluidized bed containing high-density polyethylene (HDPE) particles. With an immersed heating cartridge, electrostatic charge accumulation is quantified using Faraday cup measurements, while fouling formation on an immersed heated surface

is monitored simultaneously. The measured heat-transfer coefficients are subsequently compared with the correlation proposed by Molerus et al. (1995) to quantify the deterioration in thermal performance resulting from electrostatic fouling.

5.2 Experimental Setup

The experimental setup consists of a stainless steel gas-solid fluidized bed reactor, constructed from two welded sections. The bottom section houses a porous distributor plate at the base, designed with holes of 40 µm in diameter to ensure uniform gas distribution. Nitrogen was used as the fluidizing gas. The nitrogen fluidizing gas was not separately preheated before entering the column at room temperature; heating of the bed was provided by the immersed heating element. The active fluidization zone has a diameter of 50 mm and a height of 265 mm, providing a controlled environment for the fluidization experiments.

A centrally positioned electric heating element was integrated into the bed to simulate industrial drying conditions. The heating element has a diameter of 6.5 mm and a length of 75 mm. The stainless-steel heating element was electrically connected to the grounded reactor body, ensuring that it remained at ground potential throughout the experiments. Two thermocouples were installed to monitor the thermal conditions during the experiments. One thermocouple measured the surface temperature of the heating element, while the second measured the bed temperature at a fixed distance from the heater. These measurements were used to determine the temperature difference required for calculating the heat-transfer coefficient.

To maintain stable thermal boundary conditions and minimize heat losses to the surroundings, the entire fluidized bed reactor was enclosed within an insulated electrical oven. This configuration ensured nearly uniform thermal conditions throughout all experiments. A schematic of the fluidized bed reactor is shown in Figure 5.1, while an overview of the laboratory-scale experimental setup is presented in Figure 5.2.

High-density polyethylene (HDPE) polymer particles were used as the bed material because polymer particles readily accumulate electrostatic charge and are representative of industrial fluidized-bed drying processes. The particles had a mean volume-averaged diameter $D[4,3]= 227.8\,\mu m$ and were classified as Geldart B type particles. Under non-electrified conditions, Geldart Group B particles typically exhibit stable bubbling fluidization, making them a suitable baseline for investigating the influence of electrostatic charging. To investigate the influence of particle size distribution, fouling behaviour, and heat transfer, HDPE particles (obtained from SABIC) were sieved into distinct size groups. In addition, experiments were performed using the original unsieved material for comparison. The measured particle size distribution (PSD) of both unsieved and sieved HDPE particles, along

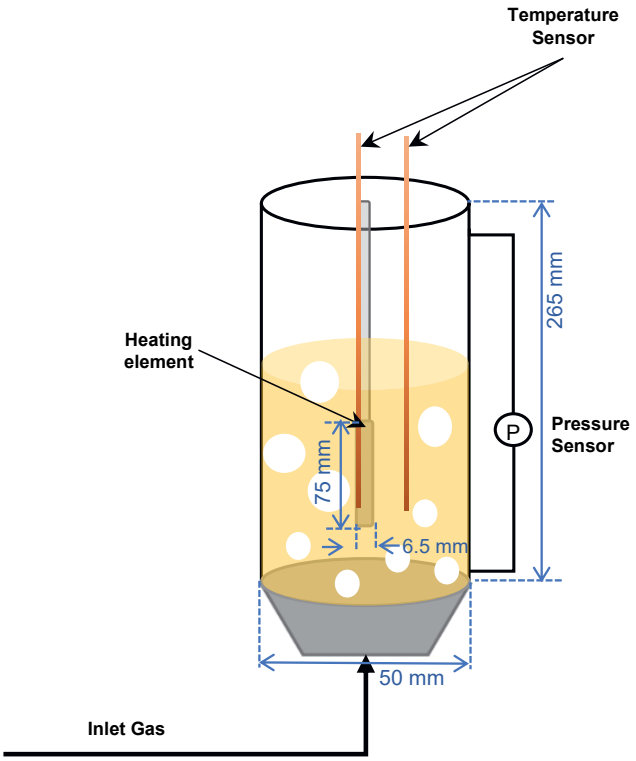


Figure 5.1: Schematic of the experimental setup: gas-solid fluidized bed including a central electric heating element.

with their corresponding experimentally measured minimum fluidization velocities (U_{mf}) following the procedure described in Section 4.3, are presented in Table 5.1.

Table 5.1: HDPE particle size distribution and experimentally measured minimum fluidization velocities of the investigated particle groups.

Particle groups	D[4,3] µm	Span	U_{mf} [m s^{-1}]
Group 1	186.4	1.07	1.16
Group 2	220.8	1.05	1.37
Group 3	284.9	0.99	2.44
Group 4 (unsieved)	227.8	1.11	1.43

Particle size distribution (PSD) measurements were conducted using a FRITSCH Micro Tech Plus Analysette 22 particle size analyzer. Detailed

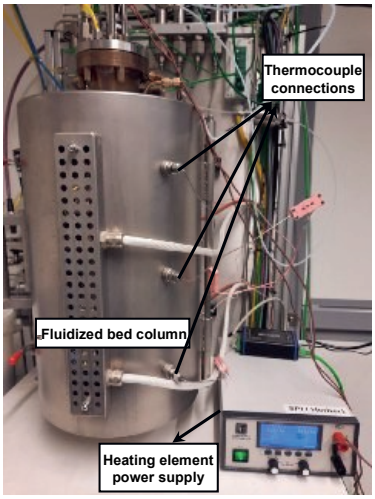


Figure 5.2: Photograph of the laboratory-scale fluidized-bed apparatus showing the fluidization column, thermocouple connections, and heating-element power controller

PSD results for all samples are provided in Appendix 5.4. Analysis of the unsieved sample revealed that approximately 20% of the particles were smaller than 100 µm. These fine particles have a tendency to adhere to larger particles, potentially influencing fluidization behavior and making the sieving process more challenging. Similarly, the PSD analysis of the sieved fractions showed that more than 10% of the particles in each group were below 100µm, which may affect interparticle interactions and charging behavior within the fluidized bed. This is visually demonstrated in Figure 5.3, included in Appendix 5.4, where small particles can be observed adhering to the surface of larger particles. This adhesion tendency may contribute to changes in effective particle size, charge transfer behavior, and fluidization characteristics.

5.3 Results and Discussion

Charge Generation and Fouling Behavior in a Fluidized Bed at Different Operating Temperatures

To evaluate the influence of operating temperature on electrostatic charge accumulation and fouling behaviour, unsieved HDPE particles were fluidized

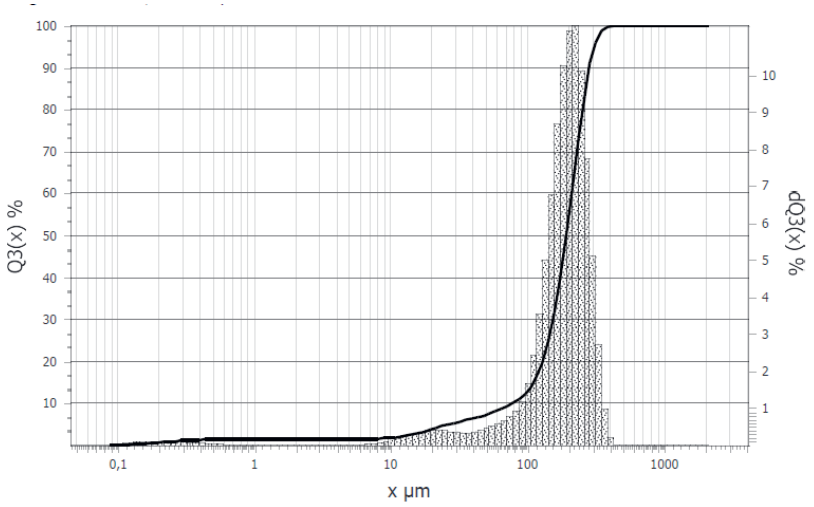
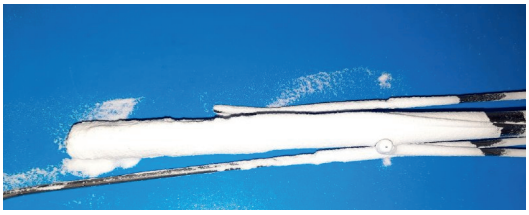


Figure 5.3: Particle size distribution of sieved particles with 180 to 220 µm

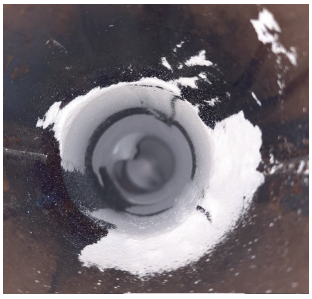
at four different cartridge heater temperature settings. Nitrogen was supplied as the fluidizing gas at a superficial velocity of 2.86 $\mathrm{m\,s^{-1}}$, corresponding to 2.0 times the minimum fluidization velocity (U_{mf}). After one hour of operation, the accumulated charge of both the bulk particles and the fouling particles was measured using a Faraday cup following the procedure described in Chapter 4. Here, fouling particles refer to particles that remained deposited on the surface of the heating element at the end of the experiment. After fluidization, the heating element was carefully removed from the bed to avoid mixing the deposited particles with the bulk material. The heating element was then gently tapped directly above the Faraday cup, allowing the deposited particles to fall directly into the cup for charge measurement. Subsequently, the bulk particles remaining in the bed were collected and measured separately. Since the deposits were removed without rubbing or scraping the surface, disturbance of the electrostatic charge during sample collection was minimized. A limitation of the present charge-measurement procedure is that particles deposited on the reactor wall could not always be collected reproducibly. While some wall deposits could be detached by tapping, others remained attached to the surface. These particles may have a different charge density from the particles remaining in the bulk bed, and their incomplete recovery may therefore contribute to the variability in the measured charge densities. An in-line, non-intrusive charge-measurement technique would be beneficial in future studies to monitor electrostatic charge without requiring particle sampling.

Representative photographs of the experimental setup after operation are shown in Figure 5.4a and 5.4b. The images illustrate the polymer deposits observed on the cartridge heating element and on the inner reactor

wall following the fluidization experiments. A detailed discussion of these observations is presented together with the quantitative fouling and heat-transfer results in the following sections.



(a) Polymer deposits on the cartridge heating element.



(b) Polymer deposition on the inner reactor wall.

Figure 5.4: Representative photographs of polymer deposition observed after the fluidization experiments: (a) polymer deposits on the cartridge heating element and (b) polymer deposition on the inner wall of the fluidized-bed reactor.

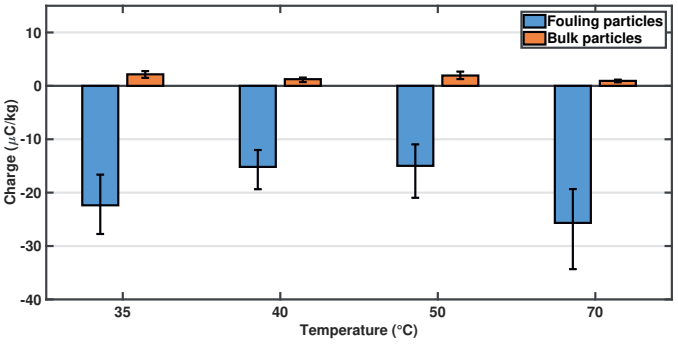


Figure 5.5: Charge of bulk and fouling particles fluidized at different temperatures

For each operating temperature, the experiment was repeated under identical operating conditions. The reported charge densities represent the average of the repeated measurements, while the error bars indicate the minimum and maximum measured values.

Analysis of the measured charge densities revealed a clear distinction between the electrostatic behaviour of bulk and fouling particles. Under all operating temperatures, bulk particles carried relatively low positive charge densities, whereas particles deposited on the heating element consistently exhibited substantially larger negative charge densities. This indicates that

particles adhering to the heated surface preferentially accumulated negative charge during fluidization.

Although some variation in charge density was observed with operating temperature, no consistent trend could be identified within the investigated temperature range. Considering the experimental variability reflected by the error bars, the results do not demonstrate a conclusive dependence of electrostatic charge accumulation on operating temperature.

The observation that fouling particles carried considerably larger negative charge densities than bulk particles is consistent with previous studies on polyethylene fluidized beds, in which particles deposited on reactor walls were also found to exhibit more negative charge than particles remaining in the bulk of the bed (Salama et al. 2013). This behaviour suggests that electrostatic charging promotes the preferential deposition of negatively charged particles on the heating surface, thereby contributing to fouling formation.

HDPE particles generally acquire a negative electrostatic charge when they repeatedly collide with metallic heat-exchange surfaces due to triboelectric charging, whereby electrons are transferred from the metal to the polymer. The direction of charge transfer depends on the work function of the metal, the electron affinity of the polymer, surface chemistry (oxide layers, contamination), humidity, and operating temperature. HDPE is near the negative end of the triboelectric series, indicating a relatively strong tendency to gain electrons from many common engineering metals, as observed in our experiments. Elevated temperatures can enhance this effect by increasing the contact area and contact time during collisions, while the inherently low electrical conductivity of HDPE prevents the accumulated charge from dissipating. As a result, negatively charged particles adhering to the heat-exchange surfaces create electrostatic attraction for incoming particles, which, together with thermal softening, promotes particle deposition, agglomeration, and the progressive growth of fouling layers. However, this effect could not be clearly discerned from our experiments.

Effect of Particle Size and Gas Velocity on Charge Generation and Fouling Formation

To further investigate the influence of particle size distribution and gas velocity on charge generation, four different particle size groups (listed in Table 5.1) were fluidized at two superficial gas velocities corresponding to 2.5 and 5 times the minimum fluidization velocity. The measured charge densities are presented in Figure 5.6. The unsieved particles sample, which contained the broadest particle size distribution and the highest proportion of fine particles, exhibited the largest charge densities among the investigated particle groups. In contrast, the charge densities of the sieved particle groups

were considerably lower. Increasing the gas velocity from 2.5 to 5 U_{mf} had only a limited influence on the measured particle charge densities.

The corresponding fouling masses deposited on the heating element are presented in Figure 5.7. In contrast to the charge measurements, gas velocity had a more pronounced influence on fouling formation. For all particle groups, higher gas velocity generally resulted in increased fouling deposition on the heating element.

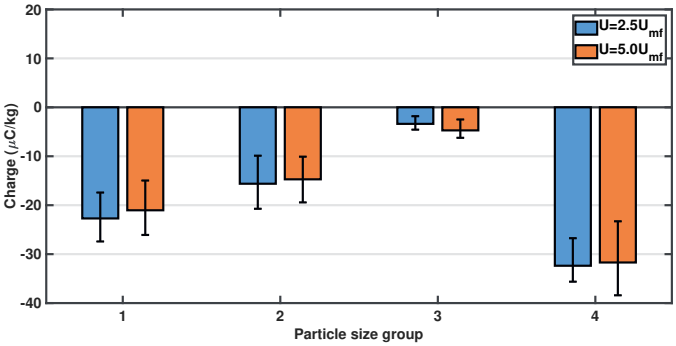


Figure 5.6: Average charge density of the investigated particle groups at different superficial gas velocities.

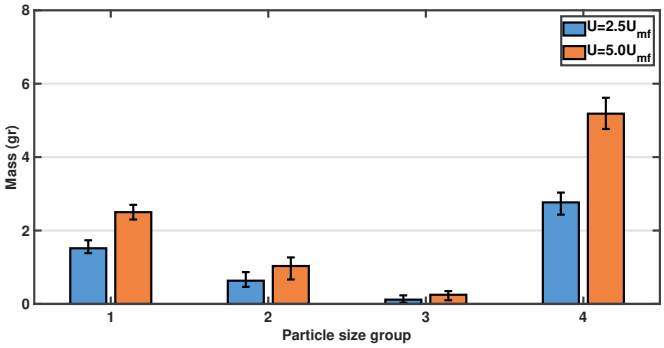


Figure 5.7: Average fouling mass deposited on the heating element for the investigated particle groups at different superficial gas velocities.

The results presented in Figure 5.7 indicate that the unsieved particle sample consistently exhibited the greatest fouling deposition, whereas particle Groups 2 and 3, consisting of relatively larger particles, produced considerably lower fouling masses. The higher fouling observed for the unsieved material coincided with its higher measured charge density (Figure 5.6), suggesting that the broader particle size distribution and the presence of fine particles may promote electrostatic charge accumulation and,

consequently, fouling formation. However, based on the present experiments, the individual contribution of the fine particles cannot be isolated and therefore no direct causal relationship can be established.

Smaller HDPE particles generally accumulate a higher negative electrostatic charge than larger particles because triboelectric charging is fundamentally a surface phenomenon. Owing to their higher surface-area-to-volume ratio, smaller particles acquire more charge per unit mass and undergo more frequent collisions with neighbouring particles and heat-exchange surfaces. Furthermore, the low electrical conductivity of HDPE inhibits rapid charge dissipation, resulting in a charge-to-mass ratio that increases approximately inversely with particle diameter. Consequently, electrostatic forces become increasingly significant relative to gravitational forces as particle size decreases, making fine particles more susceptible to adhesion, agglomeration, and entrainment. This trend is clearly reflected in the experimental results, where the smaller particles exhibit a substantially higher charge density (Figures 5.6) together with a correspondingly greater fouling mass (Figure 5.7). The particle size distribution (PSD) also has a pronounced influence on both charge generation and particle deposition. In beds with a broad PSD, collisions between particles of different sizes promote size-dependent triboelectric charge segregation, whereby fine particles preferentially acquire a negative charge while coarse particles become relatively positive, despite being composed of the same material. The resulting electrostatic attraction enhances the deposition of fine particles on heated surfaces, where they initiate and stabilize fouling layers that subsequently capture larger particles. Moreover, a broad PSD provides a continuous supply of fines that fill voids within the deposit, producing denser, more cohesive fouling layers. Consequently, minimizing the generation and accumulation of fines by carefully controlling PSD and particle attrition is an effective strategy for mitigating electrostatic fouling in fluidized-bed heat exchangers. This mechanism is strongly supported by the experimental results, which show substantially greater fouling mass and higher charge density for the particle sample with the broadest particle-size distribution (Figures 5.6 and 5.7). The superficial gas velocity has two competing effects on the mass of the fouling layer formed on heated surfaces. Increasing the gas velocity enhances particle circulation, collision frequency, and shear, thereby intensifying triboelectric charging and increasing the electrostatic attraction between particles and the heated surface, which promotes the growth of thicker fouling layers. Conversely, higher particle velocities also lead to more frequent high-energy impacts that mechanically erode and detach adhered particles, thereby giving rise to a self-cleaning effect. Consequently, the net fouling behaviour is determined by the balance between enhanced electrostatic deposition and mechanical removal, with the dominant mechanism depending on the operating conditions. Within the range investigated in the present study, up to a superficial gas velocity of approximately 5 Umf, the enhanced triboelectric charging and deposition appear to outweigh the self-cleaning effect, as evidenced by the increasing fouling mass and charge density observed in Figures 5.6 and

5.7.

Impact of Fouling on Heat Transfer in the Fluidized Bed

Since high-density polyethylene (HDPE) particles are commonly dried in fluidized bed dryers, fouling formation on immersed heat-transfer surfaces can significantly affect thermal performance. To investigate this effect, temperatures were continuously monitored at two locations: (i) on the heating element surface and (ii) at a fixed position within the fluidized bed. The electrical power supplied to the heating element was maintained constant throughout the experiments, allowing the heat-transfer coefficient to be determined from the measured temperature difference between the heating surface and the fluidized bed.

Figure 5.8 shows the temporal evolution of the heating-element surface temperature and the bulk-bed temperature during a representative experiment.

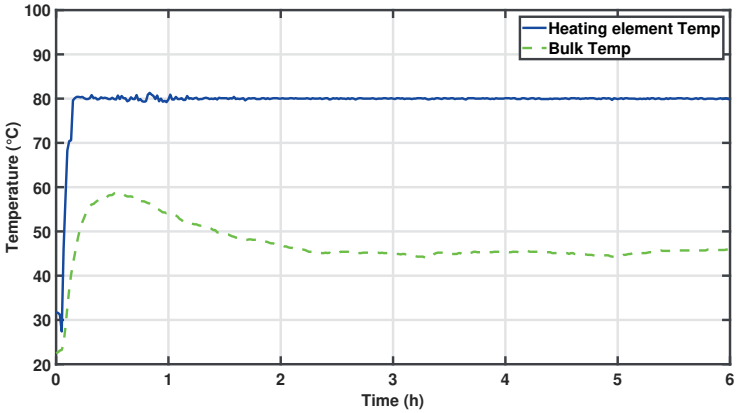


Figure 5.8: Temperature evolution of the heating element surface and the fluidized bed during the experiment with an 80°C heater setpoint. Nitrogen was supplied at a superficial gas velocity of 2.86 $\mathrm{m\,s^{-1}}$ using unsieved HDPE particles.

The measured temperatures indicate that the system gradually approaches thermal equilibrium and reaches a nearly steady thermal state after approximately two hours of operation. A closer examination of the initial heating period reveals a gradual reduction in the bulk-bed temperature during approximately the first 45 minutes, while the heating conditions remained unchanged. This behaviour coincides with the progressive accumulation of polymer deposits on the heating element observed during the experiments. As the fouling layer develops, an additional thermal resistance is introduced between the heating surface and the fluidized particles, reducing the amount

of heat transferred from the heater to the bed and consequently lowering the bulk-bed temperature.

To quantify the influence of fouling on heat transfer, the experimentally measured heat-transfer coefficient was compared with the theoretical correlation proposed by Molerus et al. (1995). The Molerus correlation predicts the particle-to-surface heat-transfer coefficient for bubbling fluidized beds with clean heat-transfer surfaces as a function of the fluidization conditions and the thermophysical properties of the gas–particle system. It is expressed as

$$\frac{h_{pc} l_l}{k_g} = \frac{0.125(1-\varepsilon_{mf})}{1+\dfrac{k_g}{2c_p\mu}} \; \frac{1}{1+\dfrac{25}{\sqrt[3]{\left(\dfrac{U_g-U_{mf}}{U_{mf}}\right)}\sqrt[3]{\dfrac{\rho_p c_p}{k_g g}\,(U_g-U_{mf})}}} \tag{5.1}$$

$$l_l = \left[\frac{\mu}{\sqrt{g(\rho_p-\rho_g)}}\right]^{2/3} \tag{5.2}$$

where

h_{pc}	particle-to-surface heat-transfer coefficient,
k_g	gas thermal conductivity,
l_l	characteristic length,
ε_{mf}	bed voidage at minimum fluidization,
u	superficial gas velocity,
U_{mf}	minimum fluidization velocity,
ρ_p	particle density,
ρ_g	gas density,
c_p	particle specific heat capacity,
μ	gas dynamic viscosity,
g	gravitational acceleration.

Figure 5.9 compares the experimentally measured heat-transfer coefficient with the value predicted by Eq. (5.1).

At the beginning of the experiment, the measured heat-transfer coefficient agrees well with the theoretical prediction, indicating that heat transfer initially follows the behaviour expected for a clean fluidized bed. As the experiment progresses, however, the measured heat-transfer coefficient gradually decreases and eventually falls to less than half of the value predicted by Molerus' correlation. Since the operating conditions remained constant throughout the experiment, this progressive deviation is attributed to the accumulation of polymer deposits on the heating element. The growing fouling layer increases the thermal resistance between the heating surface and the fluidized particles, thereby reducing the effective heat transfer from the heater to the bed.

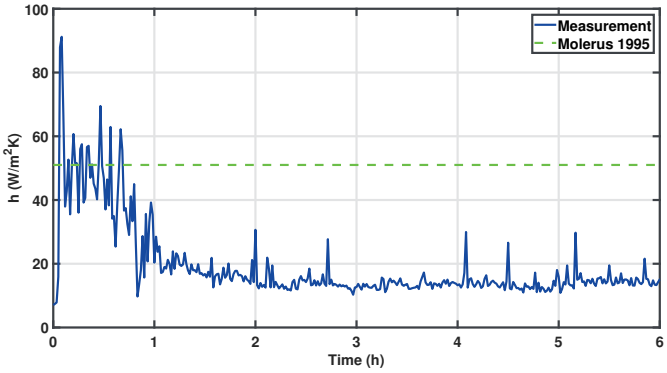


Figure 5.9: Comparison between the experimentally measured heat-transfer coefficient and the theoretical value predicted by the Molerus correlation for a clean fluidized bed.

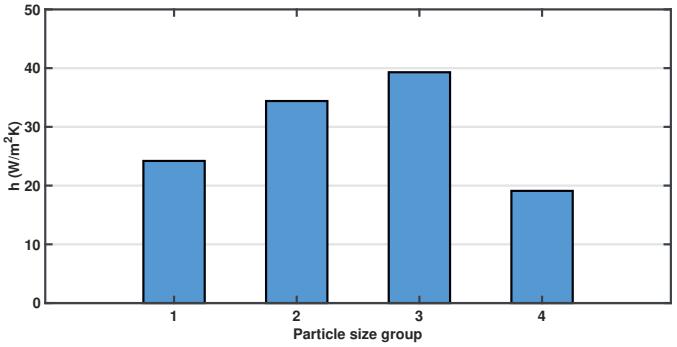


Figure 5.10: Measured heat-transfer coefficients for the investigated HDPE particle groups at different superficial gas velocities.

The measured heat-transfer coefficients for all investigated particle groups are presented in Figure 5.10.

The results demonstrate that particle groups exhibiting greater fouling deposition consistently showed lower heat-transfer coefficients. Comparison of Figures 5.6, 5.7, and 5.10 reveals a clear relationship between electrostatic charge accumulation, fouling formation, and heat-transfer performance. The unsieved HDPE particle sample exhibited the highest charge densities and the greatest fouling deposition, which corresponded to the lowest measured heat-transfer coefficient. In contrast, particle Groups 2 and 3 generated lower charge densities, formed less fouling, and consequently maintained higher heat-transfer coefficients, although lower heat transfer coefficients might have been expected in a clean bed without charge accumulation.

These observations provide experimental evidence that increased electrostatic charging promotes preferential particle deposition on the heating surface, increasing the thermal resistance of the fouling layer and thereby reducing heat-transfer performance.

The observed relationship between electrostatic charge accumulation, fouling formation, and heat-transfer deterioration indicates that electrostatic charging is an important contributor to fouling development in the present system. Since the heating element was electrically connected to the grounded stainless-steel reactor, electrostatic attraction between the charged HDPE particles and the grounded metallic surface may contribute to particle deposition. However, the present experiments do not allow the individual deposition mechanisms to be distinguished. Particle–surface adhesion, together with the elevated temperature of the heating element, may also contribute to fouling formation.

Although the experiments were performed under controlled laboratory conditions using HDPE particles, the observed trends are directly relevant to industrial polymer fluidized-bed dryers, where electrostatic charging and fouling commonly occur during prolonged operation. The results demonstrate that electrostatic charge accumulation is closely associated with fouling development and the resulting deterioration of heat-transfer performance, providing valuable insight for improving the design and operation of industrial fluidized-bed systems.

5.4 Conclusion

This chapter experimentally investigated the influence of electrostatic charging on fouling formation and the resulting deterioration of heat-transfer performance in a gas–solid fluidized bed containing HDPE particles. Particular attention was given to the effects of operating temperature, particle size distribution, and superficial gas velocity on electrostatic charge accumulation, fouling behaviour, and heat transfer.

The experimental results demonstrated a clear distinction between the electrostatic behaviour of bulk particles and particles deposited on the heating element. Fouling particles consistently carried substantially larger negative charge densities than the bulk particles, indicating that electrostatic charging promotes preferential particle deposition on heated surfaces. Although charge densities varied between operating temperatures, no conclusive dependence of electrostatic charge accumulation on temperature was identified within the investigated range.

Particle size distribution was found to have a pronounced influence on both charge generation and fouling behaviour. The unsieved HDPE particles, containing the broadest particle size distribution and the highest proportion of fine particles, exhibited the highest charge densities and the greatest fouling deposition. In contrast, increasing the superficial gas velocity had

only a limited influence on particle charge accumulation but significantly affected the amount of fouling deposited on the heating surface.

The progressive accumulation of polymer deposits introduced an additional thermal resistance between the heating element and the fluidized particles, resulting in a substantial deterioration of heat-transfer performance. Initially, the experimentally measured heat-transfer coefficient agreed well with the theoretical correlation proposed by Molerus et al. (1995). As fouling developed, however, the measured heat-transfer coefficient gradually decreased to less than half of the predicted clean-bed value.

Overall, the results demonstrate that electrostatic charging plays a critical role in fouling formation and the associated degradation of heat transfer in polymer fluidized beds. By establishing a direct relationship between electrostatic charge accumulation, fouling development, and heat-transfer deterioration, this work provides valuable insight for improving the design, operation, and thermal efficiency of industrial fluidized-bed drying systems.

Appendix A: Particle Size Distributions

Particle size distributions (PSD) for different particle fractions were measured using a FRITSCH Micro Tech Plus Analysette 22 particle size analyzer under dry conditions at a pressure of 5 bar.

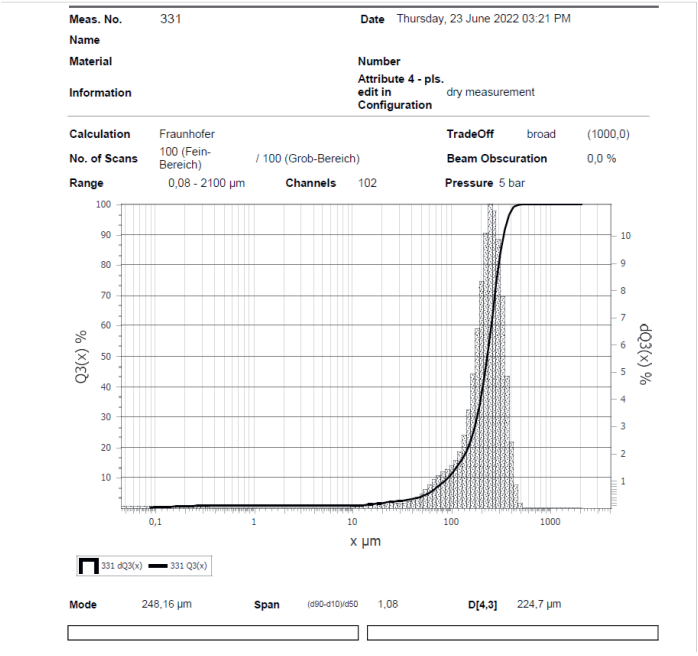


Figure 5.11: The PSD of unsieved particles

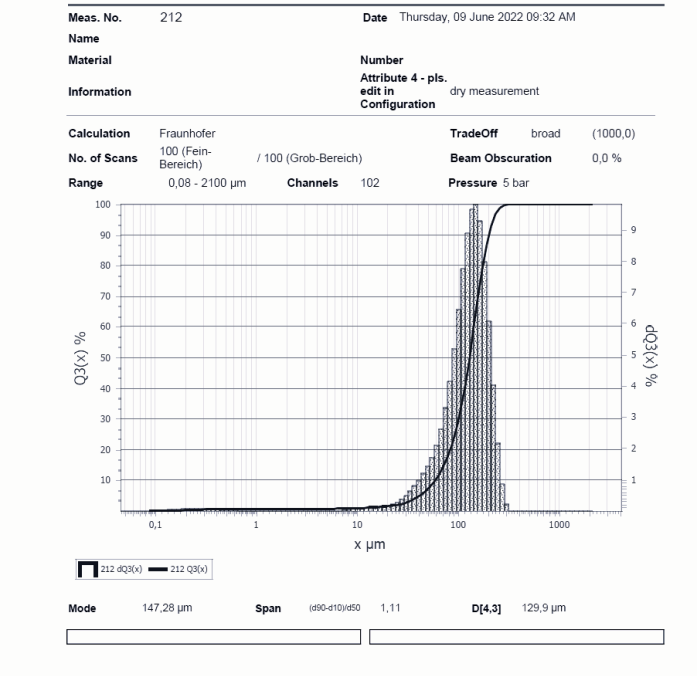


Figure 5.12: The PSD of sieved particles, Below 180µm fraction

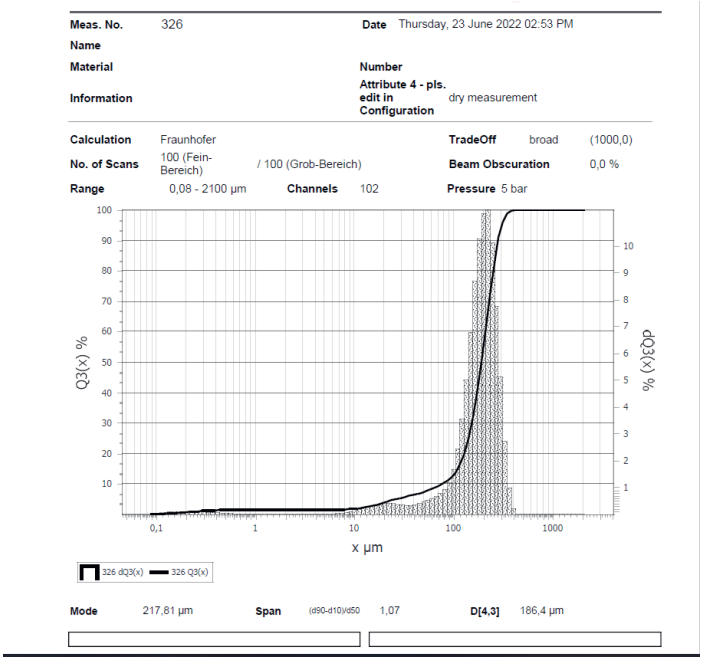


Figure 5.13: The PSD of sieved particles, 180–224 µm fraction

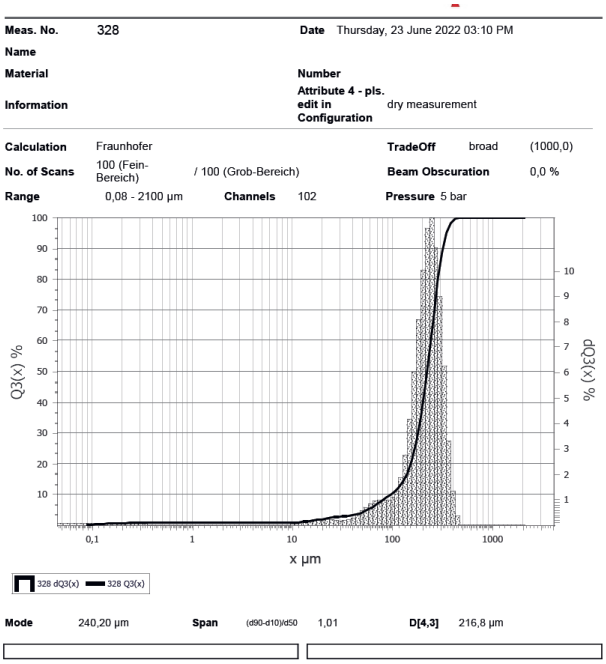


Figure 5.14: The PSD of sieved particles, 224-300µm fraction

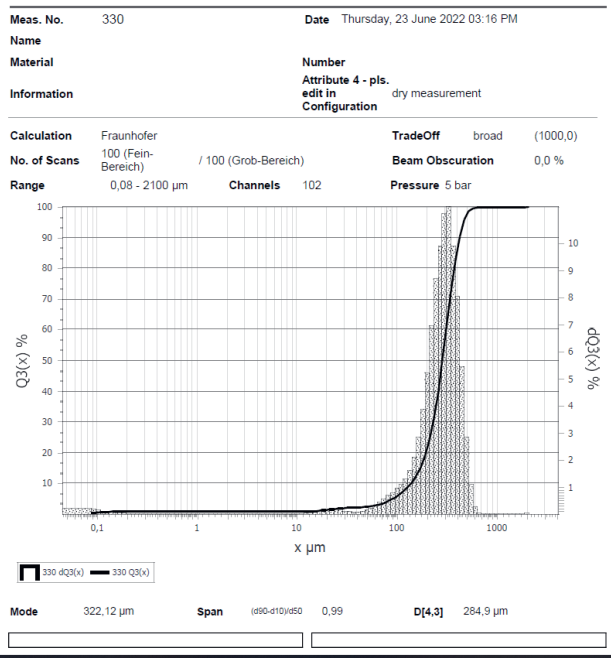


Figure 5.15: The PSD of sieved particles, upper 300µm fraction

CHAPTER 6

Discussion and Conclusions

Abstract

This chapter synthesizes the principal findings of the numerical and experimental investigations presented throughout this thesis and discusses their implications for the understanding of electrostatic phenomena in gas–solid fluidized beds. The combined results demonstrate that electrostatic charging significantly influences fluidized-bed hydrodynamics by increasing the minimum fluidization velocity, modifying bed structure, and altering bubble behaviour. In addition, experimental investigations show that electrostatic charging promotes fouling formation on grounded heat-transfer surfaces immersed in the fluidized bed, resulting in a substantial deterioration of heat-transfer performance. The chapter further evaluates the methodological contributions of the proposed hierarchical electrostatic force model and the accompanying experimental studies, highlighting their significance for the simulation and characterization of charged particulate systems. Finally, the limitations of the present work are discussed, and future research directions are identified, including improved charge-transfer and charge-dissipation models, humidity effects, image-charge formulations for grounded surfaces, and advanced experimental techniques for measuring local charge distributions. These developments will contribute to more predictive electrostatic CFD–DEM simulations, novel strategies to mitigate fouling and its adverse effects on the heat transfer performance, and ultimately more efficient, reliable, and safer industrial fluidized-bed processes.

6.1 Summary and Comparative Analysis

This research systematically examined the impact of electrostatic charges on fluidized bed hydrodynamics through numerical simulations and experimental studies. Numerically, with a discrete particle method (DPM), the importance of accounting for long-range particle-particle electric forces was demonstrated, although these long-range forces are often neglected in screened-force methods. The DPM was extended by a hybrid computational algorithm and was enhanced to accurately account for both short- and long-range electrostatic interactions. This method significantly improved the efficiency and accuracy of simulations by explicitly calculating short-range interactions and approximating long-range interactions using lumped charges. Experimentally, a pseudo-2D fluidized bed setup utilizing Geldart B-type glass particles was investigated to elucidate the effects of electrostatic charges on key fluidization parameters.

Both numerical simulations and experimental observations consistently demonstrated that electrostatic charges notably increased the minimum fluidization velocity (U_{mf}). Specifically, experimental results revealed approximately a 33% increase in U_{mf} compared to uncharged conditions. This phenomenon was attributed to electrostatically induced repulsive forces, which increased bed voidage and allowed the charged system to function as an expanded fixed bed at higher gas velocities prior to the onset of full fluidization. Bubble dynamics were similarly influenced, with both methods observing a reduction in the measured bubble area together with more elongated and diffuse bubble structures in charged beds, attributed to enhanced interstitial gas flow facilitated by increased bed voidage.

In addition, experiments were conducted to investigate the effect of triboelectrically induced particle fouling on the heat transfer performance of immersed heated surfaces as a function of particle size, operating temperature, and superficial gas velocity. The results demonstrate the severe deterioration in heat transfer caused by fouling and reveal the complex interplay between enhanced electrostatic deposition and mechanical removal, which governs the extent of fouling under different operating conditions. However, quantitative discrepancies between numerical and experimental results were observed. These differences can be largely explained by inherent simplifications in the numerical model, such as neglecting particle-wall image charges, assuming uniform charge distributions on particles, and applying idealized boundary conditions. Moreover, the numerical model needs to be further enhanced to allow simulations with a large number of particles, enabling for a one-to-one comparison with experiments.

6.2 Industrial Relevance

The influence of electrostatic charges on fluidization behaviors observed in this study is substantial, profoundly altering bed hydrodynamics. Specifically, the increased bed voidage, reduced bubble formation and size, and delayed onset of fluidization resulting from electrostatic repulsion significantly modify gas-solid interactions. These electrostatic effects pose considerable challenges for industrial operations, potentially leading to particle agglomeration, uneven particle distribution, reduced reactor efficiency, and enhanced risks of electrostatic discharges, which can trigger safety hazards such as fires or explosions.

Given these implications, industries utilizing fluidized bed reactors should implement proactive electrostatic monitoring and control measures. Such measures include optimizing humidity control to manage triboelectrification, adjusting operational parameters to minimize detrimental electrostatic effects, and employing materials (e.g. antistatic agents) or coatings that reduce electrostatic charge generation. Incorporating these strategies based on the findings from this research can effectively mitigate the adverse impacts of electrostatic charges, ensuring safer and more efficient fluidized bed processes. The observed influence of electrostatic charging also has implications for laboratory-scale fluidization studies. Changes in minimum fluidization velocity, bubble dynamics, and heat-transfer behaviour caused by electrostatic interactions may affect the experimental characterization of fluidized beds. Accounting for these effects is therefore important when experimental data are interpreted or used for the development and validation of fluidized-bed models.

6.3 Evaluation of Modeling Approaches and Methodological Contributions

This study introduced a novel hybrid numerical approach, which effectively bridged the gap between computational efficiency and accuracy in simulating electrostatic interactions within fluidized beds. Traditional computational methods typically neglect long-range interactions or employ simplified screened force methods, which result in substantial computational inaccuracies. The hybrid algorithm presented here, by contrast, significantly reduced computational errors from around 50% to less than 7%, thus providing a viable and robust solution for large-scale simulations.

The key contributions of this research include the development and validation of a computationally efficient and highly accurate electrostatic force calculation methodology. Additionally, the comprehensive experimental validation presented herein clarified the role of electrostatic charges in modifying fluidized bed hydrodynamics, particularly elucidating their

influence on critical parameters such as bubble dynamics and minimum fluidization velocity as well as the role of electrostatics in triboelectrically induced particle fouling and its influence on heat-exchanger performance. These methodological advancements present important tools for both scientific research and practical industrial applications.

6.4 Outlook

While this research achieved rigorous and insightful outcomes, several limitations and uncertainties were acknowledged. The numerical model employed simplified assumptions, such as uniform and prescribed particle charges at the particle center, exclusion of image charges, and idealized boundary conditions. Moreover, charge generation, transfer, and dissipation were not included in the model, which limits the prediction of charge evolution under realistic operating conditions. Similarly, experimental approaches encountered practical limitations related to accurate charge distribution measurements and precision in assessing electrostatic influences.

To address these limitations, future research directions are recommended. Detailed investigations into particle-wall interactions, incorporating image charge calculations and realistic charge distributions resulting from a detailed triboelectric charge transfer model, would significantly refine model accuracy. Moreover, incorporating humidity effects and variable particle charges into simulation models would improve their applicability to real-world industrial scenarios. Expanding experimental validation to larger, industrial-scale fluidized bed systems is also crucial for confirming and extending the practical relevance of these findings.

While the present thesis demonstrates the significant influence of electrostatic interactions on fluidized-bed hydrodynamics, fouling formation, and heat-transfer performance, several challenges remain before these phenomena can be predicted reliably under industrial operating conditions. The hybrid electrostatic force model developed in this work substantially improves computational efficiency while maintaining high accuracy for long-range electrostatic interactions. Further computational improvements may be achieved through the implementation of hierarchical tree-based methods, such as the Barnes-Hut algorithm, enabling larger-scale industrial simulations. The present framework provides an efficient foundation for electrostatic CFD–DEM simulations, while future developments should focus on incorporating additional physical mechanisms relevant to industrial applications. Future developments should therefore focus on incorporating dynamic charge transfer, charge dissipation, humidity effects, temperature-dependent particle properties, realistic particle-size distributions, and a fully coupled heat-transfer model into electrostatic CFD–DEM simulations, enabling direct prediction of fouling growth and its influence on heat-transfer coefficients. Such improvements would provide a more complete

representation of industrial fluidized-bed systems and further enhance the predictive capability of numerical models.

On the experimental side, the present work establishes a direct relationship between electrostatic charge accumulation, fouling formation, and heat-transfer deterioration. Future advances in experimental techniques capable of resolving local charge distributions, particle deposition, and electrostatic interactions in real time would provide valuable data for validating next-generation numerical models. The integration of such measurements with fully coupled electrostatic, hydrodynamic, and heat-transfer simulations would provide deeper insight into the mechanisms governing electrostatic phenomena in fluidized beds. Future studies combining experiments and numerical simulations could also evaluate electrostatic mitigation strategies, including continuity additives (antistatic agents), where practically applicable, humidity control, and material or operating-condition modifications, to better understand their role in mitigating triboelectric charging and fouling under industrially relevant conditions. Ultimately, these developments will contribute to improved reactor design, reduced fouling, enhanced heat-transfer performance, and more reliable operation of industrial fluidized-bed processes.

Overall, this thesis demonstrates that electrostatic phenomena cannot be treated as secondary effects in gas–solid fluidized beds. Electrostatic charging directly influences hydrodynamics, particle deposition, and heat-transfer performance. The numerical methods and experimental observations presented in this work provide a foundation for the development of more predictive electrostatic models. Coupling these models with realistic particle charging, heat transfer, and industrial electrostatic mitigation strategies will further improve the reliability and efficiency of industrial fluidized-bed processes.

Bibliography

Aboud, S. et al. (2004). “A Poisson P 3 M Force Field Scheme for Particle-Based Simulations”. In: *Journal of Computational Electronics* vol. 3, pp. 117–133.

Adams, C. K. (1987). *Nature’s Electricity*. Tab Books.

Aghel, B. et al. (2022). “Recent advances in CFD-DEM simulation of fluidized beds”. In: *18th International Conference on Fluid Flow Technologies*.

Alsmari, T. A., Grace, J. R. and Bi, X. T. (2015). “Effects of superficial gas velocity and temperature on entrainment and electrostatics in gas-solid fluidized beds”. In: *Chemical Engineering Science* vol. 123, pp. 49–56.

Bailey, A. G. (1993). “Charging of solids and powders”. In: *Journal of Electrostatics* vol. 30, pp. 167–180.

Barnes, J. and Hut, P. (1986a). “A hierarchical $O(NlogN)$ force-calculation algorithm”. In: *Nature* vol. 324 (4), pp. 446–449.

— (1986b). “A hierarchical $O(N \log N)$ force-calculation algorithm”. In: *Nature* vol. 324, no. 4, pp. 446–449.

Beeman, D. (1976). “Some Multistep Methods for Use in Molecular Dynamics Calculations”. In: *Journal of Computational Physics* vol. 20, no. 2, pp. 130–139.

Chen, A. H., Bi, H. T. and Grace, J. R. (2003). “Measurement of particle charge-to-mass ratios in a gas-solids fluidized bed by a collision probe”. In: *Powder Technology* vol. 135-136, pp. 181–191.

Chen, A. et al. (2006). “Measurement of charge distribution around a rising bubble in a 2-D fluidized bed”. In: *AIChE Journal* vol. 52, no. 1, pp. 174–184.

Cheng, Y. et al. (2012). “Experimental and numerical investigations on the electrostatics generation and transport in the downer reactor of a triple-bed combined circulating fluidized bed”. In: *Industrial & Engineering Chemistry Research* vol. 51, pp. 14258–15267.

Chowdhury, F. et al. (2021). “A review on modeling approaches for the electrostatic charging of particles”. In: *Powder Technology* vol. 389, pp. 104–118.

Cimarelli, C. and Genareau, K. (2022). “A review of volcanic electrification of the atmosphere and volcanic lightning”. In: *Journal of Volcanology and Geothermal Research* vol. 422, p. 107449.

Cocco, R., Reddy Karri, S. B. and Knowlton, T. (2014). “Introduction to fluidization”. In: *Chemical Engineering Progress* vol. 110, no. 11, pp. 21–29.

Cross, J. A. (1987). “Electrostatics: Principles, Problems and Applications”. In: *Physics Bulletin* vol. 38, no. 11, p. 424.

Cundall, P. A. and Strack, O. D. L. (1979). “A discrete numerical model for granular assemblies”. In: *Géotechnique* vol. 29, no. 1, pp. 47–65.

De Jong, J. F. et al. (2012). “Development and validation of a novel Digital Image Analysis method for fluidized bed Particle Image Velocimetry”. In: *Powder Technology* vol. 230, pp. 193–202.

Deen, N. G. et al. (2007). “Review of discrete particle modeling of fluidized beds”. In: *Chemical Engineering Science* vol. 62, no. 1-2, pp. 28–44.

Dehnen, W. (2014). “A fast multipole method for stellar dynamics”. In: *Computational Astrophysics and Cosmology* vol. 1, no. 1, p. 1.

Delebarre, A. (2004). “Revisiting the Wen and Yu equations for minimum fluidization velocity prediction”. In: *Chemical Engineering Research and Design* vol. 82, no. 5, pp. 587–590.

Dong, K. et al. (2015). “Experimental investigation of electrostatic effect on bubble behaviors in gas-solid fluidized bed”. In: *AIChE Journal* vol. 61, no. 4, pp. 1160–1171.

Ergun, S. (1952). “Chemical Engineering Progress”. In: *Chemical Engineering Progress* vol. 48, no. 2, pp. 89–94.

Fotovat, F., Bi, X. T. and Grace, J. R. (2018). “A perspective on electrostatics in gas-solid fluidized beds: Challenges and future research needs”. In: *Powder Technology* vol. 329, pp. 65–75.

Fotovat, F., Bi, X. T. and Grace, J. R. (2017a). “Electrostatics in gas-solid fluidized beds: A review”. In: *Chemical Engineering Science* vol. 173, pp. 303–334.

Fotovat, F. et al. (2017b). “The relationship between fluidized bed electrostatics and entrainment”. In: *Powder Technology* vol. 316, pp. 157–165.

Gan, Z. and Xu, Z. (2014). “Efficient implementation of the Barnes-Hut octree algorithm for Monte Carlo simulations”. In: *Science China Mathematics* vol. 57, no. 7, pp. 1331–1340.

Geldart, D. (1973). “Types of gas fluidization”. In: *Powder Technology* vol. 7, no. 5, pp. 285–292.

Giordano, M. et al. (2025). “Effective dipole model for electrostatic interactions between polarizable spherical particles”. In: *Scientific Reports* vol. 15, no. 1, p. 3121.

Godlieb, W., Deen, N. G. and Kuipers, J. A. M. (2008). “On the relationship between operating pressure and granular temperature: A discrete particle simulation study”. In: *Powder Technology* vol. 182, no. 2, pp. 250–256.

Grosshans, H. and Papalexandris, M. V. (2017). “On the accuracy of the numerical computation of the electrostatic forces between charged particles”. In: *Powder Technology* vol. 322, pp. 185–194.

Hadisarabi, M. et al. (2019). “Computational modeling of the electrostatic charge build-up in fluidized beds”. In: *Journal of Electrostatics* vol. 97, pp. 108–120.

Harper, W. R. (1951). “The Volta Effect as a Cause of Static Electrification”. In: *Proceedings of the Royal Society of London. Series A* vol. 205, no. 1081, pp. 83–103.

Hassani, M. A. et al. (2013). “Numerical investigation of effect of electrostatic forces on the hydrodynamics of gas-solid fluidized beds”. In: *Powder Technology* vol. 246, pp. 16–25.

Hendrickson, G. (2006). *Electrostatics and gas phase fluidized bed polymerization reactor wall sheeting.*

Hoef, M. van der et al. (2008). “Numerical Simulation of Dense Gas-Solid Fluidized Beds: A Multiscale Modeling Strategy”. In: *Annual Review of Fluid Mechanics.*

Hoffmann, R. (2006). “DEM simulations of toner particles with an O(N log N) hierarchical tree code algorithm”. In: *Granular Matter* vol. 8, no. 3, pp. 151–157.

Hogue, M. D. et al. (2008). “Calculating the trajectories of triboelectrically charged particles using DEM”. In: *Journal of Electrostatics* vol. 66, no. 1, pp. 32–38.

Hoomans, B. P. B. et al. (1996). “Discrete particle simulation of bubble and slug formation in a two-dimensional gas-fluidised bed: A hard-sphere approach”. In: *Chemical Engineering Science* vol. 51, no. 1, pp. 99–118.

Hou, J., Grace, J. R. and Bi, X. (2025). “Effect of fluidizing gases, humidity, and grounding on particle charging dynamics in gas-solids fluidized beds”. In: *Chemical Engineering Science*, p. 121279.

Jahnig, C. E., Campbell, D. L. and Martin, H. Z. (1980). “History of fluidized solids development at Exxon”. In: *Exxon Research and Engineering Company*, pp. 3–24.

Jakobsen, H. (2014). “Fluidized Bed Reactors”. In: *Chemical Reactor Modeling*. Springer, Cham.

Jalalinejad, F., Bi, X. T. and Grace, J. R. (2012). “Effect of electrostatic charges on single bubble in gas-solid fluidized beds”. In: *International Journal of Multiphase Flow* vol. 44, pp. 15–28.

— (2016). “Comparison of theory with experiment for single bubbles in charged fluidized particles”. In: *Powder Technology* vol. 290, pp. 27–32.

Jiang, P. et al. (1994). “Hydrodynamic behavior of circulating fluidized bed with polymeric particles”. In: *AIChE Journal* vol. 40, no. 2, pp. 193–206.

Joseph, S. and Klinzing, G. E. (1983). “Vertical gas-solid transition flow with electrostatics”. In: *Powder Technology* vol. 36, no. 1, pp. 79–87.

Kazemi, S. et al. (2021). “CFD-DEM simulation of wall sheeting and particles charge in fluidized beds”. In: *The Canadian Journal of Chemical Engineering* vol. 99, no. 7, pp. 1582–1594.

Kezeng, D. et al. (2015). “Experimental Investigation of Electrostatic Effect on Bubble Behaviors in Gas-Solid Fluidized Bed”. In: *AIChE Journal* vol. 61, no. 4, pp. 1160–1171.

Kohnke, B., Kutzner, C. and Grubmuller, H. (2020). “A GPU-accelerated fast multipole method for GROMACS”. In: *Journal of Chemical Theory and Computation* vol. 16, no. 11, pp. 6938–6949.

Kolehmainen, J. et al. (2016). “A hybrid approach to computing electrostatic forces in fluidized beds of charged particles”. In: *AIChE Journal* vol. 62, pp. 2282–2295.

Korevaar, M. W. et al. (2014). “Integrated DEM-CFD modeling of the contact charging of pneumatically conveyed powders”. In: *Powder Technology* vol. 258, pp. 144–156.

Kunii, D. and Levenspiel, O. (1991). “Bubbles in Dense Beds”. In: *Fluidization Engineering*. Butterworth-Heinemann, pp. 115–135.

— (1994). *Fluidization Engineering*. 2 ed. Butterworth-Heinemann.

Lacks, D. J. and Sankaran, R. M. (2011). “Contact electrification of insulating materials”. In: *Journal of Physics D: Applied Physics* vol. 44, no. 45, p. 453001.

Laverman, J. A. et al. (2008). “Investigation into the hydrodynamics of gas-solid fluidized beds using particle image velocimetry coupled with digital image analysis”. In: *Canadian Journal of Chemical Engineering* vol. 86, no. 3, pp. 523–535.

Li, F. et al. (2019). “Heat Transfer in a Pressurized Fluidized Bed with Continuous Addition of Fine Particles”. In: *Powder Technology* vol. 357, pp. 331–342.

Li, H. et al. (2022). “CFD-DEM investigation into flow characteristics in mixed pulsed fluidized bed under electrostatic effects”. In: *Particuology* vol. 66, pp. 100–112.

Li, J. and Kato, K. (2001). “Effect of electrostatic and capillary forces on the elutriation of fine particles from a fluidized bed”. In: *Advanced Powder Technology* vol. 12, no. 2, pp. 187–205.

Lowell, J. (1979). “Tunnelling between metals and insulators and its role in contact electrification”. In: *Journal of Physics D: Applied Physics* vol. 12, pp. 1541–1554.

Lowell, J. and Rose-Innes, A. (1980). “Contact electrification”. In: *Advances in Physics* vol. 29, pp. 947–1023.

Lu, J. et al. (2020). “Analysis of wall fouling and electrostatic charging in gas-solid fluidized beds”. In: *Advanced Powder Technology* vol. 31, no. 8, pp. 3485–3491.

Manafi, M., Zarghami, R. and Mostoufi, N. (2019). “Fluidization of electrically charged particles”. In: *Journal of Electrostatics* vol. 99, no. February, pp. 9–18.

Matsusaka, S. (2011). “Control of particle tribocharging”. In: *KONA Powder and Particle Journal* vol. 29, pp. 27–38.

Matsusaka, S. and Masuda, H. (2003). “Electrostatics of particles”. In: *Advanced Powder Technology* vol. 14, no. 2, pp. 143–166.

Matsusaka, S. et al. (2010). “Triboelectric charging of powders: A review”. In: *Chemical Engineering Science* vol. 65, no. 22, pp. 5781–5807.

Matsusaka, S., Ghadiri, M. and Masuda, H. (2000). “Electrification of an elastic sphere by repeated impacts on a metal plate”. In: *Journal of Physics D: Applied Physics* vol. 33, no. 18, pp. 2311–2319.

Mehrani, P., Bi, H. T. and Grace, J. R. (2005). “Electrostatic charge generation in gas-solid fluidized beds”. In: *Journal of Electrostatics* vol. 63, no. 2, pp. 165–173.

Mehrani, P., Murtomaa, M. and Lacks, D. J. (2017). “An overview of advances in understanding electrostatic charge buildup in gas-solid fluidized beds”. In: *Journal of Electrostatics* vol. 87, pp. 64–78.

Mihajlovic, M., Roghair, I. and Annaland, M. V. S. (2020). “On the numerical implementation of the Van der Waals force in soft-sphere discrete element models for gas-solid fluidization”. In: *Chemical Engineering Science* vol. 226, p. 115794.

Mihajlović, M. et al. (2025). “Numerical investigation of the influence of temperature on fluidization behavior”. In: *Fluids* vol. 10, no. 3, p. 60.

Molerus, O. and Wirth, K.-E. (1995). “Particle migration at solid surfaces and heat transfer in bubbling fluidized beds”. In: *Heat Transfer in Fluidized Beds*, pp. 5–17.

Molerus, O. and Wirth, K.-E. (1997). *Heat Transfer in Fluidized Beds*. London: Chapman & Hall.

Mori, S. and Wen, C. Y. (1975). “Estimation of bubble diameter in gaseous fluidized beds”. In: *AIChE Journal* vol. 21, no. 1, pp. 109–115.

Nifuku, M. and Katoh, H. (2003). “A study on the static electrification of powders during pneumatic transportation and the ignition of dust cloud”. In: *Powder Technology* vol. 135-136. Electrostatic Phenomena in Particulate Processes, pp. 234–242.

Norouzi, H. R., Zarghami, R. and Mostoufi, N. (2016). “Coupled CFD-DEM modeling of interparticle forces in multiphase flows”. In: *Wiley Handbook of Multiphase Flow*, pp. 372–411.

Oliveira, R. (1997). “Understanding adhesion: A means for preventing fouling”. In: *Experimental Thermal and Fluid Science* vol. 14, no. 4, pp. 316–322.

Pei, C., Wu, C. Y. and Adams, M. (2016). “DEM-CFD analysis of contact electrification and electrostatic interactions during fluidization”. In: *Powder Technology* vol. 304, pp. 208–217.

Pei, C., Wu, C. Y. and Adams, M. (2015). “Numerical analysis of contact electrification of non-spherical particles in a rotating drum”. In: *Powder Technology* vol. 285, pp. 110–122.

Pei, C. et al. (2013). “Numerical analysis of contact electrification using DEM-CFD”. In: *Powder Technology* vol. 248, pp. 34–43.

Ray, M. et al. (2019). “An Euler-Euler model for mono-dispersed gas-particle flows incorporating electrostatic charging”. In: *Chemical Engineering Science* vol. 197, pp. 327–344.

Rokkam, R. G., Fox, R. O. and Muhle, M. E. (2010). “Computational fluid dynamics and electrostatic modeling of polymerization fluidized-bed reactors”. In: *Powder Technology* vol. 203, no. 2, pp. 109–124.

Ruan, X. and Li, S. (2022). “Effect of electrostatic interaction on impact breakage of agglomerates”. In: *Physical Review E* vol. 106, no. 3, p. 034905.

Salama, F. et al. (2013). “Investigation of electrostatic charge distribution within the reactor wall fouling and bulk regions of a gas-solid fluidized bed”. In: *Journal of Electrostatics* vol. 71, no. 1, pp. 21–27.

Shaul, S., Rabinovich, E. and Kalman, H. (2014). “Typical fluidization characteristics for Geldart’s classification groups”. In: *Particulate Science and Technology* vol. 32, no. 2, pp. 197–205.

Shen, L., Johnsson, F. and Leckner, B. (2004). “Digital image analysis of hydrodynamics two-dimensional bubbling fluidized beds”. In: *Chemical Engineering Science* vol. 59, no. 13, pp. 2607–2617.

Sowinski, A., Mayne, A. and Mehrani, P. (2012). “Effect of fluidizing particle size on electrostatic charge generation and reactor wall fouling in gas-solid fluidized beds”. In: *Chemical Engineering Science* vol. 71, pp. 552–563.

Sowinski, A., Miller, L. and Mehrani, P. (2010). “Investigation of electrostatic charge distribution in gas-solid fluidized beds”. In: *Chemical Engineering Science* vol. 65, no. 9, pp. 2771–2781.

Tan, L., Roghair, I. and Sint Annaland, M. van (2014). “Simulation study on the effect of gas permeation on the hydrodynamic characteristics of membrane-assisted micro fluidized beds”. In: *Applied Mathematical Modelling* vol. 38, no. 17, pp. 4291–4307.

Tan, L., Roghair, I. and Sint Annaland, M. van (2017). “Discrete particle simulations of bubble-to-emulsion phase mass transfer in single-bubble fluidized beds”. In: *Particuology* vol. 33, pp. 80–90.

Tan, Z. et al. (2019). “Comparisons of TFM and DEM-CFD simulation analyses on the influence mechanism of electrostatics on single bubble in gas-solid fluidized bed”. In: *Powder Technology* vol. 351, pp. 238–258.

Tan, Z. et al. (2018). “The effect of electrostatics on single bubble in fluidized bed and its mechanism analysis”. In: *Powder Technology* vol. 325, pp. 545–556.

Tardos, G., Yen, B. and Pfeffer, R. (1983). “The effect of static charges on drag reduction in dilute gas-particle suspension flow”. In: *Chemical Engineering Communications* vol. 19, no. 4–6, pp. 205–219.

Tsilingiris, P. T. (2008). “Thermophysical and transport properties of humid air at temperature range between 0 and 100 °C”. In: *Energy Conversion and Management* vol. 49, no. 5, pp. 1098–1110.

Verlet, L. (1967). “Computer ”Experiments” on Classical Fluids. I. Thermodynamical Properties of Lennard-Jones Molecules”. In: *Physical Review* vol. 159, no. 1, pp. 99–103.

Wang, C. et al. (2023). “CFD-DEM study on the interaction between triboelectric charging and fluidization of particles”. In: *Powder Technology* vol. 419, p. 118340.

Wang, J., Hoef, M. A. van der and Kuipers, J. A. M. (2010). “CFD study of the minimum bubbling velocity of Geldart A particles in gas-fluidized beds”. In: *Chemical Engineering Science* vol. 65, no. 12, pp. 3772–3785.

Yang, Y. et al. (2017). “CFD-DEM investigation of particle elutriation with electrostatic effects in gas-solid fluidized beds”. In: *Powder Technology* vol. 308, pp. 422–433.

Yates, J. G. and Lettieri, P. (2016). *Fluidized-Bed Reactors: Processes and Operating Conditions*. Vol. 26.

Zhang, P. et al. (2021). “Experimental investigation of particle adhesion on the wall due to electrostatic charge in gas-solid fluidized beds”. In: *Powder Technology* vol. 387, pp. 373–384.

Zhao, Z. et al. (2024). “Recent advances and perspectives of CFD-DEM simulation in fluidized bed”. In: *Archives of Computational Methods in Engineering* vol. 31, no. 2, pp. 871–918.

Acknowledgements

I would like to thank everyone who supported me during my PhD and helped me along the way.

First, I would like to thank my promotor, Prof. Martin van Sint Annaland, and my co-promotor, Dr. Ivo Roghair, for their guidance, support, and many valuable scientific discussions. I learned a great deal from their knowledge, experience, and feedback, which helped me both in this research and in developing as a researcher.

I also had the pleasure of supervising several students during my PhD. I would like to thank the Master's students Matthijs Koelewijn and Robbert van Eck, and the Bachelor's students Arie Huijgen, Marit Kroese, and Nikolaj P.A.M. d'Hooghe, for their hard work and contributions to different parts of this research. I really enjoyed working with them and also learned a great deal from the experience of supervising them.

I am very grateful to H. G. Fiedler, Control and Automation Engineer, and J. Kors, Mechanical Technician, for their technical support. Their help and experience in designing, building, modifying, and operating the experimental setups were very important for the experimental part of this thesis.

I would also like to sincerely thank Ali Fathiganjehlou for his valuable feedback and support during the writing of this thesis. I am particularly grateful to Milan Mihajlovic for his valuable help and support throughout my research. I would also like to thank my fellow PhD colleagues Alessandro Battistella, Xin Kun, and Francesco Sabatino for their support, helpful discussions, and the enjoyable moments we shared during my PhD journey.

I would also like to thank Judith Wachters-van Gemert, secretary of the Chemical Process Intensification group, for always being kind and helpful and for supporting me with many administrative matters throughout these years.

ChatGPT (OpenAI) was used as a language-support tool during the preparation of this thesis, mainly to help with English grammar, wording, and readability. All scientific content, analysis, interpretation, and conclusions

are my own.

Most importantly, I would like to thank my family. My husband, Mehdi, has been beside me throughout these years. Thank you for your patience, encouragement, and support, and especially for being there during the difficult and demanding periods of my PhD. I could not have completed this journey without you.

To my daughters, Sarah and Saba, thank you for your love, patience, and understanding. There were many times when my PhD took time and attention away from our family, and I know this journey was not only mine. Thank you for understanding the busy days and difficult moments and for bringing so much happiness to my life.

I am also very grateful to my mother, who has always encouraged me and believed in me. Her love and support have given me strength throughout my life and during these years in particular.

My PhD years were also marked by the loss of two of the most important people in my life. I lost my father during the COVID period, and I wish very much that he could have been here to see me finish my PhD. I also lost my brother during these years. He was not only my brother, but also my best friend and someone who always supported me. I miss them both deeply, especially at this moment. I know they would have been happy to see me reach the end of this journey.

Finally, thank you to everyone who, in one way or another, was part of these years and helped me reach this point.

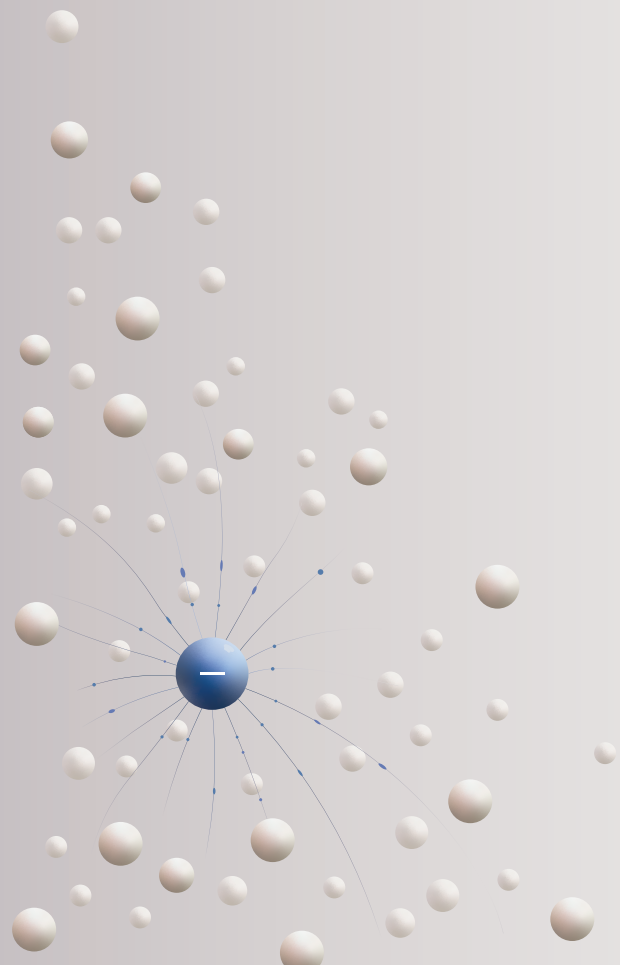
Curriculum Vitae

Marzieh Kordnejad was born in 1982 in Iran. She studied Chemical Engineering at Shiraz University, where she obtained her Bachelor's degree in 2004. Following her graduation, she began her professional career in the chemical industry.

In 2007, she returned to Shiraz University to pursue a Master's degree in Chemical Engineering, with a focus on process simulation and control. Under the supervision of Prof. A. Jahanmiri, she conducted her Master's research on the Real-Time Optimization of a Methanol Reactor and obtained her Master's degree in 2010. She subsequently continued her career in industry, gaining experience in process engineering, simulation, and the design of chemical and process plants.

In March 2017, she started her PhD research in the Chemical Process Intensification group at Eindhoven University of Technology, under the supervision of Prof. Martin van Sint Annaland and Dr. Ivo Roghair. Her doctoral research focused on electrostatic phenomena in gas–solid fluidized beds, combining discrete particle simulations with experimental investigations to study the influence of particle charging on fluidization hydrodynamics, particle deposition, and heat transfer.

Since September 2022, she has been working as a Researcher in Gas Processing at Shell Global Solutions B.V. in the Netherlands. Her work focuses on gas-processing technologies, process modeling, and engineering software development. She currently contributes to the GHG Emission Monitoring Technology group and leads activities related to Tools for Gas Processing, with a particular focus on modeling and software development for acid gas removal.



ISBN: 978-90-386-6792-8